Coherence and decoherence studies in electron matter wave interferometry

Dissertation

der Mathematisch-Naturwissenschaftlichen Fakultät
der Eberhard Karls Universität Tübingen
zur Erlangung des Grades eines
Doktors der Naturwissenschaften
(Dr. rer. nat.)

vorgelegt von
Andreas Pooch
aus Tübingen

Tübingen
2018

Gedruckt mit Genehmigung der Mathematisch-Naturwissenschaftlichen Fakultät der Eberhard Karls Universität Tübingen.

Tag der mündlichen Qualifikation:	05.11.2018
Dekan:	Prof. Dr. Wolfgang Rosenstiel
1. Berichterstatter:	Dr. Alexander Stibor
2. Berichterstatter:	Prof. Dr. Claus Zimmermann

Zusammenfassung

Die Frage nach dem Übergang eines quantenmechanischen Systems hin zur klassischen Mechanik ist seit geraumer Zeit Gegenstand intensiver Forschung und gehört zu den Grundlagen der modernen Physik. Sie lässt sich mit der Theorie der Dekohärenz beschreiben und äußert sich vor allem im Verschwinden makroskopischer Superpositionszustände. Nicht nur in der Grundlagenforschung, sondern auch in der Entwicklung neuer technischer Anwendungen wie z.B. des Quantencomputers ist das Verständnis über Dekohärenzmechanismen von großer Bedeutung. Zahlreiche Experimente aus unterschiedlichen Bereichen der Physik tragen dazu bei. Sie alle vereint jedoch, dass ein Quantenobjekt mit einer meist makroskopischen Umgebung wechselwirkt. Für hybride Quantensysteme ist es außerdem wünschenswert, die Wechselwirkung gezielt kontrollieren und die Kohärenz des Systems möglichst lange aufrecht erhalten zu können. Die Analyse verschiedener Dekohärenzmechanismen ist dafür unerlässlich.
In dieser Arbeit wird anhand eines Biprisma-Interferometers die Dekohärenz von elektronischen Materiewellen an einer Goldoberfläche theoretisch diskutiert und experimentell untersucht. Dieser Aufbau erlaubt durch einfache Zweistrahlinterferenz die Stärke der Wechselwirkung graduell zu variieren. Dabei treten als Parameter sowohl die räumliche Aufspaltung der beiden Teilwellen, als auch ihre Höhe über der Goldplatte auf. Als Messobservable dient jeweils der Kontrastwert des entstehenden Interferenzmusters. In der Analyse der Ergebnisse wird gezeigt, dass zwei bestehende Theorien für die Beschreibung der Wechselwirkung ungeeignet sind. Ein Ansatz der makroskopischen Quantenelektrodynamik, welcher im Wesentlichen auf die dielektrische Permittivität fußt, stellt sich dagegen als vielversprechend heraus.
Im Zuge des anvisierten Vorhabens werden überdies Verbesserungen und Erweiterungen des Experiments vorgestellt. Generell ist bei Materiewellen-Interferometern die Wahl der Teilchenquelle entscheidend für Zuverlässigkeit, Genauigkeit und Erreichen der Daten. In der vorliegenden Arbeit wird daher eine Ein-Atom-Spitze mit optimalen Strahleigenschaften erfolgreich eingesetzt. Um jedoch noch höhere Ströme bei niedrigen Elektronengeschwindigkeiten zu erzielen, wird ein neu konzipiertes Design mit zwei Blenden in das Interferometer integriert. Die Signalrate ist dabei unabhängig von der Elektronenenergie einstellbar. Dies ist vor allem im Hinblick auf sensitive Messungen von Vorteil, da die Belastung der Spitze und störende Einflüsse reduziert werden. Die Beibehaltung der Kohärenzeigenschaften der Elektronen während der Signalerhöhung wird mittels Simulation und Experiment verifiziert. Die Verringerung der Elektronenenergie auf sehr niedrige Werte ist prinzipiell machbar und wird hier gezeigt. Darüber hinaus ist unter Mitwirkung dieser Methode die Bestimmung der Energiebreite einer Ein-Atom-Spitze gelungen.
Die für viele Anwendungen vorteilhaften langsamen Elektronen sind jedoch besonders anfällig für externe Störungen wie mechanische Schwingungen, Temperaturdrifts und elektromagnetische Felder. Der Kontrast des zeitlich aufintegrierten Interferenzmusters

wird reduziert. Im Gegensatz zur Dekohärenz ist dieses kollektive Dephasing der Elektronen jedoch reversibel, wenn sowohl räumliche als auch zeitliche Informationen über die Teilchendetektion vorliegen. Mit Hilfe eines neu installierten Delayline-Detektors wird eine Korrelationsanalyse in allen aufgenommenen Daten angewendet. Dabei lässt sich nicht nur das unverwaschene Muster mit all seinen Merkmalen berechnen, sondern auch Störfrequenzen ermitteln. Aus diesem Grund eignen sich Materiewellen-Interferometer aufgrund ihrer hohen Phasensensitivität hervorragend als Sensorbauteil. Für die Anwendung als Sensor für elektromagnetische und mechanische Schwingungsfrequenzen wird in dieser Arbeit ein kompaktes und leicht handhabbares Interferometer vorgestellt. Hierbei sind die Distanzen der einzelnen Bauteile bezüglich der notwendigen Vergrößerung der Interferenzstreifen so klein wie möglich gehalten. Mit einer herkömmlichen selbstgeätzten Wolframspitze werden Interferenzen erfolgreich demonstriert und mit der Korrelationsanalyse optimiert. Es werden mit unserem Bauteil typische Netzfrequenzen als Störung identifiziert und damit zur Verbesserung der Laborbedingungen für die Dekohärenzanalyse beigetragen. Die Sensitivität dieses Prototyps lässt sich mit veränderten Strahltrajektorien und Aufspaltungen noch erhöhen, ebenso durch Kombination mit der Methode zur Signalerhöhung.
Neben dem erfolgreichen Test der Funktionsfähigkeit von kohärenter Intensitätssteigerung und Dephasierungsanalyse in der Biprisma-Interferometrie ist für die Dekohärenzstudie die Erweiterung zu Fragen der Temperaturabhängigkeit und Leitfähigkeit erstrebenswert. Dazu wird ein kommerzielles Kryostatsystem vorgestellt. Sowohl tiefste Temperaturen mit flüssigem Helium als auch einige Hundert Kelvin sind problemlos möglich. Besonders für die Wechselwirkung mit einer supraleitenden Oberfläche als Dekohärenz-Umgebung, bei welcher bisherige Modellerklärungen schwierig sind und keine Theorien existieren, wird die Implementierung des Kryostaten in die bestehende Anlage simuliert und dargestellt. Speziell für Messungen nahe der Sprungtemperatur wird ein tieferes Verständnis über den quantenmechanischen-klassischen Übergang erwartet.
Diese Arbeit ist sowohl für die Grundlagenforschung im Bereich der Dekohärenztheorie relevant als auch im Hinblick auf Anwendungen in der Elektroneninterferometrie. Zukünftige Entwicklungen in der Quanteninformationstechnologie benötigen eine umfassende Kenntnis der Gesetzmäßigkeiten über die Grenzen der quantenmechanischen Superposition. Die Abgrenzung zur Dephasierung ist dabei ebenfalls von Bedeutung und kann mit Mitteln dieser Arbeit bestimmt werden.

List of Publications

This cumulative thesis is based on the publications listed below. They are thematically ordered as discussed in the thesis and appended at the end.

Publications

Publication [1] **A. Pooch**, M. Seidling, N. Kerker, R. Röpke, A. Rembold, W. T. Chang, I. S. Hwang, and A. Stibor,
Coherent properties of a tunable low-energy electron-matter-wave source,
Physical Review A **97**, 013611 (2018),
doi: 10.1103/PhysRevA.97.013611.

Publication [2] **A. Pooch**, M. Seidling, M. Layer, A. Rembold, and A. Stibor,
A compact electron matter wave interferometer for sensor technology,
Applied Physics Letters **110**, 223108 (2017),
doi: 10.1063/1.4984839.

Publications not included in this thesis

Publication [3] G. Schütz, A. Rembold, **A. Pooch**, S. Meier, P. Schneeweiss, A. Rauschenbeutel, A. Günther, W. T. Chang, I. S. Hwang, and A. Stibor,
Biprism electron interferometry with a single atom tip source,
Ultramicroscopy **141**, 9 (2014),
doi: 10.1016/j.ultramic.2014.02.003.

Publication [4] A. Rembold, G. Schütz, W. T. Chang, A. Stefanov, **A. Pooch**, I. S. Hwang, A. Günther, and A. Stibor,
Correction of dephasing oscillations in matter-wave interferometry,
Physical Review A **89**, 033635 (2014),
doi: 10.1103/PhysRevA.89.033635.

Publication [5] G. Schütz, A. Rembold, **A. Pooch**, H. Prochel, and A. Stibor,
Effective beam separation schemes for the measurement of the electric Aharonov–Bohm effect in an ion interferometer,
Ultramicroscopy **158**, 65 (2015),
doi: 10.1016/j.ultramic.2015.06.016.

Publication [6] G. Schütz, A. Rembold, **A. Pooch**, W. T. Chang, and A. Stibor,
Electron matter wave interferences at high vacuum pressures,
Measurement **68**, 201 (2015),
doi: 10.1016/j.measurement.2015.02.022.

Contributions

The contributions to the manuscripts of this thesis are outlined below. Alexander Stibor proposed and supervised the experiments. All authors participated in the revision of the manuscripts.

- **Publication [1]**

  I planned the concept of enhancing the intensity of an electron source while keeping the energy of the particles constant. The experimental setup was assembled by Michael Seidling and myself. Our co-operation partners Wei-Tse Chang and Ing-Shouh Hwang fabricated the electron source used in the experiment. The measurements of many different interferograms were done by Michael Seidling and myself. The experimental data was evaluated by Michael Seidling with some contributions by myself. The manuscript was mainly written by Alexander Stibor and myself.

- **Publication [2]**

  The idea of mounting a compact interferometer originated from Alexander Stibor with some contributions and discussions by myself. The assembly of the interferometer parts and electronic devices were done by Moritz Layer and myself including a self etched tungsten tip. With the delayline detector Michael Seidling and me were able to record all the measurements. The data was mainly evaluated by Michael Seidling, with some contributions by myself including image editing. The manuscript was written by Alexander Stibor and myself, with contributions of Michael Seidling.

Contents

1 Introduction

The historical development of matter waves follows a long tradition of fundamental considerations concerning the nature of light [7, 8]. However, in 1802 the famous double-slit experiment of YOUNG proved the wave nature of light [9] and paved the way for a various number of early interferometers [10–14]. Thereby, the wave theory and its implications received new impetus which was also supported by the theoretical framework of MAXWELL [15]. But in 1905, EINSTEIN was able to interpret the photoelectric effect theoretically by allocating a quantized energy $E = h\nu$ to every "light quanta" [16]. He made use of PLANCK's radiation hypothesis with the PLANCK constant h and the frequency ν in which the electromagnetic field contains such photons as smallest energy units [17]. COMPTON then provided evidence of the particle behaviour of light by scattering x-rays at graphite [18].

Different experimental problems obviously address both, the particle and the wave nature of light. This prompted DE BROGLIE to state a fundamental principle: all particles of matter with mass m and momentum p exhibit wave properties with a characteristic wavelength $\lambda_{dB} = h/p$ [19]. The bold claim of DE BROGLIE had now to be verified taking into consideration that with increasing mass and velocity of the particles the demands to the experimental setting rise. In fact, the first proof of the matter wave hypothesis succeeded in 1927 by DAVISSON and GERMER [20]. A focussed electron beam with energies up to 100 eV was aimed at a single crystal of nickel atoms and hence diffracted. Intensity maxima and minima occurred for the glancing angles known from x-ray diffractometry. In 1940 BOERSCH demonstrated FRESNEL diffraction of electrons at a macroscopic edge of aluminium oxide [21]. Interestingly, only the distances of the intensity maxima and source-edge is relevant for the determination of the electron wavelength.

A further milestone of matter wave interferometry was the realization of electron interferences with an electrostatic biprism fiber by MÖLLENSTEDT and DÜKER in 1955 [22, 23]. Here, electron wave front splitting took place due to an electric field of a positively biased glass fiber. This work enabled a wide range of thrilling experiments [24] including the present thesis. For example the double-slit interferences with electrons of JÖNSSON [25] was awarded in 2002 to the most beautiful experiment in physics of all time [26]. For that time the fabrication of fine slits of only 300 nm width were outstanding.

Of course, attempts were undertaken to examine heavier particles with regard to their wave properties. RAUCH developed a neutron interferometer by using a perfect silicon single crystal [27]. With enhancing sensitivity of the interferometers, a phase shift with neutrons due to the gravitational field of the earth could be measured [28].

Also, atom interferometers became into use to an increasing extent: CARNAL and MLYNEK executed the double-slit experiment with helium atoms [29]. Inspired by them, interferometers for atoms [30] were applied to measure inertial forces [31], im-

portant constants [32, 33], the earth rotation rate [34] and the gravitation constant [35] with high precision. Even in the field of ultracold atom optics the interference of two overlapping Bose-Einstein condensates of sodium atoms succeeded [36].

A further step towards higher masses was done by ARNDT as he achieved interferences of C_{60} molecules by using a diffraction grating of silicon nitride [37]. Soon after, also C_{70} fullerenes were diffracted by a near-field Talbot-Lau interferometer [38]. This technique allows to use comparably incoherent and weak beam sources as it is usually the case for heavy molecules. The current mass record for the interferometry of complex biomolecules exceeds 10.000 amu [39].

All mentioned seminal experiments enabled today's state-of-the-art interferometers which have become a remarkable tool in various fields of fundamental research and technical applications. With tricky and sophisticated techniques laser interferometers are able to detect gravitational waves [40, 41] and marginal small rotation rates [42]. Fundamental questions of the nature of time [43, 44] are examined as well as the relativity principle [45, 46] by means of atom interferometry. Also, the study of inertial forces becomes accessible in more detail [47, 48]. Different kinds of decoherence processes [49] are described via collisions [50, 51], thermal emission of radiation [52], temperature dependency [53] and photon absorption [54] in the context of molecule interferometry [55].

Matter wave interferometers for electrons and ions also improved significantly within the last few decades [24, 3, 56, 57]. The magnetic AHARONOV-BOHM effect was proven successfully [58–61]. Thereby, a large beam path separation of 60 μm was reached. A micro magnetic coil was placed between the partial waves and enabled a measurable phase shift of the interference pattern due to its magnetic vector potential. Likewise, the well-known SAGNAC effect causes a phase shift, too [62] and was applied to electron interferometry [63]. For that, the whole experimental setup including the power supplies was installed on a rotatable platform with an angular speed of up to 0.5 Hz. Even HANBURY BROWN-TWISS anticorrelations were demonstrated for free electrons, a consequence of PAULI's exclusion principle and showing the fermionic character of electrons [64, 65].

Talking about decoherence mechanism of electron waves in the same breath emphasizes the wide range of applications of electron interferometers [66–69]. The technology is influenced by recent developments concerning the beam source [70–72], the precise electron guiding [73, 74], the coherent beam path separation [75, 76, 3, 77, 78] and single-particle detection methods releasing temporal and spatial information [79, 80].

All electron interferometers make high demands on accuracy, stability and reproducibility of the measurements during their operation. With that, they become more and more sensitive to external influences like vibrations, electromagnetic noise and decoherence effects.

In particular, the latter is a fundamental principle of quantum mechanics which leads in general to a suppression of the coherent properties of a quantum mechanical state. Decoherence effects arise when the closed quantum state interacts with an environment. Thereby, both systems become entangled irreversibly [81]. Originally, the decoherence concept emanates from the measurement problem of quantum mechanics and its interpretation where the superposition principle seems to be incompatible with the classical world. Although every particle is described by a wave function which

obeys the linear SCHRÖDINGER equation, superpositions of macroscopically distinct states are never observed but actual measurements of a physical system always yield a definite result. A famous example in this context is SCHRÖDINGER's cat: a mechanism is built to kill a cat if a radioactive atom decays spontaneously [82]. Before observation and according to the SCHRÖDINGER equation, the cat evolves into a linear combination of states that correspond to a dead cat with decayed atom and an alive cat with undecayed atom. However, by measuring the state of the cat it is always found either alive or dead. Previous probability amplitudes collapse to a sharp result. Here, the importance of the interaction with the environment was recognized by ZEH [83, 84]. In contrast to microscopic systems like electrons, macroscopic systems reveal continuous energy spectra that become quickly correlated to any environment like gas molecules or even cosmic background radiation. Consequently, a macroscopic system can never be described by a pure quantum state. For the derivation of macroscopic properties, the partial trace of the state of the total system is essential [85, 81] and gives information about the degree of coherence.

The phenomenon of decoherence is meanwhile several times confirmed and enables a well controlled handling [86–91]. One exciting example among others is the work of HAROCHE on controllable quantum systems for which he earned the Nobel Prize in 2012 [92]. It enabled the analysis of decoherence by means of time evolution of macroscopic systems and also the development of highly precise optical clocks. Moreover, so called quantum non-demolition (QND) experiments succeeded [93] where a projective measurement does not alter the systems' free evolution. The system can be measured many times with identical observables.

In particular, in the field of quantum information and quantum computing the concept of decoherence is fundamental [94]. The knowledge of decoherence mechanism is important for the growing number of hybrid quantum systems in which long coherence times are needed [95]. With regard to grain boundaries, doping levels and crystal defects, non-destructive sensing of surfaces might be an interesting application of decoherence measurements.

In a time where Google, IBM, Microsoft and many more face a hard marketplace competition for the dominant position in "quantum supremacy" [96, 97], the physics of decoherence belongs to the most thrilling fields of research.

Within this context one goal of this thesis is the study of decoherence of electron superposition states near a conducting gold surface and the comparison with theoretical approaches. Thereby, an existing system from HASSELBACH was adopted and modified. Originally, in this experiment the decoherence of electron matter waves near a doped silicon plate were analysed with regard to COULOMB interaction [66]. However, changing the material of the environment allows to get a deeper insight of the decoherence mechanism and to answer open questions concerning old [98, 99] and new [69, 100] theoretical models. The basic working principle follows thereby a proposal of ANGLIN and ZUREK from 1996 [68] where a biprism interferometer is applied. Coherent electrons are split by a negatively charged biprism fiber, recombined by a quadrupole lens and then superimposed on a detector. Intermediately, the electrons traverse the resistive plate and interact with it. A gradual loss of contrast along the fringes down to the plate level indicates a loss of the coherence properties of the electrons.

However, a key element for all sensitive measurements in the field of electron interferometry remains the particle source which has to be optimized concerning the stability, brightness and coherent emission. Particularly, for studies of the quantum-classical transition via electron superposition states a source is desired which allows to tune the electron energy while being strongly coherent and fixed in place. The energy of an electron corresponds to its velocity and thus, determines the interaction time of the quantum state with the environment.

Most of the sources in former interference experiments were etched metal tips with diameters of several ten nanometers [101]. With the development of new beam sources such as single-atom tips, many more possibilities opened up [102, 103, 3, 5]. By adding a monolayer iridium to a cold field emitter, the emission area can be significantly reduced down to the size of a single atom [104, 70]. Under suitable conditions a pyramidal atom stack is formed at the tip apex due to energetic reasons. The extraction voltage depends on the present electric field strength and also on material and geometrical properties. Slight variations of the geometry on the nanometer scale during the fabrication process of the tip are unavoidable even if progress was made to control the tip profile during the etching process [105]. Consequently, each fabricated tip has its own extraction voltage leading to a different velocity for a given intensity.

Moreover, for a spatially coherent beam the tip radius in electron biprism interferometers was manufactured as small as possible. All to often the extraction voltage decreased, too, resulting in a larger wavelength. The emission signal could then only be increased by raising the tip voltage. Thereby, the electron wavelength was again shortened and smaller fringe distances were caused. This in turn required a stronger magnification which lowered the incoming signal at the detector.

In order to solve this problem a well-known technique from electron microscopy is described and applied successfully in this thesis. Two counter electrodes (apertures) are placed behind the tip. By setting a high voltage to the first one and grounding the second one, a high emission intensity with slow electrons can be achieved. The velocity can be adjusted independently from the emission current. In doing so, not only the intensity is increased without changing the diffraction properties, but also the stress exposure to the tip is minimized and the lifetime is extended [106]. In this thesis it is verified that the lateral and longitudinal coherence of the electrons is not affected by this intensity enhancement process and that the interference properties remain unchanged. It is a useful tool for electron sources in general and their application not only within the context of this thesis but also for electron-diffraction microscopy [107–109], time-resolved ultrafast electron diffraction [110] and for the development of a quantum electron microscope [86, 111].

Single-particle interferometers in general are strongly exposed to external perturbations due to their high phase sensitivity of both beam paths. Small deviations of the partial waves suffice to accumulate a clear phase shift on the detector. Thus, dephasing mechanism like electromagnetic oscillations [4, 112, 2], mechanical vibrations [113, 114] and temperature drifts cause an overall contrast reduction of temporally integrated interference patterns. Especially for sensitive long-time phase measurements it appears as a big challenge to deal with. However, it was recently described that dephasing

effects can in principle be reversed when using spatial and temporal information of the incoming particles [115]. Moreover, dephasing can be used for an accurate determination of the involved perturbation frequencies [116]. By correlating all particles by means of their impact position and time, a full spectrum of the unknown frequencies, their amplitudes, the interference visibility and the fringe distance can be extracted from the dephased pattern. These features make electron matter wave interferometers highly suitable for sensor applications.

For that reason a compact and mechanically stable biprism interferometer is presented in this thesis in which the distances between all optical parts is minimized. Beam path simulations optimized the angle of superposition with regard to realistic magnifications. The portable device demonstrates the universal operation possibility at any place and thus, acts as an important prototype for prospective sensors.

In the context of decoherence measurements of electrons near a gold surface both methods, the enhancement of a coherent electron beam and the improvement of the interferometric properties by means of a correlation analysis, are presented successfully in this thesis.

A further step in the described setup will be the installation of a temperature-dependent environment in which the decoherence strength is varied. In particular, the interaction with a superconducting surface is an interesting undertaking since the concept of a localized mirror charge in the surface becomes inapplicable. Until now, there are no existing theories that give predictions about decoherence of electron superposition states in the vicinity of a superconductor. Probably, an abrupt change of the decoherence rate will occur at the critical temperature.

For that purpose a cryostat system has to be mounted to the interferometer. In this work the planning and general considerations of cooling the gold plate are illustrated. Specific modifications of the interferometer are described and laid underneath with CAD (computer-aided design) drawings. The gold plate is mounted on the cold finger and can achieve temperatures between $2 - 500\,\mathrm{K}$ by using liquid helium or a heating coil. For the vertical movement of the plate, a translation stage ensures fine adjustment of the position. By now, the cryostat is tested successfully only for temperature performances in a separate vacuum chamber. However, the future use in the biprism interferometer for decoherence measurements will allow an easier handling and moving guidance during operation.

In particular, the investigation of decoherence effects of superconductors, but also temperature dependencies for other thrilling materials like vanadium dioxide, is an exciting topic and will exhibit many fascinating results. For a better understanding of the underlying fundamental transition between classical and quantum mechanical physics, this thesis provides new instructive achievements and findings.

In this cumulative thesis, the publications [1, 2] form the basis of the following chapters concerning improvements in electron biprism interferometry and decoherence measurements. Thereby, the interferometer parts and explanations are successively structured and built on one another.

In chapter 2 the working principle of a biprism interferometer is introduced and basic equations are given. Following this, the concept of decoherence is portrayed and relevant theoretical approaches for this thesis are outlined. The theory chapter is concluded with cornerstones of the applied second-order correlation analysis.

Chapter 3 deals with the possibility to increase the signal of an electron beam. Several benefits for interferometry in general are discussed. The preservation of the coherent properties of the beam during field emission with two aperture electrodes is verified and the small energy width of a single-atom tip is confirmed, thus making those type of emitters highly favoured for electron interferometry.

With regard to sensor applications, the correlation analysis is applied to a compact and rigid biprism interferometer in chapter 4. Even with a polycrystalline tungsten tip it is shown that interference fringes are achievable. Potential perturbations are identified and corrected in order to yield a higher fringe visibility. This compact interferometer lays the foundations of a portable sensor device for electromagnetic radiation and also for mechanical vibrations.

All advantages of the previous chapters are combined in chapter 5 where the decoherence measurements of free electrons in the vicinity of a gold surface are analyzed. Adjustment troubles concerning the parallelism of the beam are denominated and possible solutions presented. Most importantly, two theoretical approaches of the problem are ruled out due to the evaluation of the experimental data. However, an exact description of the decoherence process is still difficult.

The cryostat system and its future application is discussed in chapter 6. Detailed drawings and planning considerations are served with regard to the existing setup. Possible materials are pointed out as candidates for the environment.

This thesis ends with a summary of all achieved results and their importance for several applications in basic research. Further improvements of the setup are denoted. Finally, the publications [1, 2] are appended.

2 Theory

In this chapter, the main properties and formulas which form the basis of describing interference phenomena are shown and discussed. They are indispensable for understanding the principle operation of an electron biprism interferometer. Fundamental terms like matter waves, decoherence effects and dephasing mechanisms are introduced.

2.1 Interference

Interference phenomena are always associated with an arbitrary kind of waves. Due to de Broglie [19], not only light but also every particle has a characteristic wavelength

$$\lambda = \frac{h}{p} \tag{2.1}$$

$$= \frac{h}{\sqrt{2m_e e U_e}} \quad . \tag{2.2}$$

Here, h denotes the Planck constant and p the norm of the momentum vector $\vec{p}$ of the particle. Eq. (2.2) is valid for non-relativistic particles accelerated by a potential difference U_e. This is justified for the electrons with mass m_e and elementary charge e in our setup.

Due to the superposition principle, one can calculate the amplitude of a wave field $A(\vec{r},t)$ at an arbitrary point $\vec{r}$ by adding together all incoming wave amplitudes at this point. The observable intensity $I(\vec{r},t)$ is then given as the square of the absolute value of the resulting wave amplitude. For two overlapping matter waves ($j \in \{1,2\}$) of the form

$$A_j(\vec{r},t) = A_j \cdot \exp\left(\mathrm{i}\left(\vec{k_j}\vec{r} - \omega_j t + \varphi_j\right)\right) \quad , \tag{2.3}$$

with wave vector $\vec{k_j}$, frequency ω_j and phase φ_j, one yields

$$I(\vec{r},t) = \left|A_1(\vec{r},t) + A_2(\vec{r},t)\right|^2 \tag{2.4}$$

$$= {A_1}^2 + {A_2}^2 + 2A_1A_2\cos\varphi(\vec{r},t) \quad . \tag{2.5}$$

The interference term of Eq. (2.5) exhibits that the intensity is position- and time-dependent. It is convenient to introduce a definition for the fringe contrast K,

$$K := \frac{I_{max} - I_{min}}{I_{max} + I_{min}} \quad , \tag{2.6}$$

with the maximal and minimal intensities I_{max}, I_{min} [117]. With that, Eq. (2.5) forms to

$$I(\vec{r},t) = I_0\Big(1 + K \cdot \cos\varphi\big(\vec{r},t\big)\Big) \quad , \tag{2.7}$$

where I_0 is the mean intensity of both waves. However, Eq. (2.7) is only valid for point-like and monochromatic electron sources [117]. In reality of course, they have a certain spatial extension and spectral bandwidth which implicates that the contrast is always smaller than unity. Thus, the sum of all waves leads to an incoherent superposition.

In general, coherence describes the phase relation of different waves to each other. One can distinguish between the following:

- **Longitudinal coherence** originates from the source emitting electrons not only with one single energy. The wave vectors differ which can be interpreted as a wave packet. Its coherence length l_c is defined [117] as

$$l_c := \frac{1}{\Delta k} = \frac{\lambda^2}{2\pi\Delta\lambda} = \frac{\lambda}{\pi} \cdot \frac{E}{\Delta E} \quad , \tag{2.8}$$

  with the standard deviations Δk and ΔE. The path difference of two waves must not exceed l_c, otherwise no interference takes place.

- **Transversal coherence** is a result of a finite source size. Each point on the surface contributes to the total emission. Thus, the emitted electrons take different paths and lead to many shifted patterns. The contrast reduces. There is a maximal allowed source size d for which one yield interference fringes. It is expressed in the angular coherence constraint

$$d \cdot \sin\alpha \ll \frac{\lambda}{2} \quad , \tag{2.9}$$

  with the emission angle α.

Based on the concept of Möllenstedt and Düker [22], interference of electrons is achieved by using a thin biprism fibre which acts as a wave front splitter. Just like the optical biprism for light, the electrostatic biprism separates coherently the electron waves and bends all beam paths afterwards if a positive voltage U_f on the fiber is applied. This biprism simply consists of glass coated with a noble metal and has a typical radius r_{BP} of a few hundred nanometer. It is located between two grounded electrodes with distance R.
The angle of deflection γ is calculated [117, 23] to

$$\gamma = \frac{\pi}{2\,ln(R/r_{BP})}\frac{U_f}{U_e} = \gamma_0\frac{U_f}{U_e} \quad . \tag{2.10}$$

It is constant for all beam paths which is depicted schematically in Fig. 2.1. Geometrical considerations lead to the angle of superposition in the interference plane [56]

$$\Theta = \frac{d_{SB}}{d_{SI}}\gamma_0\frac{U_f}{U_e} \quad , \tag{2.11}$$

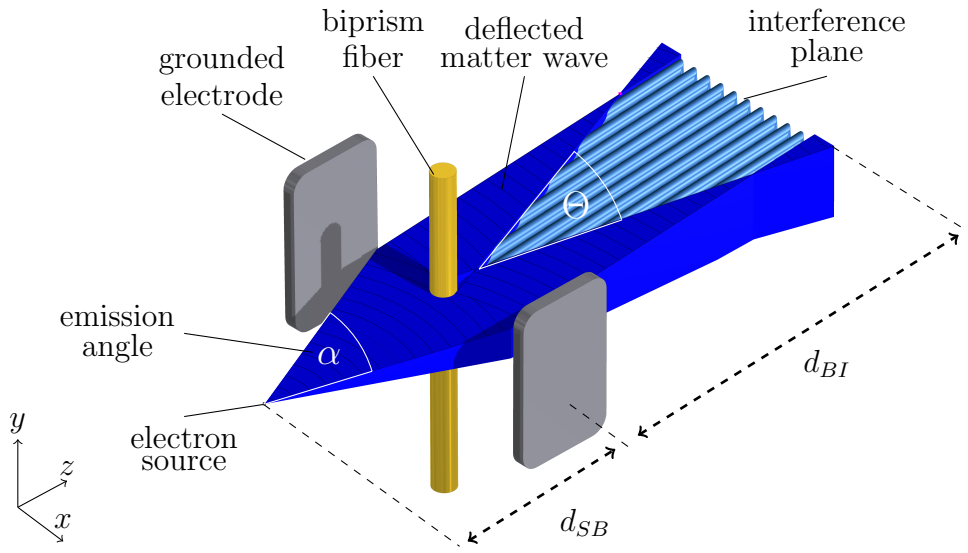

Figure 2.1: Schematic drawing of the principle of operation of a biprism interferometer. The electrons emitted from the source with an angle α illuminate the biprism fiber coherently. Due to the electrostatic potential of the biprism the matter waves get separated and superimpose afterwards with an angle Θ in the interference plane. Grounded electrodes besides the fiber ensure a homogeneous field. The geometrical lengths d_{SB}, d_{BI} and $d_{SI} = d_{SB} + d_{BI}$ determine the fringe distance s according to Eq. (2.13).

where d_{SB} is the distance between source and biprism and d_{SI} between source and interference plane. Together with Eq. (2.7) one can deduce a simple relationship for the fringe distance s in the interference pattern

$$s = \frac{\lambda}{\Theta} \quad , \tag{2.12}$$

and thus

$$s = \frac{h}{\sqrt{2m_e e}} \frac{d_{SI}}{d_{SB}\gamma_0} \frac{\sqrt{U_e}}{U_f} \quad . \tag{2.13}$$

In [117] the finite spatial and chromatic width of real sources are treated by model functions which obey symmetrical and integrable claims. From that, the contrast can be written as

$$K = G_1(\Theta, k_0, \varepsilon) \cdot G_2(\Theta_0, r, \Delta k) \quad , \tag{2.14}$$

with

$$G_1(\Theta, k_0, \varepsilon) = \exp\left(-\frac{1}{2}\left(\frac{d_{BI}}{d_{SB}}\Theta k\varepsilon\right)^2\right) \tag{2.15}$$

$$G_2(\Theta_0, r, \Delta k) = \exp\left(-\frac{1}{2}\left(\Theta_0 r \Delta k\right)^2\right) \quad . \tag{2.16}$$

G_1 causes a uniform contrast reduction for the whole interference pattern due to the source size ε. On the other hand G_2 is dependent of the coordinate r in the interference plane. This portion of contrast reduction is varying along the detector. However, one can estimate quantitative numbers for the number of visible fringes taking into account all geometrical properties. It turns out that the contrast reduction due to the energy width of the source is negligible and therefore, G_2 is set to unity for observing a small number of fringes.

2.2 Decoherence

2.2.1 General considerations

From the beginning of the development of quantum theory, it emerged to be one of the most successful theories of physics. Until today, no discrepancy to any experiment is known. Still, the question why we see a classical world and do not see macroscopic superposition states refers back to the concept of decoherence. From the point of view of quantum theory there is nothing against it. However, such states like the famous cat state are never observed [82]. One approach is to claim the following: a fully conserved quantum system appears to be classical resulting from the irreversible interaction with its environment. In other words: the microscopic object (radioactive atom that decays and releases a poisonous substance) is already entangled with the macroscopic object (cat) which can be considered as a heat bath. This description is somewhat different to the well accepted Copenhagen interpretation in which the wave function of the cat collapses due to opening the box. The importance to describe such paradoxes by their interaction with the environment was recognized by Zeh [84]. Macroscopic systems with their continuous energy spectra are unable to avoid interactions with the environment like air molecules, photons or any other sort of radiation. Thus, it is impossible to describe a macroscopic object by a pure quantum state.

For a better understanding, Anglin and Zurek proposed an experiment [98] where the controllable environment is realized by a resistive plate. The electron and phonon gas inside this plate interacts with a beam of free electrons. It is treated as the quantum system. The beam gets split into two parts, each traversing the plate in a certain height h and with a lateral separation Δx (see Fig. 2.2).

We can write the electron as a superposition state

$$\big(|l\rangle + |r\rangle \big)/\sqrt{2} \tag{2.17}$$

of two left and right moving parts $|l\rangle$ and $|r\rangle$. As the electron moves above the plate, a mirror charge is induced and follows the movement. A disturbance of the electron and phonon gas is the consequence due to ohmic resistance. The state of the combined system before the interaction reads as

$$|\Psi_{before}\rangle = \big(|l\rangle\,|B\rangle + |r\rangle\,|B\rangle \big)/\sqrt{2} \tag{2.18}$$

$$= \big(|l\rangle + |r\rangle \big)\,|B\rangle\,/\sqrt{2} \quad , \tag{2.19}$$

where $|B\rangle$ denotes the state of the gas. After the interaction it changes for each path

now to

$$|\Psi_{after}\rangle = \big(\,|l\rangle\,|L\rangle + |r\rangle\,|R\rangle\,\big)/\sqrt{2} \quad . \tag{2.20}$$

We assume that $\langle L\,|\,R\rangle = 0$ since both states are distinguishable by executing a measurement. Mathematically spoken, an orthogonal basis of the environment is built by these states. The point of view for an external observer has changed because the state in Eq. (2.20) is not a product of two partial states any more. In order to come to know about the properties of the microscopic object alone, a description where only the states of the microscopic object appear is relevant for measurements.
Therefore, density matrices are suited:

$$\rho_{before} = |\Psi_{before}\rangle\,\langle\Psi_{before}| \tag{2.21}$$
$$\rho_{after} = |\Psi_{after}\rangle\,\langle\Psi_{after}| \quad . \tag{2.22}$$

The density matrix of a subsystem comes from building the partial trace of the density matrix of the combined system. The reduced density matrix is then written as

$$\rho_{|x\rangle,before} = Tr_{|X\rangle}\big(\rho_{before}\big) \tag{2.23}$$
$$\rho_{|x\rangle,after} = Tr_{|X\rangle}\big(\rho_{after}\big) \quad , \tag{2.24}$$

whereas $\langle x|$ and $\langle X|$ stand for the system of object and environment, respectively. Considering that the relation

$$Tr_{|X\rangle}(A) = \langle L\,|\,A\,|\,L\rangle + \langle R\,|\,A\,|\,R\rangle \tag{2.25}$$

is valid for any operator A and that the states are normalized

$$\langle L\,|\,L\rangle = \langle R\,|\,R\rangle = 1 \quad , \tag{2.26}$$

the reduced density matrix elements can be calculated to

$$\rho_{|x\rangle,before} = \big(\,|l\rangle + |r\rangle\,\big)\big(\,\langle l| + \langle r|\,\big)/2 \tag{2.27}$$
$$= \big(\,|l\rangle\,\langle l| + |r\rangle\,\langle l| + |l\rangle\,\langle r| + |r\rangle\,\langle r|\,\big)/2 \tag{2.28}$$

and

$$\rho_{|x\rangle,after} = \big(\,|l\rangle\,\langle l| + |r\rangle\,\langle r|\,\big)/2 \quad . \tag{2.29}$$

Clearly, both results show a different prediction for measurements before and after the interaction. In Eq. (2.27) a pure state is given. The object is still in a superposition state. The object is not either in one state $\langle l|$ or $\langle r|$ but can include both. Interference terms exist. On the other hand a mixed state in Eq. (2.29) is indicated where it is impossible to find an expression by a single pure state like $\langle l|$ or $\langle r|$ or else $\langle l| + \langle r|$. When measuring, the statistic ensemble gets determined and the object is either in one state or the other with a probability of 0.5.

Thus, decoherence can be seen as a result from the fact that the environment carries information from the microscopic system after interaction. For example, one could make a measurement of the electron gas in the plate to find out whether it is in the

state $\langle L|$ or $\langle R|$. Is the answer $\langle L|$, then one can conclude that the beam electron followed the left path and is in the state $\langle l|$. $\langle L \,|\, R\rangle = 0$ guarantees that both states of the plate are distinguishable and allows to draw this conclusion.

The experiment with free electrons interacting with a resistive plate has some advantages: like proposed in first theoretical treatments of decoherence [118, 119, 98], the environment is simply realized by ohmic resistance. Furthermore, the microscopic object is an easy-to-manage free electron with zero extension and no inner degrees of freedom. Also, since there are no magnetic fields in the interaction area the spin of the electron is irrelevant.

2.2.2 The proposal of Anglin and Zurek

In 1996 Anglin and Zurek proposed an experiment by using an electron interferometer where the power of decoherence should be adjusted over a wide range [68, 98]. In Fig. 2.2 a sketch of the proposed system is shown. A charged particle traverses a conducting plate along some trajectory and induces an image charge on the surface. While following the particle's movement, bulk currents within the body of the plate are generated. Ohmic resistance is a result due to scattering of electrons with thermal phonons at room temperature. Moreover, a wake of disturbance in the electron and phonon gas goes along with the passage of the beam electron.

After crossing the plate, the disturbed state of the conductive plate remains as a record of the particle's trace. In general, interference can be observed when the joint wave function for two distinct localized states $|l\rangle$ and $|r\rangle$ goes to unity, $\langle \Psi[l] \,|\, \Psi[r]\rangle \to 1$. It means the plate does not distinguish between the two different particle trajectories. Alternatively, a wide separation of the trajectories suppresses the interference and causes a classical probability distribution on the detector.

This setup is considered as well suited for examining decoherence experimentally. The strength is adjustable over a wide range of parameters, namely the path separation Δx, the height h of the electron over the plate or the specific resistivity ρ. Within the flight time the beam electron experiences sufficient interaction in which the decoherence mechanism takes place. Otherwise, the transition from classical to quantum behaviour would not be possible to measure [120].

Attraction of the induced charge: Besides the decoherence studies one might be interested in how the beam electron is attracted towards the plate due to its induced image charge. A quick estimation shall show that this effect plays no role for our experiment. The force component in direction z is according to Coulomb's law

$$F_z = -\frac{1}{4\pi\varepsilon_0}\frac{e^2}{(2z)^2} \quad . \tag{2.30}$$

The velocity component v_z in the direction normal to the plate is then derived to

$$v_z = -\frac{F_z}{m} t_{\text{flight}} \tag{2.31}$$

$$= -\frac{e^2 L}{16\pi\varepsilon_0 m v z^2} \quad , \tag{2.32}$$

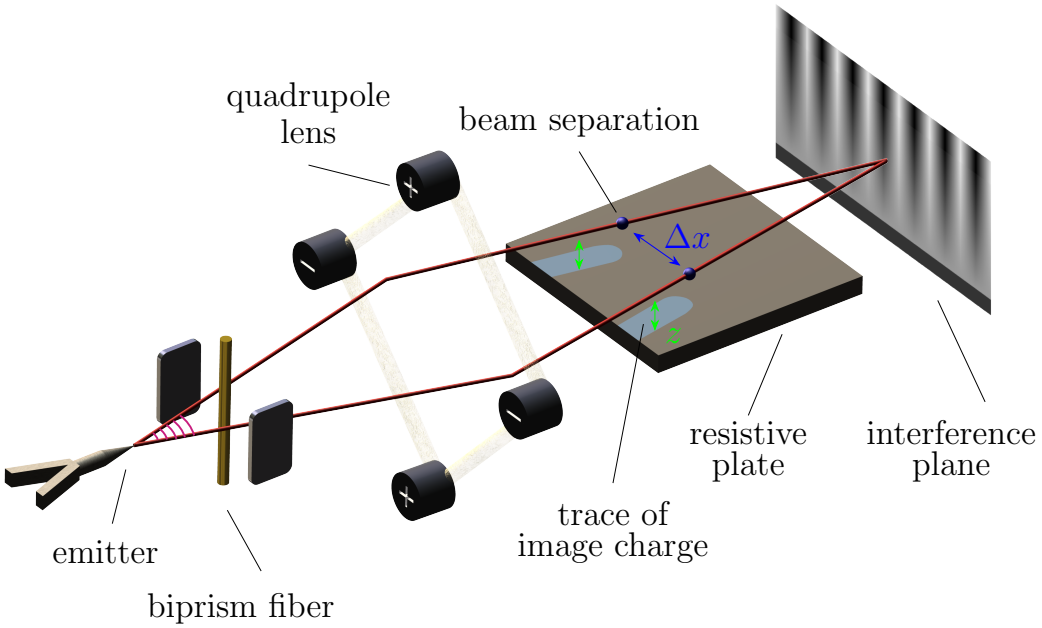

Figure 2.2: Schematic drawing of the purpose of Anglin and Zurek for investigating controlled decoherence of an electron due to the interaction with a resistive plate. The electron trajectory traverses the surface with a height z and is separated by a distance Δx. A loss of visibility in the interference plane arises for small heights above the surface.

with the flight time $t_{\text{flight}} = L/v$ of the electron to pass the plate length L. In the experiment typical values are $L = 10\,\text{mm}$, $z = 10\,\mu\text{m}$ and $v = 0.08\,\text{c}$. A deflection angle $\tan\alpha = \frac{v_z}{v} \approx 10^{-37}$ is the result and can therefore be neglected.

Joule heating: For a homogeneous conductor and a sufficient thick plate Anglin and Zurek calculate the loss of energy of the electron due to classical electromagnetic interactions [68, 121]. This Joule heating is dependent on the velocity v, the height z and the specific resistivity ρ of the conducting plate:

$$P_{\text{Joule}} = -\frac{e^2\rho v^2}{16\pi z^3} \quad . \tag{2.33}$$

For an 1.6 keV electron the loss of energy $\Delta E_{\text{loss}} = P_{\text{Joule}} \cdot t_{\text{flight}}$ is only $\approx 10^{-8}\,\text{eV}$ assuming a gold coated plate surface with $\rho = 2.2 \cdot 10^{-8}\,\Omega\text{m}$. This implies that also the deceleration of the electron due to dissipative heat development is negligible since the energy spread of the electron source is in the order of a tenth eV. The conductivity is considered as constant (independent of frequency and wave vector) because additional plasmonic effects, interband transitions or radiation losses are ruled out.

Interestingly, in the case of adding a thin layer of insulator on top of the plate Eq. (2.33) becomes proportional to the inverse fourth power of z [122, 68]. Thus, the

dependency can be examined with even greater sensitivity. But since gold is a very noble and inert element we do not continue following this finding. However, by using a silicon waver instead of a gold surface this finding may become of importance as the waver lays on the holder made of titan. It will be discussed later.

Decoherence rate: Anglin and Zurek estimate the strength of decoherence by introducing a relaxation time τ_r as a result from the disturbance of the electron and phonon gas [68],

$$\tau_r = \frac{v}{\dot{v}} \quad . \tag{2.34}$$

The acceleration component $\dot{v}$ is calculated by deriving the power loss of Eq. (2.33) with respect to time,

$$P_{\text{Joule}} = \frac{d}{dt}\Big(\frac{mv^2}{2}\Big) = m\,v\,\dot{v} \quad . \tag{2.35}$$

The relaxation time is then given by

$$\tau_r = \frac{16\pi m z^3}{e^2\rho} \quad . \tag{2.36}$$

Furthermore, the full system of plate and beam electron is treated linearly. It grants that the relaxation time is proportional to a certain decoherence rate. Like described in [123], for room temperature a zeroth order approximation is assumed to describe the time decay of a wave packet of a free particle which is connected to a thermal reservoir. The formula for this decoherence time is given for high temperatures and weak coupling (room temperature included),

$$\tau_d = \tau_r\Big(\frac{\lambda_{dB}}{\Delta x}\Big)^2 \quad . \tag{2.37}$$

Here, $\lambda_{dB} = h/\sqrt{2mk_BT}$ denotes the thermal de Broglie wavelength. Inserting it into Eq. (2.37) gives the following form:

$$\tau_d = \tau_r\Big(\frac{h^2}{2mk_BT(\Delta x)^2}\Big) \quad . \tag{2.38}$$

A few years later Joos, Breuer and Petruccione receive a slightly different result [81, 124]. They also examine the effect of coupling a massive object to a thermal reservoir but declare prefactors in a master equation elsewise. It is given as

$$\tau_d = \tau_r\Big(\frac{h^2}{4\pi^2mk_BT(\Delta x)^2}\Big) \quad , \tag{2.39}$$

where a factor of $1/2\pi^2$ is added. Zurek in turn ends up with the same outcome in his paper [49] which seems to be more accurate. Finally, the decoherence time for a linear model with a conducting plate has the following expression:

$$\tau_d = \frac{4h^2z^3}{\pi e^2k_BT\rho(\Delta x)^2} \quad . \tag{2.40}$$

Four parameters can be varied experimentally. The temperature T and resistivity ρ of the plate as material properties and the separation Δx and height z as beam attributes. The latter ones allow for a higher sensitivity among their variation. Moreover, Eq. (2.40) is independent from the velocity and mass of the electrons flying above the plate. However, Eq. (2.40) is only valid within the limitations of a sufficient high temperature. Also the beam separation must not be too big. If the distance between the two disturbances of the electron gas (which follow the beam electrons) is bigger than their extent then a further separation will have no consequence. The decoherence is expected to saturate. Anglin and Zurek specify this distance in the range of the correlation length in the electron gas [68]. A bunch of exemplary values for τ_d is shown in Tab. 2.1: The quantity to be measured in our experiment is the contrast K of the

$z\,[\mu m]$ \ $\Delta x\,[\mu m]$	1	10	100
1	$2.4 \cdot 10^{-7}$	$2.4 \cdot 10^{-9}$	$2.4 \cdot 10^{-11}$
	$(3.6 \cdot 10^{-13})$	$(3.6 \cdot 10^{-15})$	$(3.6 \cdot 10^{-17})$
10	$2.4 \cdot 10^{-4}$	$2.4 \cdot 10^{-6}$	$2.4 \cdot 10^{-8}$
	$(3.6 \cdot 10^{-10})$	$(3.6 \cdot 10^{-12})$	$(3.6 \cdot 10^{-14})$
100	$2.4 \cdot 10^{-1}$	$2.4 \cdot 10^{-3}$	$2.4 \cdot 10^{-5}$
	$(3.6 \cdot 10^{-7})$	$(3.6 \cdot 10^{-9})$	$(3.6 \cdot 10^{-11})$

Table 2.1: τ_d in seconds for gold ($\rho = 2.2 \cdot 10^{-8}\,\Omega\mathrm{m}$) at room temperature ($T = 293.15\,\mathrm{K}$). The values in brackets correspond to the resistivity of a n-doped silicon wafer ($\rho = 1.5 \cdot 10^{-2}\,\Omega\mathrm{m}$).

interference pattern. It provides information about the coherence of our beam electron. Assuming that only the decoherence effect with the plate is responsible for decreasing the contrast its dependence of z is then given by the exponential function of the ratio between flight time τ_{flight} and decoherence time τ_d:

$$K = \mathrm{e}^{-\frac{\tau_{\text{flight}}}{\tau_d}} \tag{2.41}$$

$$= \exp\Big(-\frac{\pi e^2 k_B T \rho L (\Delta x)^2}{4h^2 v z^3}\Big) \quad . \tag{2.42}$$

The loss of contrast increases with decreasing velocity due to a extended interaction time over the plate. In Fig. 2.3 the expected graph of Eq. (2.42) is plotted. One can see two regions where the contrast does not vary. For small heights the contrast is completely lost since the decoherence is very strong. This is the classical regime. For large heights the contrast approaches to unity where the electron beholds its quantum

properties and the ability to interfere. Between those extremal regions there must be a continuous transition from classical to quantum behaviour. It can be recognized in Fig. 2.3 at $z \approx 0.7\,\mu$m for gold and $z \approx 60\,\mu$m for silicon.

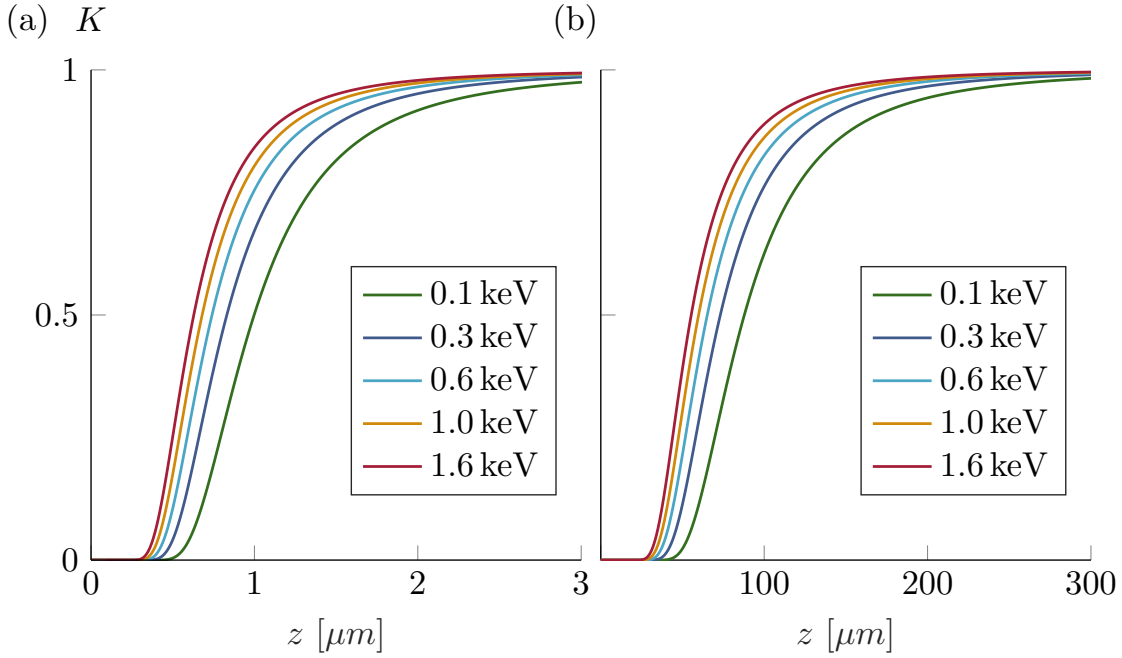

Figure 2.3: (a) Plot of the fringe visibility K as a function of the height z above a 10 mm long gold surface for different electron energies. The transition between the two limits is very narrow within a few μm for a beam separation of $\Delta x = 10\,\mu$m. (b) A similar figure is shown for silicon. Here, the transition lies at approximately hundred times higher z.

2.2.3 The theory of Machnikowski

Against the background of Anglin 's and Zurek 's proposal [68] and with the feasibility to create interference fringes with free single electrons in an electron interferometer [125, 126] Machnikowski was encouraged to develop a fully quantum description of the electron decoherence according to the specific experimental conditions [99, 127, 128]. His approach starts from the fact that a which path information is gained from the overlap between the spectral density of the electron reservoir fluctuations and the spectral function of the unperturbed system [129]. Here, the fluctuations are simply treated as the dielectric function of the metal. A single electron is chosen to have a narrow Gaussian wave packet shape (compared to any experimental geometrical length) which does not show significant dispersion effects for the given velocities of $v \approx 10^7$ m/s. Moreover, the time interval of consecutive emitted electrons is larger than the relaxation time of the plate ensuring each flight event to be independent [99]. For the Hamiltonian H describing the Coulomb interaction between beam electron and electrons and ions in the plate Machnikowski uses the Coulomb gauge,

$$H = \frac{e^2}{4\pi\varepsilon_0} \int \mathrm{d}^3 r \int \mathrm{d}^3 r' \, \frac{\rho_B(r)\rho_C(r')}{|r - r'|} \quad , \tag{2.43}$$

where $\rho_B(r)$ is the density operator for the beam electron and $\rho_C(r')$ the charge density at a point r' in the metallic plate. Assuming that the initial state of the combined system can be written as a direct product of the initial state of the electron and the thermal state of equilibrium of the electron gas, MACHNIKOWSKI performs the calculation of the reduced density matrix of beam electron and charges in the plate. In order to avoid going too much into detail, only the the result

$$K = \exp\Big(-\frac{L}{\lambda_{\mathrm{dec}}}\Big) \quad , \tag{2.44}$$

for the fringe visibility K is shown [99]. λ_{dec} acts as a decoherence rate per unit length over the plate. It is now essential to evaluate this parameter. Provided that the plate is bulky and surface effects can be neglected, a general expression by means of the fluctuation-dissipation theorem is derived. For the correlation of the two elements of the reduced density matrix the imaginary part of the dielectric function $\varepsilon_d(\mathbf{q},\omega)$ becomes relevant. The formula for λ_{dec} is computed to

$$\lambda_{\mathrm{dec}}^{-1} = \frac{k_B T}{2\pi^2 \hbar\, v}\gamma\Big(\frac{\Delta x}{z}\Big)\,\mu\Big(\frac{m_{\mathrm{eff}}\, e^2}{2\pi\varepsilon_0\varepsilon_i\hbar^2 k_F}\Big) \quad , \tag{2.45}$$

with the geometrical function

$$\gamma(\zeta) = \frac{1}{2}\int_{-\infty}^{\infty}\frac{1}{1+u^2}\ln\Big(1+\frac{\zeta^2}{4}\frac{u^2}{1+u^2}\Big)\,\mathrm{d}u = \frac{\pi}{16}\zeta^2 + \mathcal{O}(\zeta^4) \quad , \tag{2.46}$$

and the material dependent function

$$\mu(\xi) = \frac{\xi^2}{4}\int_0^1 \frac{1}{u^3}\Big(1+\frac{\xi}{4\pi u^2}\Big(1+\frac{1-u^2}{2u}\ln\Big(\frac{1+u}{1-u}\Big)\Big)\Big)^{-2}\,\mathrm{d}u \quad . \tag{2.47}$$

Here, m_{eff} is the effective mass of the electrons in metal, $\varepsilon_i = 1+\chi_{\mathrm{phonon}}(\omega=0)$ the dielectric constant and k_F the FERMI wave number.

In Fig. 2.4 the result of MACHNIKOWSKI 's calculations for metal is shown. Compared to the result (2.42) of ANGLIN and ZUREK the contrast here shows the same dependency of the plate length L, temperature T and electron velocity v. However, according to Eq. (2.46) it shows also a dependency of the ratio of the beam separation and height which goes along with the square of $\Delta x/z$. This $1/z^2$ dependency of the contrast for MACHNIKOWSKI's calculation is different to the $1/z^3$ dependency of ANGLIN and ZUREK. Furthermore, the decoherence rate for practically all metals is many orders of magnitude higher than expected by ANGLIN and ZUREK. This is due to a different decoherence mechanism where the formation of the image charge is already dissipative. There is no need of carrier-phonon scattering and thus, the Ohmic resistance is of minor importance. In [99] MACHNIKOWSKI states that "the decoherence effect will be qualitatively similar for any plate material (e.g. for semiconductors) as long as the electron gas response is dominated by the low-frequency sector". This can be seen in the decoherence rate where no resistivity ρ appears any more.

2.2.4 The theory of Karstens and Scheel

In her master thesis, KARSTENS describes path decoherence effects for both, electrons and ions, by investigating the dielectric properties of the plate [100]. The decoherence

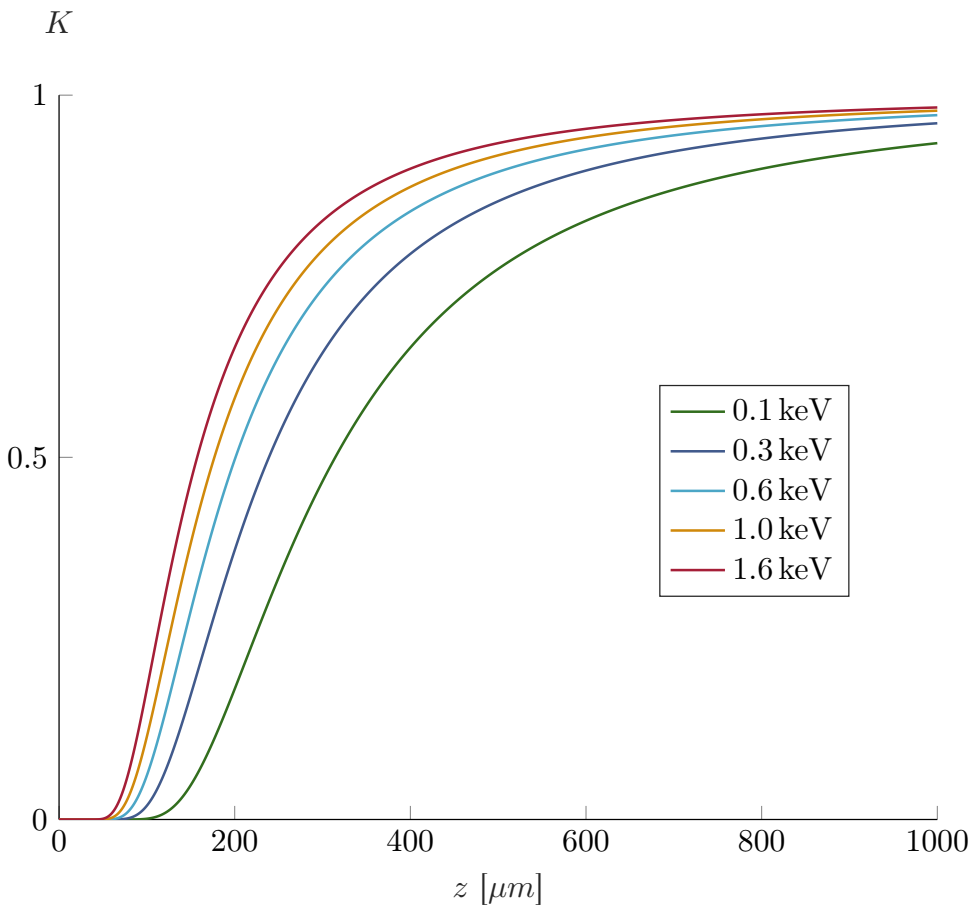

Figure 2.4: Plot of the contrast K against the height z for different electron energies according to MACHNIKOWSKI 's calculations [99]. Here, a beam separation of 10 μm and a plate length of 10 mm is assumed. The decoherence effect becomes significant between $z = 100\,\mu$m and $z = 300\,\mu$m.

rates are deduced by means of the decoherence functional ansatz which is introduced and portrayed in [124]. For the evaluation of this functional ansatz, macroscopic quantum electrodynamics is used in the presence of absorbing media.

Consider an open quantum system Q coupled to an environment E. The Hamiltonian $\hat{H}$ is split into

$$\hat{H} = \underbrace{\hat{H}_Q + \hat{H}_E}_{\hat{H}_0} + \hat{H}_I \quad , \tag{2.48}$$

where $\hat{H}_Q$ and $\hat{H}_E$ denote the Hamiltonians for each subsystem. The interaction of Q and E is described by an operator of the form

$$\hat{H}_I = \sum_n |n\rangle \langle n| \otimes \hat{E}_n(t) \quad , \tag{2.49}$$

with time-invariant basis vectors $|n\rangle$ of states of the system. The time evolution of the complete system is only specified by a general operator

$$\hat{E}_n(t) = e^{i\hat{H}_0 t} \hat{E}_n(0) e^{-i\hat{H}_0 t} \quad . \tag{2.50}$$

A state $|\Psi\rangle$ of the coupled system is a superposition of product states of the quantum system and the environment. Since the time evolution operator is applied only on arbitrary states $|\phi_E\rangle$ of the environment, a fix state $|n\rangle$ gets entangled with a state of the environment. Moreover, the states $|n\rangle$ are not affected by a measurement of the system. At this point, the introduction of the density operator $\hat{\rho}$ is reasonable as it describes in terms of probabilities c_n, in which particular state $|\Psi_n\rangle$ a system is. In bra-ket notation, the density operator is of the form

$$\hat{\rho} = \sum_n c_n \left|\Psi_n\right\rangle \left\langle\Psi_n\right| \quad , \tag{2.51}$$

with $\sum_n c_n = 1$ and $\mathrm{Tr}(\hat{\rho}) = 1$. Using the latter, one can show that $\langle\hat{\rho}\rangle \leq 1$. It is equal to unity if $\hat{\rho}$ describes one pure state. Furthermore, the expectation value of an observable A is given by $\langle A\rangle_{\Psi_n} = \langle\Psi_n|\,\hat{A}\,|\Psi_n\rangle$. The mean value of a mixture of system states has to take into account the weighted sum of each expectation values:

$$\langle A\rangle_{\hat{\rho}} = \sum_n c_n \left\langle\Psi_n\right|\hat{A}\left|\Psi_n\right\rangle \quad . \tag{2.52}$$

It turns out to be

$$\langle A\rangle_{\hat{\rho}} = \mathrm{Tr}(\hat{\rho}\hat{A}) \quad . \tag{2.53}$$

Thus, all expectation values can be calculated with the density operator. It contains the maximum information, which can be obtained by measuring a system. Generally, for the two systems Q and E a reduced density operator $\hat{\rho}_r$ serves to describe the properties of Q without looking on the complete system. $\hat{\rho}_r$ for the quantum system Q emerges from taking the partial trace of $\hat{\rho}$ over E:

$$\hat{\rho}_r(t) = \sum_{n,m} c_n c_m^* \left|n\right\rangle \left\langle m\right| \langle\phi_{E_m}(t)|\phi_{E_n}(t)\rangle \quad . \tag{2.54}$$

From Eq. (2.54) the dynamic of the diagonal elements $\langle n|\,\hat{\rho}_r(t)\,|m\rangle$ is simply given by the overlap of the states of the environment E:

$$|\langle\phi_{E_n}(t)|\phi_{E_m}(t)\rangle| = e^{\Gamma_{nm}(t)}, \qquad \Gamma_{nm}(t) \leq 0 \quad . \tag{2.55}$$

The specific time characteristics of $\Gamma_{nm}(t)$ strongly depends on the interaction strength between Q and E and its inner degrees of freedom. Mostly, this leads to a rapid decay of all side diagonal elements after a time τ_d. The reduced density operator becomes the sum of all diagonal elements and contains no coherent superposition any more [120, 81]:

$$\hat{\rho}_r(t) \xrightarrow{t\gg\tau_d} \sum_n |c_n|^2 \left|n\right\rangle \left\langle n\right| \quad . \tag{2.56}$$

The time evolution of $\hat{\rho}_r(t)$ follows from the Schrödinger equation and is expressed in the von Neumann equation [130]

$$\frac{\mathrm{d}\hat{\rho}}{\mathrm{d}t} = -\frac{i}{\hbar}[\hat{H}_I(t), \hat{\rho}(t)] \quad . \tag{2.57}$$

Here, $[\hat{H}, \hat{\rho}] = \hat{H}\hat{\rho} - \hat{\rho}\hat{H}$ is a commutator. The general solution is given by

$$\hat{\rho}(t) = \hat{U}(t)\hat{\rho}(0)\hat{U}^{\dagger}(t) \quad . \tag{2.58}$$

with the time evolution operator $\hat{U}(t) = \exp\big(-\frac{i}{\hbar}\hat{H}\cdot(t-t_0)\big)$ and its adjoint operator $\hat{U}(t)^{\dagger}$. Karstens shows that the decoherence functional $\Gamma_{nm}(t)$ essentially increases with the square of the time t [100]. In general, solving Eq. (2.57) is a very complex challenge. In [124] an approach is presented where the Hamiltonian is separated into two parts: one for the Coulomb interaction within the material and one for the interaction of the material with the electromagnetic radiation field. Moreover, several assumptions are made:

- The initial state is of the form $\hat{\rho}(t_i) = \hat{\rho}_M(t_i) \otimes \hat{\rho}_F$ where the radiation field $\hat{\rho}_F$ is thermally stable with temperature T. This product state clearly neglects all former correlations between both systems. The interaction starts initially at time t_i. Calculating the trace then leads to the reduced density matrix elements of the material at t_i.

- The Compton wavelength is small and the current densities are classical. No radiation scattering effects take place.

- Separated particle trajectories have the same energy. That is fulfilled since the beam is only deflected by the biprism with no further electronic influence.

Further considerations point out that a macroscopic quantum electrodynamics is needed to treat electric fields in the decoherence functional $\Gamma_{nm}(t)$ in presence of a resistive plate. In this phenomenological description based on the Maxwell equations the optical properties of the plate are included by means of the dielectric permittivity $\varepsilon(\mathbf{r}, \omega)$ and the magnetic permeability $\mu(\mathbf{r}, \omega)$.
The decoherence rate for electrons is calculated in [100] based on the multipole expansion of the current densities in the decoherence functional $\Gamma_{nm}(t)$. Only the monopole moment is relevant for electrons due to their missing inner structure.
For our experiment, the limit of high temperatures ($\hbar\omega \ll k_B T$) is valid for the evaluation of the decoherence functional.
Also, a Markov approximation is used assuming that the interaction time is large compared to correlation times within the reservoir (plate). After coupling to the beam electron the plate returns to its initial state instantaneously.

Finally, Karstens comes to the following result for the decoherence functional where the height z and beam separation Δx are adjustable parameters [100]:

$$\Gamma = -\frac{e^2 t}{4\pi^2 \varepsilon_0 \hbar} \int_{-\infty}^{\infty}\int_{-\infty}^{\infty} \mathrm{d}k_x\, \mathrm{d}k_y \left(1 - \cos\left(k_x \Delta x\right)\right) \cdot \left(2n_{\mathrm{th}}|k_y v| + 1\right) \cdot \frac{e^{-2k_{\parallel}\gamma_k \cdot z}}{2k_{\parallel}\gamma_k} \cdot \mathrm{Im}\left(r_p \gamma_k^2 + r_n \frac{v^2}{c^2}\frac{k_x^2}{k_{\parallel}^2}\right) \quad . \tag{2.59}$$

Here, $k_z = \sqrt{\frac{\omega^2}{c^2} - k_{\parallel}^2}$ denotes the component of the wave vector normal to the surface with $k_{\parallel} = \sqrt{k_x^2 + k_y^2}$. The mean thermal photon number is approximated to $n_{\mathrm{th}} = \frac{2k_B T}{\hbar|k_y v|}$.

The factor $\gamma_k = \sqrt{1 - \left(\frac{v}{c}\frac{k_y}{k_\parallel}\right)^2}$ is nearly one for non-relativistic velocities. Moreover, the FRESNEL coefficients for polarized waves parallel (r_p) and normal (r_n) to the surface are given as

$$r_p = \frac{\epsilon(\omega)k_z - k_{z1}}{\epsilon(\omega)k_z + k_{z1}} \quad , \quad r_n = \frac{k_z - k_{z1}}{k_z + k_{z1}} \quad . \tag{2.60}$$

Thereby, $k_{z1} = \sqrt{\frac{\omega^2}{c^2}\epsilon(\omega) - k_\parallel^2}$ represents the component of the wave vector normal to the surface within the medium. Obviously, the permittivity $\epsilon(\omega)$ is of crucial importance for the interaction between beam electron and plate material. By means of the DRUDE model for metals it can be written as

$$\epsilon(\omega) = 1 - \frac{\omega_p^2}{\omega(\omega + i\gamma_r)} = 1 - \frac{\omega_p^2}{\omega^2 + \gamma_r^2} + i\frac{\omega_p^2\gamma_r}{\omega(\omega^2 + \gamma_r^2)} = \epsilon_1 + i\epsilon_2 \tag{2.61}$$

For gold the plasma oscillation frequency is $\omega_p = 1.37 \cdot 10^{16}\,\mathrm{Hz}$ and the relaxation rate $\gamma_r = 4.12 \cdot 10^{13}\,\mathrm{Hz}$ [131].
Fig. 2.5 illustrates the visibility $K = e^{\Gamma}$ with regard to Eq. (2.59) for different electron energies.

2.3 Dephasing correction

In this section, a short review of the dephasing correction method is given following the publications [4, 112, 116]. This method was applied in the present thesis since a delay line detector is used which releases spatial and temporal information of the incoming particles.

Considering a perfect double-slit experiment, the spatial interference pattern is built by detecting single particles and their individual points of impact. The intensity distribution follows from the temporal integration of all impacting particles and becomes the sum of the probability distribution of every individual particle for infinitely many of them. The pattern then stays fix with a certain fringe distance s. However, besides decoherence mechanism also dephasing effects typically reduce contrast. It is due to a collective time-dependent phase shift of the wave functions. Even with greatest effort it is a hopeless undertaking getting rid of all disturbing sources and external influences. Perturbation and noise lurk everywhere: vibrations from the building, fluctuations of the voltage supply units, mains hum of the electric network, electromagnetic radiation or simply acoustic noise. Electrons get affected by these emergences as they might lose their phase relation. Thus, the interference pattern blurs out and the spatial contrast K on the detector screen decreases. In contrast to decoherence, dephasing can be reversed. In [4, 112, 113, 116] a general method is shown by applying a second-order correlation analysis to the interference pattern.

Starting with a probability distribution $f(x,t)$ of incoming particles on the dectector,

$$f(x,t) = f_0\left(1 + K\cos\left(\frac{2\pi}{s}x + \phi(t)\right)\right) \quad , \tag{2.62}$$

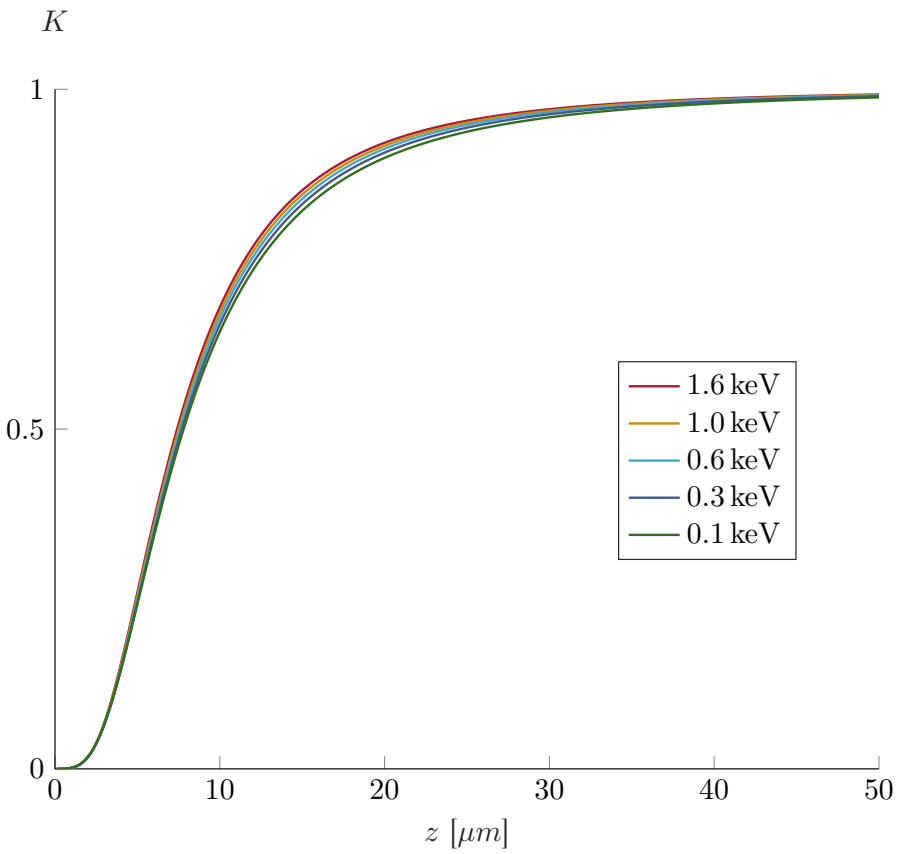

Figure 2.5: The visibility K of decohering electrons over a 10 mm long gold plate is shown for different heights z and a beam separation of $\Delta x = 10\,\mu$m according to the theory of [100, 69]. The dependency of the electron energy is less distinctive than for the two other theories.

a perturbation is manifested in the time-dependent phase $\phi(t)$. f_0 is a normalization factor and s the fringe periodicity. For a harmonic oscillation with frequency ω_1 and amplitude φ_1, Eq. (2.62) reads as

$$f(x,t) = f_0\left(1 + K\cos\left(\frac{2\pi}{s}x + \varphi_1\cos\left(\omega_1 t + \phi_1\right)\right)\right) \quad , \tag{2.63}$$

with an arbitrary phase ϕ_1. Since the interference fringes are orientated in y-direction only the x-position is relevant. Integrating $f(x,t)$ over time leads to a reduced contrast $K_{\mathrm{red}}(\varphi_1)$ dependent on the amplitude of the perturbation. This can be seen by calculating the time average integral of the probability function:

$$\langle f(x,t)\rangle_t = \lim_{T\to\infty}\frac{1}{T}\int_0^T f(x,t)\,\mathrm{d}t \tag{2.64}$$

$$= f_0\left(1 + \underbrace{K J_0(\varphi_1)}_{K_{\mathrm{red}}(\varphi_1)}\cos\left(\frac{2\pi}{s}x\right)\right) \quad . \tag{2.65}$$

A crucial factor is hereby the zero order Bessel function $J_0(\varphi_1)$ of first kind with $|J_0(\varphi_1)| \leq 1$. It implies that the perturbed contrast K_{red} is always less or equal to

the unperturbed contrast K. $J_0(\varphi_1 = 0) = 1$ ensures the maximum contrast when no perturbation is given.

The task is now to calculate K from a perturbed measurement. Therefore, the time information of the detector becomes essential. For a single frequency perturbation it turns out that not only the unperturbed contrast can be revealed by using a second-order correlation function, but also the other properties of the perturbation ω_1, φ_1 and even ϕ_1 [4, 116]. The second-order correlation function $g^{(2)}(u,\tau)$ is defined as

$$g^{(2)}(u,\tau) \equiv \frac{\left\langle\!\left\langle f(x+u,t+\tau)\cdot f(x,t)\right\rangle\!\right\rangle_{x,t}}{\left\langle\!\left\langle f(x+u,t+\tau)\right\rangle\!\right\rangle_{x,t}\left\langle\!\left\langle f(x,t)\right\rangle\!\right\rangle_{x,t}} \quad , \tag{2.66}$$

with the average time and position integral

$$\left\langle\!\left\langle f(x,t)\right\rangle\!\right\rangle_{x,t} = \lim_{X,T\to\infty}\frac{1}{XT}\int_0^T\int_{-\frac{X}{2}}^{\frac{X}{2}} f(x,t)\,\mathrm{d}x\,\mathrm{d}t \quad . \tag{2.67}$$

Applying the second-order function to Eq. (2.63), one yields

$$g^{(2)}(u,\tau) = 1 + \frac{K^2}{2}A(\tau)\cos\left(\frac{2\pi}{s}u\right) \quad , \tag{2.68}$$

with the time-dependent amplitude

$$A(\tau) = \sum_{m=-\infty}^{\infty} J_m(\varphi_1)^2\cos\left(m\omega_1\tau\right) \quad . \tag{2.69}$$

The interpretation is the following: the second-order correlation function, centered around 1, is modulated by a spatial distance u between two detection events. Importantly, the fringe periodicity stays the same as in the unperturbed case. However, the amplitude of the modulation varies with the correlation time τ. Since $A(\tau = 0) = 1$ the perturbation frequency drops out of Eq. (2.68) for $\tau = 0$, thus enabling K and s to evaluate:

$$g^{(2)}(u,0) = 1 + \frac{K^2}{2}\cos\left(\frac{2\pi}{s}u\right) \quad . \tag{2.70}$$

In k-space $A(\tau)$ characterizes a superposition of infinite many sidebands at discrete frequencies $m\omega_1$ ($m \in \mathbb{Z}$). Thus, an amplitude spectrum with characteristic peaks, separated by s, exists.

To identify these frequencies a Fourier transform of the correlation function has to be executed as it describes the power spectrum of the perturbed data according to the Wiener-Khintchine theorem [132, 133]. It is defined by

$$\left|\mathcal{F}\Big(g^{(2)}\big(u,\tau\big)\Big)\big(u,\omega\big)\right| = \left|\frac{1}{\sqrt{2\pi}}\int_{-\infty}^{\infty} g^{(2)}\big(u,\tau\big)\mathrm{e}^{i\omega\tau}\mathrm{d}\tau\right| \quad . \tag{2.71}$$

With that, Eq. (2.68) becomes

$$\frac{1}{2\pi}\left|\mathcal{F}\Big(g^{(2)}\big(u,\tau\big)\Big)\big(u,\omega\big)\right|^2 = \delta(\omega)^2 + \tag{2.72}$$

$$\left(\frac{K^2}{2}\cos\left(\frac{2\pi}{s}u\right)\sum_{m=-\infty}^{\infty} J_m(\varphi_1)^2\Big(\delta(\omega+m\omega_1)+\delta(\omega-m\omega_1)\Big)\right)^2 \quad , \tag{2.73}$$

where $\delta(\omega)$ denotes the DIRAC delta function. The spatial periodicity in the amplitude spectrum remains the same as for the unperturbed interference pattern whereas the amplitude of the modulation in u-direction is given by the square of the BESSEL functions. The average $\mathcal{G}$ of the amplitude spectrum indicates the height of the m-th peak to

$$\mathcal{G}(m\omega_1) = \frac{K^2}{2} J_m(\varphi_1)^2 \quad . \tag{2.74}$$

Until so far the perturbation frequency ω_1 and the amplitude φ_1 of Eq. (2.63) can be calculated. The determination of the phase ϕ_1 is described in [113]. The aim is to reconstruct the complete interference pattern. For this, new coordinates $x_{i,\mathrm{new}}$ of the particles have to be determined by the following relation:

$$x_{i,\mathrm{new}} = x_i - \frac{s}{2\pi}\varphi_1(t_i)\cos\left(\omega_1 t_i + \phi_1\right) \quad . \tag{2.75}$$

The phase is obtained by varying φ_1, ω_1 and ϕ_1 with respect to maximize the contrast of the reconstructed pattern.

For the determination of the spatial perturbation amplitude b_1 we assume that the perturbation takes place before the pattern is magnified by the quadrupole lens. This is reasonable since perturbations affect small structures significantly stronger. b_1 is derived for each perturbation frequency ω_1 with its amplitude φ_1 and the theoretical fringe distance s_0 by

$$b_1 = s_0 \cdot \frac{\varphi_1}{2\pi} \quad . \tag{2.76}$$

In order to handle the experimental data from the detector one has to consider a numerical second-order correlation function $g^{(2)}(u,\tau)_{\Delta u,\Delta\tau}$ with discretized variables Δu and $\Delta\tau$ of spatial distance u and time interval τ,

$$g^{(2)}(u,\tau)_{\Delta u,\Delta\tau} = \frac{1}{\Delta u \Delta\tau} \int_{u-\frac{\Delta u}{2}}^{u+\frac{\Delta u}{2}} \int_{\tau-\frac{\Delta\tau}{2}}^{\tau+\frac{\Delta\tau}{2}} g^{(2)}(u,\tau)\,\mathrm{d}\tau\,\mathrm{d}u \tag{2.77}$$

$$= \frac{TX}{N^2}\frac{1}{\Delta u\Delta\tau} \underbrace{\int_{u-\frac{\Delta u}{2}}^{u+\frac{\Delta u}{2}} \int_{\tau-\frac{\Delta\tau}{2}}^{\tau+\frac{\Delta\tau}{2}} \sum_{i,j=1}^{N} \delta(\tau + t_i - t_j)\delta(u + x_i - x_j)\,\mathrm{d}\tau\,\mathrm{d}u}_{N_{u,\tau}} \quad . \tag{2.78}$$

$N_{u,\tau}$ is the number of particle pairs (i,j) with distances $(x_i - x_j) \in [u - \frac{\Delta u}{2}, u + \frac{\Delta u}{2}]$ and time differences $(t_i - t_j) \in [\tau - \frac{\Delta\tau}{2}, \tau + \frac{\Delta\tau}{2}]$. Since the detector area with diameter X and the acquisition time T is limited, the probability of a particle impact is corrected by a factor of $(1 - \tau/T)$ and $(1 - |u|/X)$. Eq. (2.78) is then modified to

$$g^{(2)}(u,\tau)_{\Delta u,\Delta\tau} = \frac{TX}{N^2}\frac{1}{\Delta u\Delta\tau}\frac{N_{u,\tau}}{(1-\frac{\tau}{T})(1-\frac{|u|}{X})} \quad . \tag{2.79}$$

In [116] the influence of noise on the calculated properties of the perturbance is discussed. In general, the Poissonian distribution of emitted particles sets a limit to resolve

minimal frequencies and amplitudes. It can be found that a spatial discretization step size of

$$\Delta u = 0.371 \cdot s \quad . \tag{2.80}$$

leads to a maximal signal-to-noise ratio. In particular, for sensor applications one is interested in the lower limit to identify small amplitudes $\varphi_{1,\min}$. A formula is given in [116] for the threshold where the noise reaches the signal level:

$$\varphi_{1,\min} = 0.8842\ \pi \cdot \frac{\left(X/s\right)^{\frac{1}{4}}}{KN^{\frac{1}{2}} \cdot \left(\tau_{\max}/T\right)^{\frac{1}{4}}} \quad . \tag{2.81}$$

Thus, for measuring small amplitudes a high contrast and a large number of detected particles is desired to achieve.

3 Intensity amplification

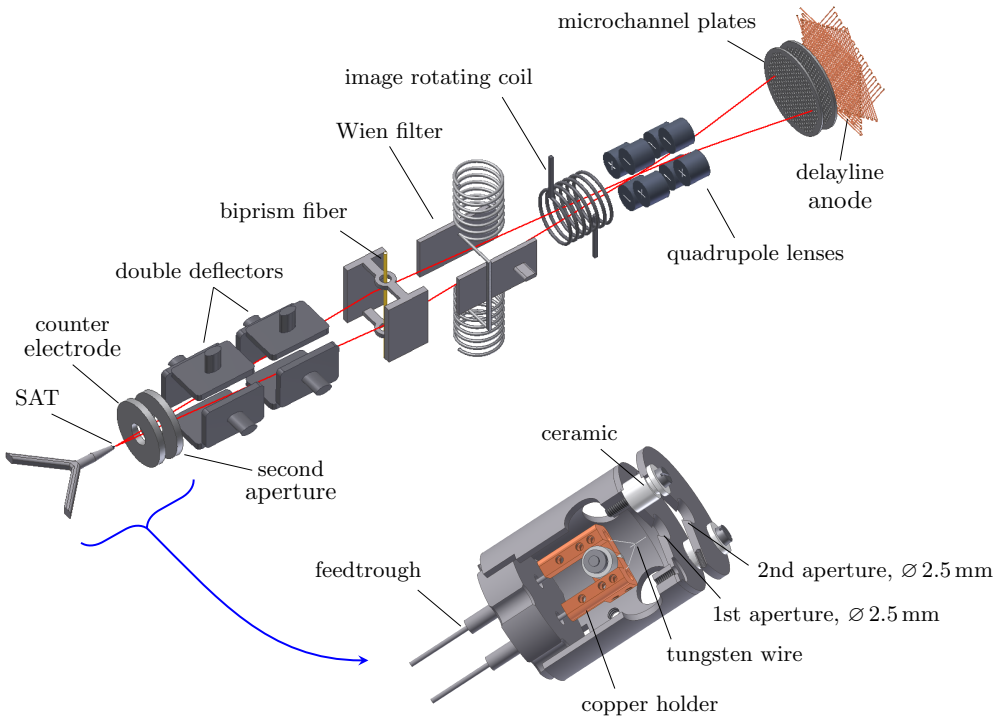

Figure 3.1: Schematic sketch of the setup for measuring the coherent properties of an electron beam which is intensity enhanced. The red line corresponds to a possible separated beam path through the interferometer. A detailed mechanical drawing of the electron source assembly is shown also where two apertures are positioned in front of the tip [1].

A general challenge in various quantum experiments and applications is to develop suitable sources of coherent particles. For instance, in the field of microscopy, interferometry, metrology or material analysis [134, 3, 103, 135], intensive coherent sources for free electron matter waves are strongly desired. Moreover, for the measurement of COULOMB-induced decoherence of an electron superposition close to a metallic or even superconducting surface, a source with tunable electron energy and constant coherence properties at the same time is a beneficial feature.

The decoherence study of electron waves near a semiconducting plate was carried out only with one electron energy, namely 1.665 keV [66]. However, in order to test different theoretical approaches and to expand the study to a wide range of parameters [98, 99, 69], more effort has to be done for the improvement of the experimental setting. Also, as changing the electron energy determines the interaction time of the quantum state with the environment, the expected result of each theory differs for different electron energies which is a good evidence to show the validity.

In the following chapter, the results of the publication [1] are portrayed. A single-atom tip serves as a highly coherent electron source in a biprism interferometer, in which an interference pattern is recorded. By means of the visibility of the fringes, the coherent properties can be calculated. Since the emitter is assembled as a diode system, the energy and the intensity of the electrons can be set independently. Importantly, it turns out that the coherent properties of the electrons are preserved while they are accelerated by different potentials of two electrodes. Moreover, with a Wien filter and a correlation analysis of the contrast, the energy width of the source is determined.

A sketch of the interferometer is shown in figure 3.1. Many parts were already in use for measuring the decoherence of electrons near a silicon wafer [67]. However, the key elements field emitter, biprism fiber and detection system were improved. All used components of this setup are described subsequently. The idea of a higher count rate for a given electron energy allows to shorten the integration time and additionally improves the sensitivity of a possible sensor application [116].

3.1 Interferometer parts

3.1.1 Single-atom tip

In order to yield higher spatial and temporal coherence properties a beam source with minimal extension and emission angle is favourable. Several different types of electron emitters have been developed in the last decades, e.g. thermal emitter [136], multi-walled carbon nanotube emitter [137] or so-called supertips where a tiny protrusion is created on an etched tungsten tip [138].

However, a lower limit for the source size is naturally given by the finite extension of atoms. Therefore, an electron source where only one atom emits coherently is of great interest. Such a type of emitter was first realized by Fink [139]. Fu developed an easier fabrication method [104] which was further improved by Kuo [70, 140]. It consists of an usual etched single crystal W(111) wire where a monolayer iridium is deposited. In ultra-high vacuum (UHV) the wire is resistively heated to a temperature between 1000 K and 1300 K for 3 or 5 minutes. Due to minimization of the free energy of surface atoms, the tip forms a three-sided atom pyramid with a single atom at the apex spontaneously [104]. This single-atom tip (SAT) can be regenerated in UHV up to 100 times by annealing again [70]. Hereby, the long time stability is preserved. Furthermore, due to its geometry the SAT exhibits a self-focusing effect of the electric field lines which lead to very small emission angles of a few degree [141].

In Fig. 3.2 a sketch of the SAT is shown. The emitting area of a single iridium atom is assumed to be its diameter with $\approx 0.3\,\mathrm{nm}$ [140]. Therefore, the angular coherence constraint (2.9) states a broad coherently illuminated area on the biprism plane.
The emission behaviour and properties of each SAT is characterized in a separate test vacuum chamber. Every annealing and forming step is executed repeatedly and comparably with MatLab software. The properties like electric current through the wire or the processing time is entered manually. During annealing the tip temperature is measured through a window by a disappearing filament pyrometer. With that, a stepwise approximation to the optimal forming temperature is possible. To observe and rate the electron field emission, the emission pattern is recorded by a movable

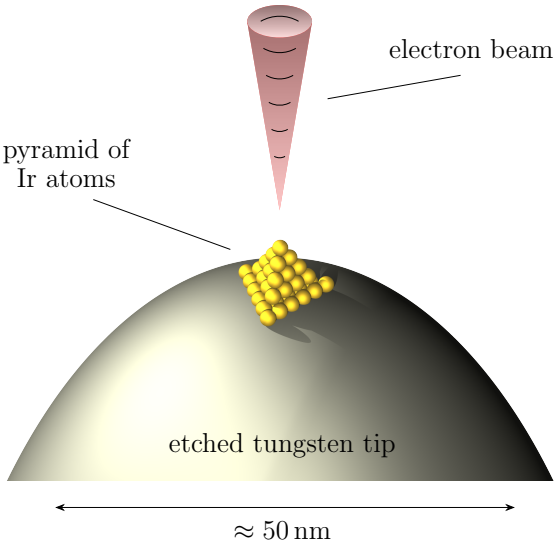

Figure 3.2: Sketch of a single-atom tip serving as a coherent electron source for the biprism interferometer. A three-sided pyramid of iridium atoms is formed on top of the etched tungsten tip. Ideally, the electrons are emitted from only one topmost atom.

MCP detector with a fluorescent screen. Once a sample shows a circular homogeneous pattern and stays stable when further processing, the tip is aligned to the middle of an aperture and then transferred to the biprism interferometer within a laminar flow box. Hereby, great caution is needed not to destroy the tip. It is mounted on a special copper holder where shear forces easily can arise.

3.1.2 Counter electrode

In front of the SAT two electrodes with a hole diameter of 2.5 mm and a distance of 4 mm to each other are positioned. The second electrode is always grounded, whereas the first electrode can be set to a voltage. The applied voltage to the counter electrode influences the field at the SAT, this is why more electrons are emitted when the counter electrode is set to a positive voltage. Respectively less electrons are emitted if a negative voltage is applied. The grounded electrode ensures that the electrons, which leave the source setup are decelerated respectively accelerated to an energy of $e \cdot U_{SAT}$.

3.1.3 Deflector elements

In order to adjust the electron beam on the optical axis which is (ideally) the centre of all interferometer components deflector electrodes are installed along the interferometer bar. This is consistent with the rugged construction principle that prevents mechanical alignment and moving parts during operation [125]. Any beam correction has to be done by electrostatic fields. Therefore, a deflector element consists of four electrodes

with length l_d, each opposing pair with distance d_d being on opposite equal electric potentials. Therefore, nearby electrodes have a different polarity. Thus, the alignment in x- and y- direction is ensured. As for a plate capacitor, the deflection with respect to an angle α follows from

$$\tan\alpha = \frac{1}{2}\frac{l_d}{d_d}\frac{U_{\mathrm{defl}}}{U_e} \tag{3.1}$$

Usually, two deflector elements are combined to one double deflector to allow for a parallel beam shift.

3.1.4 Biprism fiber

The biprism fiber in the interferometer is the crucial element to achieve interference fringes by wave front splitting of the electron waves. The fiber consists of fused silica and is drawn computer-controlled by a fiber-pulling rig [142, 76]. The fibers are produced in Vienna and sent to us within a cooperation with Rauschenbeutel. The experimental setup is depicted in Fig. 3.3. A standard optical fiber is attached on two translation stages and positioned above a hydrogen-oxygen flame with adjustable size and temperature. Thus, the fiber is softened and stretched at the same time with variable force. This technique allows to create tapered optical fibers with pre-defined shape [143]. The fibers in our biprism interferometer exhibit a section of 6 mm with a uniform nominal diameter of 350 nm. SEM images verify that the realized fiber profiles deviate by less than 10 % from the expected design.

In order to install these tapered optical fibers to our interferometer, blank holders made of pure titanium are shipped to Vienna and equipped with the fibers. An ultra-high vacuum compatible two-component epoxy glue is used for the fixing which is cured with ultraviolet radiation. Back in Tübingen (not to crack during the shipment is a good indication of their quality), the holders and the grounded electrodes are magnetron-sputtered with a gold-palladium alloy (80:20). Contact potential effects are hence avoided. Compared to former experiments which used biprism fibers with a gold coating as coherent beam splitter [24], gold-palladium reveals a considerably higher surface smoothness. This is important since irregularities disturb the field distribution and lower the fringe contrast. Characteristic for pure gold is the formation of flakes on the biprism surface. Patch fields arise from the individual grains which slightly modify the work function [144]. Because of that gold-palladium is explicitly favoured.

To ensure constant coverage of all sides, the fiber is coated twice for two opposing sides. A total thickness of ≈ 23 nm is set. The SEM image is shown in Fig. 3.4.

3.1.5 Wien filter

The Wien filter is a useful tool to correct the longitudinal wave packet shift of electron waves caused by varying electric potentials along their trajectory [126]. Mainly the deflector electrodes for beam aligning are responsible for such a shift when the beam does not match perfectly to the optical axis. The Wien filter consists of a crossed magnetic field $\vec{B}$ and electric field $\vec{E}$, both perpendicular to the electron beam path. Contrary to the task of analyzing electron energy spectra, here the Wien filter is operated in

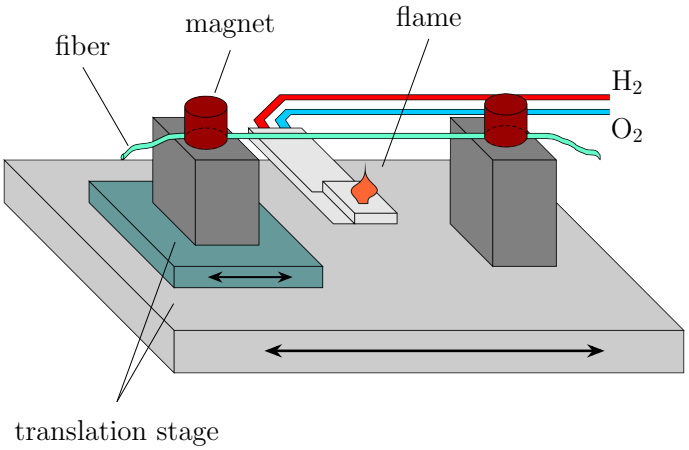

Figure 3.3: Sketch of the fiber-drawing apparatus. A standard optical fiber is moved by two translation stages above a hydrogen-oxygen flame. It becomes softened and stretched along the fiber axis. Magnets keep the fiber tightly attached to the stages. By using computer control, arbitrary shapes with a diameter down to 100 nm can be achieved [145].

Figure 3.4: SEM image of a tapered optical fiber coated with gold-palladium. The smooth surface is clearly visible. The total diameter is 395 nm.

the compensated mode. The magnetic and electric force on the charged particles with velocity $\vec{v}$ cancel each other:

$$e\vec{E} + e\left(\vec{v} \times \vec{B}\right) = 0 \quad . \tag{3.2}$$

Thus, the trajectories of the particles are not affected. However, the induced longitudinal wave package shifts according to electric potentials are of different amplitude when the electron waves pass the Wien filter with lateral separation Δx. This is due to the fact that the wave packets travel on paths of different electric potentials and group velocities inside the Wien filter [126, 146]. With increasing and magnetically compensated capacitor voltage U_{WF}, the fringe pattern stays stationary but the contrast varies due to a shift Δz between the wave packets. Interestingly, since the well-known magnetic AHARONOV-BOHM effect [58, 147] is proven experimentally [148, 60], here we take advantage of the scalar electric AB effect and seem to have an indirect proof [24].

The potential difference in the Wien filter is described by the ratio of the distances [126],

$$\Delta U_{\mathrm{WF}} = 2\, U_{\mathrm{WF}}\, \frac{\Delta x}{D} \quad , \tag{3.3}$$

with the distance D between the capacitor electrodes. For the difference of the group velocities of both beam paths, it is

$$\Delta v = \Delta U_{\mathrm{WF}} \sqrt{\frac{e}{2 m_e \cdot U_e}} \quad .$$

From that, the shift Δz in direction of propagation is calculated by

$$\Delta z = \frac{L}{2D}\frac{\Delta x}{U_e} \cdot U_{\mathrm{WF}} \quad , \tag{3.4}$$

where L denotes the length of the deflector plates. Eq. (3.4) is important for our analysis of the coherence length of a SAT described in the first publication of this work. A simple sketch of the Wien filter and its geometric properties is shown in Fig. 3.5.

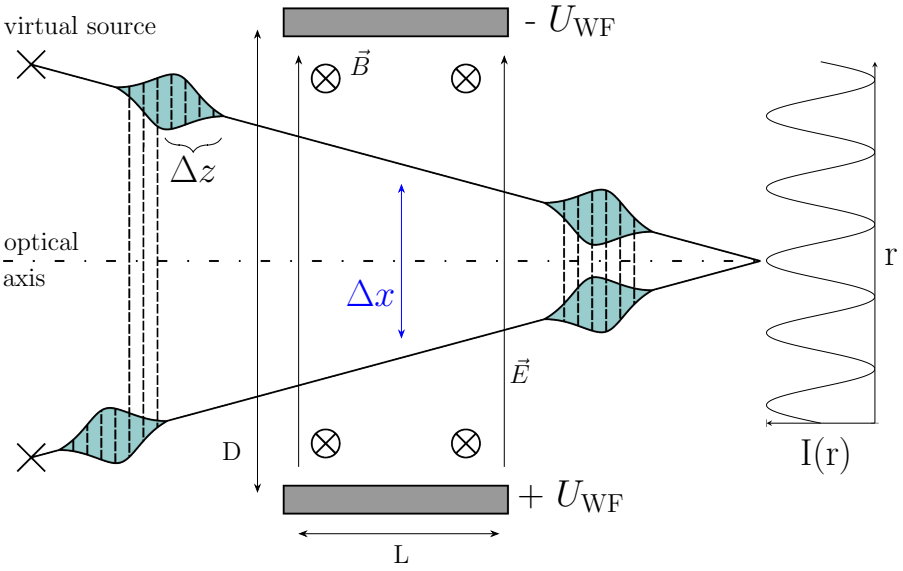

Figure 3.5: A longitudinal shift Δz of two laterally separated wave packets is corrected by the Wien filter in the compensated mode. With that, maximum contrast in the detection plane is achieved.

With this device it is possible to measure the longitudinal coherence length of electron waves directly [149, 1] and furthermore, the corresponding energy width of the source can be derived.

3.1.6 Quadrupole lens

Due to a limited spatial resolution of the detector and an expected fringe periodicity of a few hundred nanometers, a magnification of the interference pattern is required for a reasonable signal acquisition. The inevitable reduction of the detected current density needs to be kept to a minimum. For this purpose, electrostatic quadrupole lenses are well suited since the magnification takes place in mainly one direction perpendicular to the fringes [150]. They consist of four cylindrical electrodes. Diametrical opposed ones are on the same potential U_{Q} but with different polarity compared to their neighbours. The arrangement is illustrated in Fig. 3.6. For reasons of optimal magnification the electrodes have a circular cross section with a radius r_Q 1.147 times bigger than the radius of the in-circle G_0[150]. The electrostatic potential $\hat{V}(x, y, z)$ relative to the

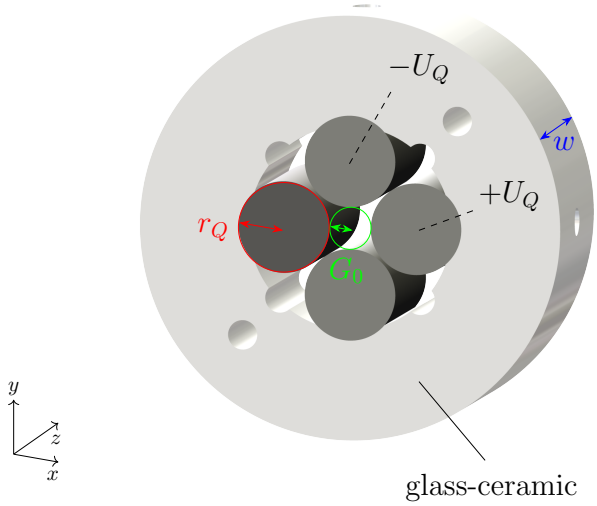

Figure 3.6: Drawing of a quadrupole lens with four circular electrodes with radius r_Q. Diametrical opposing electrodes are on the same potential U_Q, either positive or negative. The electrodes are mounted on a machinable glass-ceramic holder. Here, the xz-plane is defocusing for electrons.

optical axis is given to

$$\hat{V}(x,y) = \frac{x^2 - y^2}{G_0^2} \cdot U_\mathrm{Q} \quad . \tag{3.5}$$

For the calculation of the equations of motion, the electric field strength $\vec{E} = -\nabla\hat{V}$ is expressed in terms of the COULOMB force. Finally, the horizontal plane in Fig. 3.6 acts in a defocusing way, meaning that a negative charged particle is deviated off the axis as follows:

$$\begin{pmatrix} x(z+w) \\ \alpha(z+w) \end{pmatrix} = \begin{pmatrix} \cosh(kw) & \tilde{k}^{-1}\sinh(\tilde{k}w) \\ -\tilde{k}\sinh(kw) & \cosh(\tilde{k}w) \end{pmatrix} \begin{pmatrix} x(z) \\ \alpha(z) \end{pmatrix} \tag{3.6}$$

with $\tilde{k}^2 = (U_\mathrm{Q})/(G_0^2\,U_e)$. The transfer matrix Eq. (3.6) describes the exit point $x(z+w)$ and exit angle $\alpha(z+w)$ along the z-axis dependent on the electrode length w.

3.1.7 Delayline detector

For the detection of the interfering electrons, a wholly innovatively delayline detector is placed at the end of the vacuum chamber. This detector of the company *RoentDek GmbH* bases on an early concept of two meandering wires which provide not only spatial but also temporal information about the incoming particles [79]. This attribute is of great importance for this thesis and the work of our group [1, 2, 4, 113, 6]. It enables a second-order correlation analysis as described in section 2.3. For this work, a similar and further improved assembly is used [80]. In Fig. 3.7 the operation principle of the detector DLD40X is depicted.

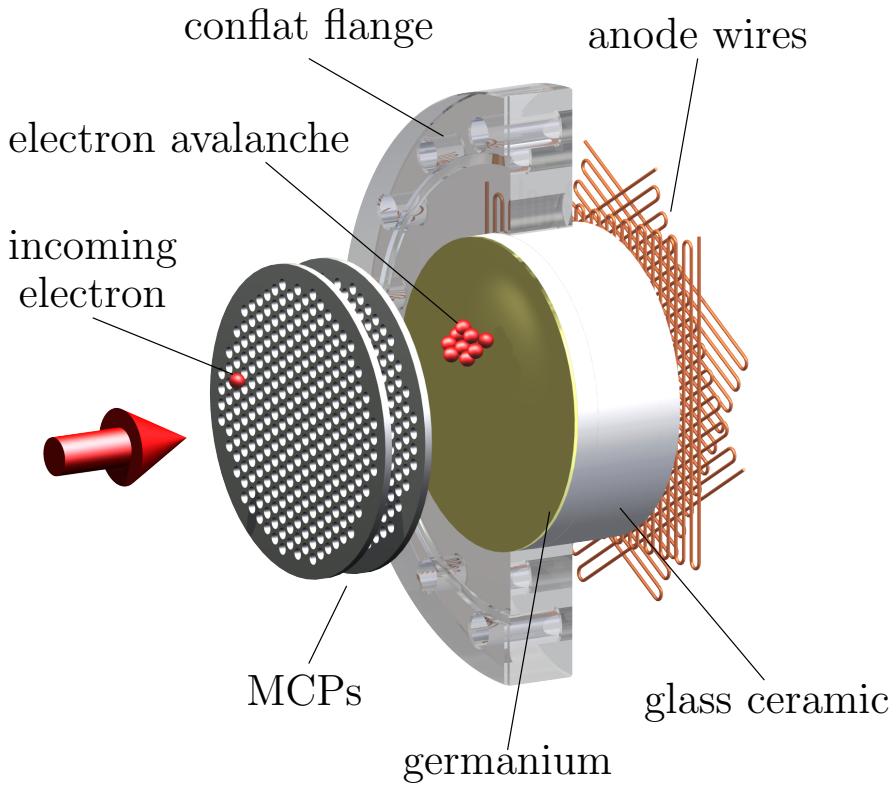

Figure 3.7: Schematic drawing of the delayline detector to gain the spatial and temporal information of particle events in the detection plane. An incoming electron hits the first grounded microchannel plate (MCP) and is amplified together with a second one lying on 2320 V potential. An electron avalanche is released and accelerates towards a ceramic plate which is set to a potential of 2800 V. A highly resistive layer germanium on the plate enables the charges to flow off slowly. The MCP output is then transferred via capacitive coupling to the read-out anode. This hexagonal delayline anode is located on air side and consists of three meandered wire leads arranged in a symmetric geometry at relative angles of 60 °. Signal pulses are picked up in each wire which propagate in both directions of the wire. The differences of arrival times at both ends of the wire allows to calculate the impact position of the electron.

In the following, the main parts and basic properties of the detection system are briefly described and summarized. Thereby, the way of signal processing can be pursued by means of Fig. 3.8. Importance is attached to an appropriate understanding and adjustment of the components for a proper operation of the detector.

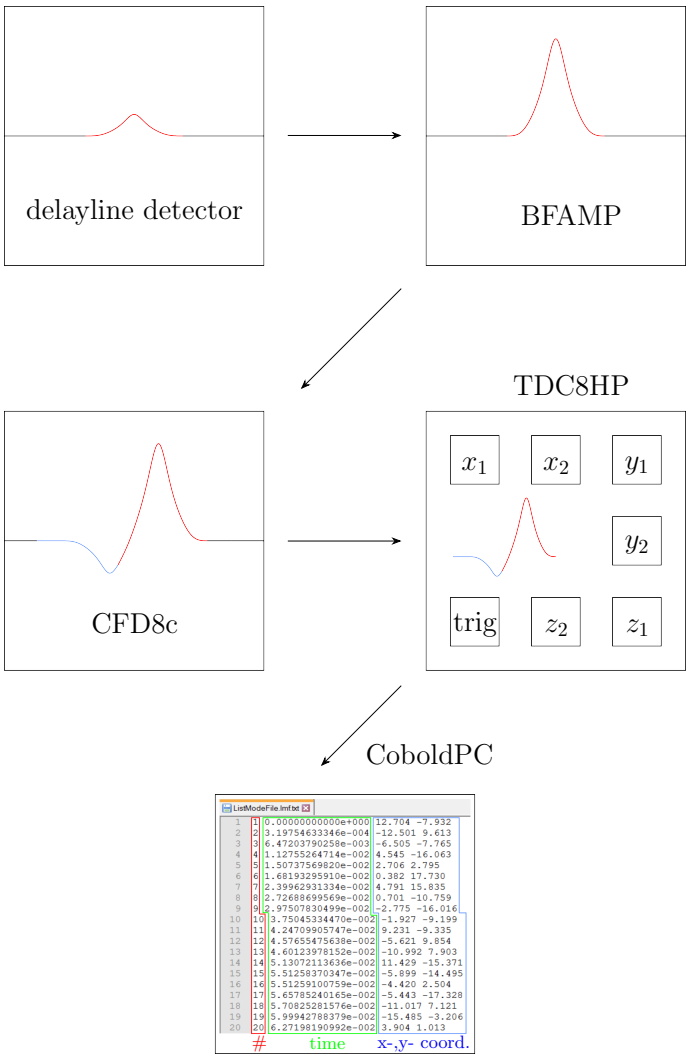

Figure 3.8: Illustration of signal processing of the delayline detector. The detector offers seven output channels, one for each end of the anode wires and one for the MCP signal. A detected count in one channel is enhanced by a bipolar fast amplifier (BFAMP). It is then transformed into a bipolar signal where the zero crossing of the rising edge is used to set the time trigger for the six position channels. Here, the MCP signal is used as the trigger signal. A time-to-digital converter continuously records the digital waveform on its inputs similar to a logic analyser.

- **Microchannel plate and delayline anode:** Two MCPs in chevron configuration with 45 mm active diameter, a thickness of 1 mm and 12 μm pore size [151] are embedded in a standard CF DN 100 flange at one end of the vacuum chamber in order to amplify the incoming signal from the biprism interferometer. The first MCP is grounded and the second one lies on a potential of 2320 V. In total, an electron avalanche with a gain factor of about 10^7 is accelerated towards a ceramic plate biased with 2800 V, see Fig. 3.7. It is 2 mm thick, forming the vacuum-sealed transfer tube for the charge carriers. To enable this charge transfer to air side, a highly resistive layer of germanium is deposited on the vacuum side. Thus, charges accumulate for a short while before they flow off slowly towards a metal rim contact of this "resistive screen". It gives rise to build up an image charge on a metal plate outside the ceramic tube. Thereby, the time constant is in the order of nanoseconds. Onward, the signal is picked up by the hexagonal delayline anode via capacitive coupling. The hexagonal delayline uses three wire layers arranged in strip rows. Each layer is rotated at relative angles of 60 ° compared to the other layers, thus forming a hexagonal symmetry. The strip arrays are embedded in a multi-layer printed circuit board (PCB). The picked up image charge pulse is fed into each delayline, thus creating a signal pulse propagating in both directions along the wire. Hereby, the third wire layer gives extended detection opportunities to improve the multi-hit performance. With the hexanode detector it is possible to control and enhance the intrinsic resolution, yielding in a higher overall imaging performance. This is due to the fact, that the two-dimensional particle position can be computed from any two out of three layers.

  The arrival times $(t_{x_1}, t_{x_2}, t_{y_1}, t_{y_2}, t_{z_1}, t_{z_2})$ are measured. From that, the arrival time differences are determined which directly lead to the charge cloud centroid's position. However, for a proper hit detection the sum of all arrival times need to be constant, $t_{x_1} + t_{x_2} = t_{y_1} + t_{y_2} = t_{z_1} + t_{z_2}$. This means, the spatial resolution of the detector is strongly dependent on the time measurement and the temporal resolution of the further electronics. The pulse at the first MCP serves as the time trigger and initiates a time range in which the particles correlate. Typically, a time resolution of about 100 ps can be achieved corresponding to a spatial resolution of 50 μm [80]. In order to estimate the spatial coordinates of the particle impacts, one can define a signal speed $v_\perp$ perpendicular to the wire orientation which is approximately $\frac{1}{0.75}\,\frac{\text{mm}}{\text{ns}}$ for the used configuration. The position in a hexagonal coordinate frame u, v, w is calculated by

$$u = (t_{x_1} - t_{x_2}) \cdot \frac{v_{\perp_x}}{2} \tag{3.7}$$

$$v = (t_{y_1} - t_{y_2}) \cdot \frac{v_{\perp_y}}{2} \tag{3.8}$$

$$w = (t_{z_1} - t_{z_2}) \cdot \frac{v_{\perp_z}}{2} \quad . \tag{3.9}$$

  The usage of an read-out anode which is placed outside the vacuum is very advantageous concerning the assembly and installation of the mechanical parts. Even more, the PCB is easily detachable and allows to service the anode without

losing the ultra-high vacuum condition in the chamber. Thereby, work time is saved and entering of dust on the interferometer is avoided.

The output of temporal and spatial information with high resolution of electron interference patterns is mandatory for this thesis and makes the application of a second-order correlation analysis to this data possible.

- **Bipolar fast amplifier:** The BFAMPs modules enhance the signals from the anode wires close after detection before they can be routed to timing and digitizing circuits. The default amplification value lies at 150 with a bandwidth of up to 200 MHz. Output pulses with maximal $\pm 1.5\,\mathrm{V}$ are produced linearly [152]. The BFAMP creates a bipolar output signal for further digital read-out processing, see Fig. 3.9. Compared to former detector versions, the bipolar signal offers as a key benefit higher time performances by triggering all signals by the zero-crossing. It can be shown that this zero-crossing time is independent from the incoming pulse heights, thus making it more accurate for time calibration. In order to create bipolar signals, the input signal is pre-amplified and split up into signals with different polarity. Afterwards, a certain time delay between those two components is generated with an external cable on the rear panel. These two signals are again summed up and amplified. All amplifying channels and their inverted equivalent can be monitored separately to optimize the potentiometer settings. The delay time is important for the following CFD and is ideally on the order of the input signal's FWHM. For determining the characteristic signal rise time and to exclude disturbing effects of the amplifier bandwidth, the output is observed without connected delay cable. Thus, the unipolar output signal serves as reference. Moreover, in order to minimise noise pickup, all amplifier housings are metallic and grounded properly by a thick copper cable. Furthermore, electric crosstalk is avoided since the input signal cables are free-standing placed.

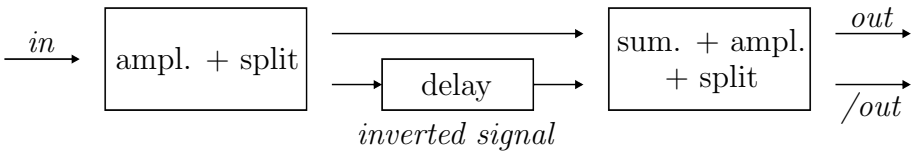

Figure 3.9: Sketch of forming a bipolar signal shape by a BFAMP circuit. Explanations are given in the text.

- **Constant friction discriminator:** The CFD unit is used for improved processing of timing signals obtained from the BFAMP. In combination, a high timing precision and pulse-pair resolution is achieved. Therefore, all parameters have to be adjusted precisely with respect to different input signal properties. In general, leading-edge discriminator units produce digital output signals with a time jitter if the input signals have different amplitudes. The CFD is constructed with the goal to deliver output signals with timing properties being independent from the initial pulse heights as long as a selectable threshold level is exceeded and the input signals do not vary as function of the incoming pulse heights (e.g. due to non-linear effects) [153].

The CFD is driven with +12 V DC and offers eight independent channels. For optimal operation, the CFD requires proper adjustment of the parameters by means of potentiometers:

→ Threshold level: An electronic circuit chain consisting of two comparators and a logical AND-gate switch to "high" if the input signal exceeds the threshold level. Ideally, this level is set right above the noise level but low enough to count small input signals.

→ Walk level: It is specified similarly for the bipolar signal and should be set near above the noise level of the input signal. As the noise fluctuates, several transitions from "low" to "high" are generated. This zero-crossing serves as the timing output of the circuit.

→ Delay: It is achieved like for the BFAMPs with external cables. Approximately, a 1 m long cable gives a delay of 5 ns (Lemo 00 series). The CFD delay has to be balanced with the input signal rise time t_R and the fraction F. Loosely speaking, a proper delay D is realized when

$$D = t_R \cdot (1 - F) \quad . \tag{3.10}$$

If the delay is too high, the two signal parts do not merge to a bipolar signal. If the delay is too short, no distinct zero-crossing can be observed.

→ Fraction: It defines the ratio of the peak heights of the bipolar signal. Usually, the value is set to ≈ 0.3. However, according to Eq. (3.10), it is linked to the delay and should produce a distinct bipolar signal with high slope at the zero-crossing.

Threshold and walk level can be monitored on separate output sockets.

- **Time-to-digital converter:** The TDC is a PCI slot card with several connection sockets compatible with Lemo 00/250 connectors. It offers many features in analysing the data from the CFD such as ultra-short dead times between multiple hits on one channel (below 5 ns), simultaneous read-out and acquisition, unlimited number of hits per trigger and a high maximum read-out rate of several hundred kHz. The TDC continuously forms and records digital waveforms according to its inputs. It acts as a logic analyser to identify rising input signal transitions for each channel individually. One transition characterizes a hit. The accuracy is up to 25 ns serving as the time unit for all channels [154].
  In order to relate the signals in time, an arbitrary channel serves as a trigger input. For our purpose, the MCP channel is used. A released trigger condition is applied to group the anode wire signals x_i, y_i, z_i with $i \in \{1, 2\}$. Groups of hits are merged within a certain time interval after a trigger. Its range is limited to 419.4 μs. If a trigger is released inside the range of a group, the following is possible:

  1. The new trigger is suppressed and is counted as a usual hit.
  2. The new trigger sets a new group and ends the previous one.
  3. The new trigger sets a new group and overlapping data is assigned to both groups whereas the timing value refers to the corresponding trigger.

A trigger dead time can be set to apply the first case and to avoid overlapping groups. In this work, this value is chosen to be 40 ns. The TDC as well as the CoboldPC software are configured and calibrated by typical text based configuration files where all relevant parameters are written in independent lines. It allows an easy software adjustment of the detection properties.

- **CoboldPC software package:** CoboldPC (acronym for "Computer based online- offline listmode dataanalyser") is a complete data acquisition and analysis program in which the detector hardware can be addressed and controlled. All information is stored event by event in a data list with four columns showing a continuous numbering according to the impact times, the time value and the two coordinates in x- and y- direction. The number of recorded events can be entered manually. This list can be run and processed either during the data read-out (online mode) or after the data acquisition (offline mode) is finished. In Fig. 3.10 an image of the electrons impinged on the detector is shown in the main window of the graphical interface. There are several options to customise this image to the experimental conditions, e.g. the pixel binning can be changed or the image is cleared and updated every second. It is especially helpful when varying sensitive beam settings. Furthermore, count rates and raw data in different channels can be displayed with the program. The command line in CoboldPC is used to start

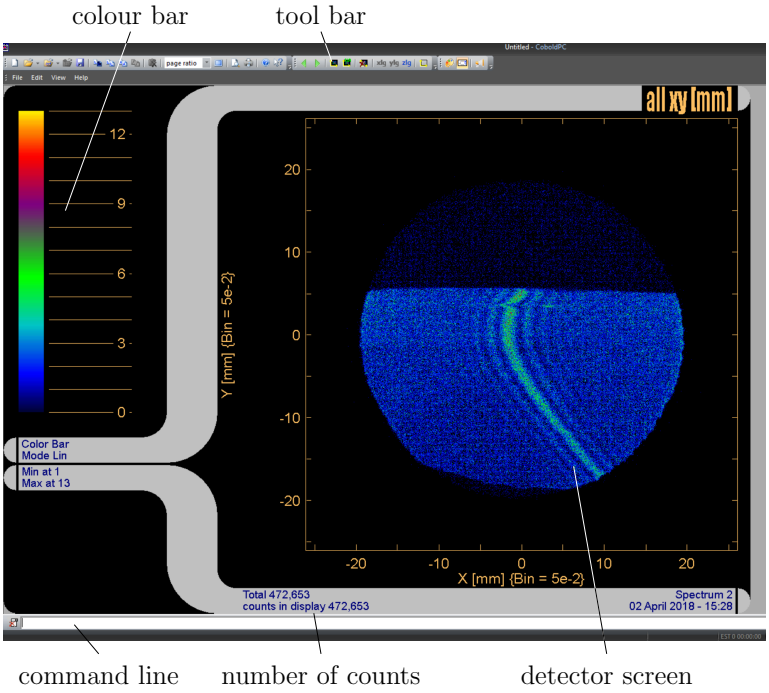

Figure 3.10: Typical view of the CoboldPC interface. Exemplarily, a random interference pattern with 1.6 keV electrons is shown during experimental optimization of the beam trajectory. Distances on the screen can be extracted from the two axes. The upper dark region of the circular detector area is the shadow of the gold plate. Also, dust contamination is observable at the upper end of the fringes.

the main constituents of a read-out session. This includes primarily the launch of a user customised script file where all data transfer routines between hardware and software are defined. From there, the yielded variables are stored in a list of coordinates which can be displayed in different spectra in the program. These 2d histograms are widely versatile for checking specific parameters on their functionality. Parameters which can be varied in the analysis routine are for example length scale calibration factors or the conditions for a true event. To ensure that only real particle impacts are shown in the spectrum, a constant value of the time sum $x_1 + x_2$, $y_1 + y_2$ and $z_1 + z_2$ for all three wire layers is demanded within a selectable range. This prevents the detection of noise.

3.2 Evaluation

The characteristics of the described setup, in order to enhance the intensity of the electron beam, are determined. Also, the limits of the design are tested. An interference pattern with only 600 V emission voltage is recorded. This is possible due to the coherent intensity enhancement and opens up new possibilities in low-energy electron interferometry.

3.2.1 Characterization

As a first step, the performance of a higher electron emission rate is examined. Thereby, two situations are compared. In the first case, the standard operating mode is run where the counter electrode is grounded and the tip voltage is increased from 1560 V to 1800 V. According to the Fowler-Nordheim theory, the intensity increases. In the second case, the tip voltage remains constant at $U_{\mathrm{SAT}} = -1600\,\mathrm{V}$ whereas the voltage of the counter electrode is varied from $-119.7\,\mathrm{V}$ to $+199.7\,\mathrm{V}$. All other relevant parameters, in particular the biprism voltage $U_f = 0.331\,\mathrm{V}$, are kept constant. The second electrode is grounded in all measurements.

Figures 3.11 (a) to (c) show the results of the standard operating mode. The count rate increases with higher tip voltages like expected from the Fowler-Nordheim theory. The inset of Fig. 3.11 (a) illustrates a Fowler-Nordheim plot. The measured fringe distance is also shown. According to Eq. (2.13) an increasing acceleration voltage causes an increasing fringe pattern periodicity s. However, is has to be noted that the fringe distance in Fig. 3.11 is also affected by the the quadrupole lens magnification that depends on the velocity of the electrons [150] which is the reason for a reduced fringe distance. The contrast, extracted by the correlation analysis, is shown in Fig. 3.11 (c) and remains almost constant.

For the case of varying the potential of the counter electrode, the evaluation of the count rate, the fringe distance and the contrast is shown in Fig. 3.11 (d) to (f). The horizontal axis is arranged in the way that a voltage of 0 V of the counter electrode corresponds to the tip voltage of $-1600\,\mathrm{V}$ in Fig. 3.11 (a) to (c). For these measurements this voltage leads to a wavelength of $\lambda_{\mathrm{dB}} = 30.7\,\mathrm{pm}$. In Fig. 3.11 (d) the achieved count rate is plotted against the counter electrode voltage. The signal on the detector increases by a factor of ~ 6.4 which is a clear evidence of the effectiveness of the method. A linear behaviour in a Fowler-Nordheim representation is observed

if the potential difference between tip and counter electrode is regarded as extraction voltage. The constant fringe distance in Fig. 3.11 (e) together with the simulations in section 3.2.3 suggest the conclusion that the counter electrode voltage does not affect the electron wavelength at the position of the biprism fiber. Additionally, the achieved contrast of an applied correlation analysis is depicted in Fig. 3.11 (f). Since no significant change is observable, the transversal and longitudinal coherence properties can be considered as constant. To support this finding and to provide a higher confidence, further tests were performed.

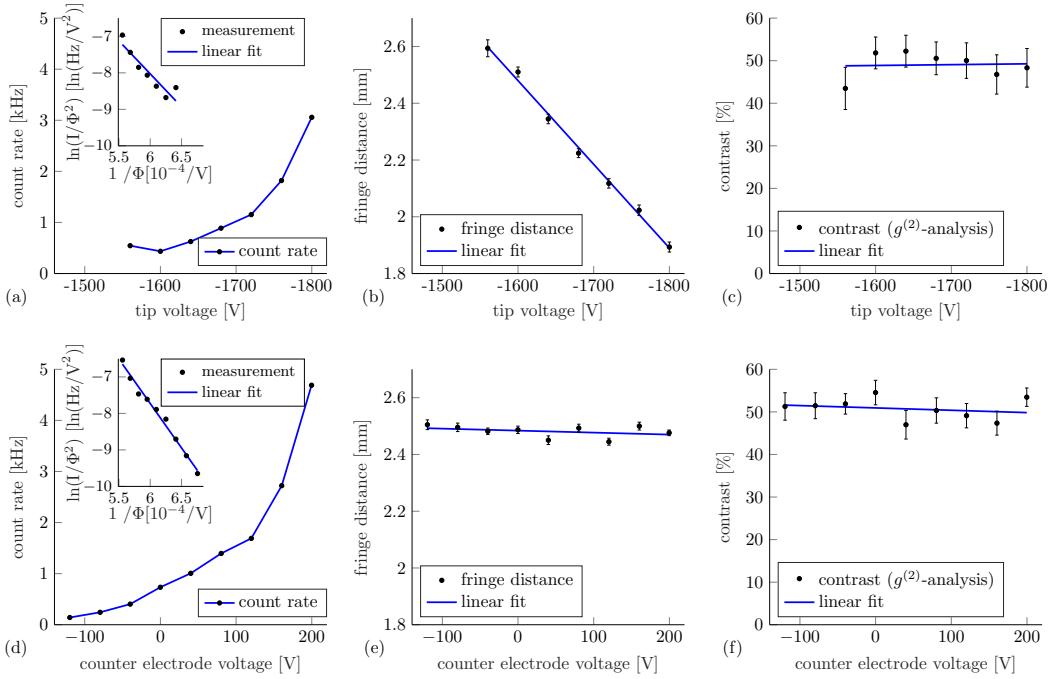

Figure 3.11: Comparison of two cases regarding the count rate, fringe distance and contrast. The subfigures (a) to (c) reveal the behaviour for a varying tip voltage U_{SAT} with grounded counter electrode. In (d) to (f), a voltage to the counter electrode is applied. Φ in the inset of subfigure (a) equals the tip voltage. (c) The determined contrast based on a correlation analysis remains constant [4]. (d) Here, the count rate is determined as a function of the aperture voltage. U_{SAT} is $-1600\,\mathrm{V}$. The signal on the detector increases by a factor of ~ 6.4. Inset: Again a FOWLER-NORDHEIM plot, where Φ equals the potential difference between the tip and the counter electrode. (e) The fringe distance does not change for different aperture voltages. Thus, the electron energy is only dependent on the tip voltage. (f) The visibility remains constant. Hence, the coherent properties of the electron beam are not affected by a counter electrode voltage [1]. Figure from [1]. Reprints with permission of the American Physical Society (AIP).

3.2.1.1 Coherence

In order to verify that the transversal coherence does not change by an applied counter electrode voltage, a separate test is performed where the number of visible fringes is determined at the maximal and minimal voltage of the counter electrode. The interferograms for $U_c = -119.7\,\mathrm{V}$ and $U_c = 199.7\,\mathrm{V}$ are illustrated in Fig. 3.12. Both, the detected (Fig. 3.12a) and the reconstructed (Fig. 3.12b) interferogram is shown, using the correlation analysis and algorithm described in [4, 113, 116]. In deviation from the publications, the used model function for the analysis is

$$I(x) = I_0 \cdot \left(1 + K_m \cdot \cos\left(\frac{2\pi x}{s_m} + \Phi_0\right)\right) \cdot \mathrm{sinc}^2\left(\frac{2\pi x}{s_1} + \Phi_1\right) \quad . \tag{3.11}$$

according to Eq. (2.7). K_m and s_m are determined. The average intensity I_0, the phases Φ_0 and Φ_1 and the width of the interference pattern s_1 are additional fitting parameters. The contribution of a double-slit analysis is covered within the squared *sinc*-function [155].

Each fringe in Fig. 3.12a and Fig. 3.12b is marked by a number. Obviously, the amount of visible fringes does not change within the measurements. Accompanied by the fact that the visibility remains constant, this clearly indicates an unchanged transversal coherence length.

Furthermore, it is tested if the longitudinal coherence is affected by the counter electrode voltage. The longitudinal coherence length can be measured by using a Wien filter which satisfies the Wien condition, Eq. (3.2). A series of measurement for counter electrode voltages of 0 V, 100.2 V and 199.7 V is performed, see Fig. 3.13. The initial Wien filter voltage of 72 V is stepwise decreased to −99 V. For each measuring point the current through the Wien filter coils is adapted to ensure the Wien condition at any time. Indisputably, a small error is hereby made since the current drifts slightly while the coils thermalize. At least 10^5 particles are recorded in an interferogram for a more precise correlation analysis. Although the biprism voltage $U_f = 0.331\,\mathrm{V}$ and the acceleration voltage $U_{\mathrm{SAT}} = -1600\,\mathrm{V}$ remain constant, minimal shifts are observed by changing the counter electrode voltage. Every recorded data file is analyzed with a model function and a correlation analysis as mentioned before. In Fig. 3.13 the visibility is plotted against the Wien filter capacitor voltage. The associated count rates of 0 V, 100.2 V and 199.7 V counter electrode voltage are $523 \pm 43\,\mathrm{Hz}$, $1851 \pm 147\,\mathrm{Hz}$ and $5620 \pm 528\,\mathrm{Hz}$, respectively. Thus, the integration times vary significantly. As a result of a strong impact of dephasing mechanisms there is no contrast determinable for Wien filter capacitor voltages higher than $\sim 30\,\mathrm{V}$ with the spatial signal at $U_c = 0\,\mathrm{V}$. The longitudinal coherence length is determinable in this case only by applying the correlation analysis where not only the spatial information is included but also the temporal to correct the dephasing.

Three Gauss fits of the form

$$K\big(U_{WF}\big) = K_{\max} \cdot \exp\left(\frac{1}{2}\left(\frac{U_{WF} - U_{\mathrm{shift}}}{\sigma}\right)^2\right) \quad , \tag{3.12}$$

are applied to the data of Fig. 3.13 in order to yield the maximal contrast $K_{\max}$ and a fitting parameter U_{shift}. According to [126] the longitudinal coherence length l_c repre-

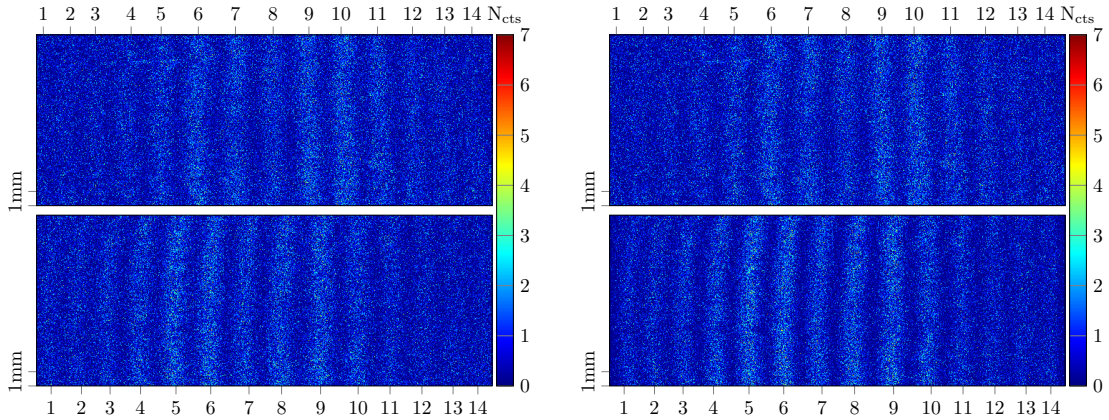

(a) Detected interferograms **(b)** Reconstructed interferograms

Figure 3.12: Both interferograms exhibit the same number of interference fringes, revealing that the transversal coherence of the electrons is not affected by the counter electrode voltage. In the left bottom corner, a length scale is given. The colour bar represents the number of hits per pixel.
(a) Two detected interferograms at $U_c = -119.7\,\mathrm{V}$ (top picture) and $U_c = 199.7\,\mathrm{V}$ (bottom picture), both at a fixed tip voltage of $U_{\mathrm{SAT}} = -1600\,\mathrm{V}$. The contrast is determined to $K_m = 30.6 \pm 2.1\,\%$ and $K_m = 33.9 \pm 2.2\,\%$, respectively. The fringe distance is $s_m = 2.52 \pm 0.01\,\mathrm{mm}$ and $s_m = 2.49 \pm 0.01\,\mathrm{mm}$.
(b) Derived reconstructed interferograms at $U_c = -119.7\,\mathrm{V}$ (top picture) and $U_c = 199.7\,\mathrm{V}$ (bottom picture), both at a fixed tip voltage of $U_{\mathrm{SAT}} = -1600\,\mathrm{V}$. The reconstruction offers a contrast of $51.3 \pm 3.2\,\%$ and $53.5 \pm 2.2\,\%$ with a corresponding pattern periodicity of $2.52 \pm 0.01\,\mathrm{mm}$ and $2.50 \pm 0.01\,\mathrm{mm}$. All measurements are recorded with $3 \cdot 10^5$ particles. The reconstructed contrast is more accurate and yields higher values for smaller integration times (64 s bottom picture compared to 2122 s top picture). This is due to the fact that a perturbation has to be phase stable during the measurement to be perfectly corrected [1]. Figure from [1]. Reprints with permission of the American Physical Society (AIP).

sents a specific shift of the separated wave packets where the contrast vanishes. Defining this value to 10 % of the peak value, the necessary voltage U_{cl} for this shift is

$$U_{cl} = \sqrt{2 \cdot \ln 10} \cdot \sigma \tag{3.13}$$

with the width σ of the GAUSS fit. Inserting U_{cl} into equation (3.4), the longitudinal coherence length l_c can be calculated. The separation of the partial beams Δx at the center of the Wien filter is derived from geometric considerations

$$\Delta x = \Theta \cdot d_{\text{WF-QP}} \quad , \tag{3.14}$$

with $d_{\text{WF-QP}}$ being the distance between the Wien filter and the quadrupole lens. Θ corresponds to the superposition angle determined by Eq. (2.11).

For a constant separation of the partial beams of 135 nm at the center of the Wien filter, the resulting data reveal coherence lengths of 82 ± 9 nm for 0 V counter electrode voltage, 93 ± 10 nm for 100.2 V and 82 ± 8 nm for 199.7 V. Within the margin of error, the longitudinal coherence length remains constant while enhancing the emitted intensity of a cold field emitter by a biased counter electrode. Additionally, the energy width of the single-atom tip can be determined according to Eq. (2.8). The evaluation leads to energy widths of 377 ± 40 meV, 334 ± 37 meV and 377 ± 35 meV, respectively. These results are in good agreement with the literature value for the energy spread of SAT field emitters of 0.4 eV [156].

3.2.2 Low voltage emission

Slow coherent electrons are of great interest in several fields of research [108, 109, 157]. The presented method allows to generate a coherent electron beam with energies well below an usual field emission process. Thanks to the additional potential of the counter electrode, an electron energy of only 600 V is achieved in the current setup. This is significantly lower than the minimal operating voltage of the implemented single-atom tip where no emission can be observed without a counter electrode. The required voltage for initiating the emission is namely dependent on the geometry and shape of the tip surface. By applying a counter electrode voltage of 1378 V, it is possible to generate an interference pattern as shown in Fig. 3.14. Thereby, the count rate is still reasonable with 1138 ± 2 Hz. The corresponding DE BROGLIE wavelength is enlarged for lower energies to 50 pm according to Eq. (2.2). However, the interference contrast is clearly lowered as slow electrons are more susceptible to dephasing and correlation correction is limited to timescales with phase stable perturbations. Only 19.8 ± 1 % is yielded with a pattern periodicity of 8.6 ± 0.1 mm. The correlation analysis offers a contrast of 37.7 ± 3.0 % with a fringe distance of 9.0 ± 0.3 mm. In Fig. 3.15 the $g^{(2)}$-correlation function is plotted. Calculating a theoretical fringe distance of 928 nm before entering the quadrupole lens, the magnification factor of the interference pattern states to 9730 ± 290.

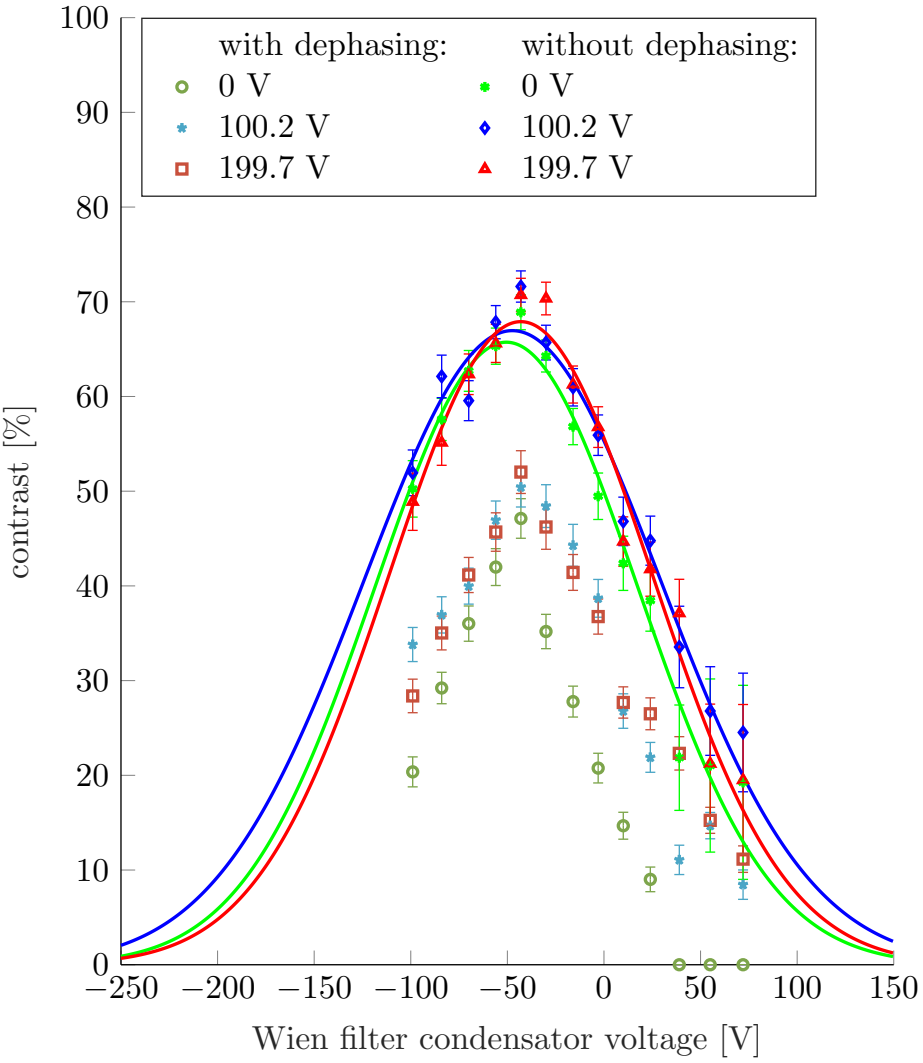

Figure 3.13: Measurement of the interference contrast as a function of different Wien filter capacitor voltages. The tip potential $U_{\mathrm{SAT}} = -1600\,\mathrm{V}$ is fix. Three aperture voltages 0 V, 100.2 V and 199.7 V are applied. The uncorrected contrast is shown in green circles, blue stars and red squares. As strong dephasing mechanisms by the network frequency are present, three data points contrasts are not evaluable. For that reason a $g^{(2)}$-correlation analysis is applied, providing the corrected contrast distribution (green stars, blue diamonds and red triangles). Gauss fits to the data reveal that the longitudinal coherence lengths show no significant variations for different aperture voltages [1]. Figure from [1]. Reprints with permission of the American Physical Society (AIP).

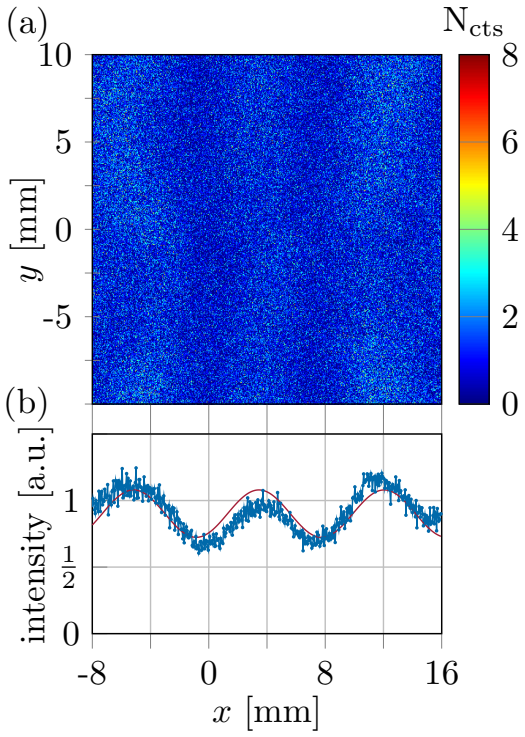

Figure 3.14: (a) Interferogram of electrons with 600 eV energy while applying 1378 V to the counter electrode. The pattern is straightened by a fourth degree polynomial for a proper evaluation. The biprism voltage is 0.135 V. (b) Blue graph: average intensity along the y-direction of (a). Red curve: The numerical fit yields a contrast of $19.8 \pm 1\,\%$ and a pattern periodicity of 8.6 ± 0.1 mm.

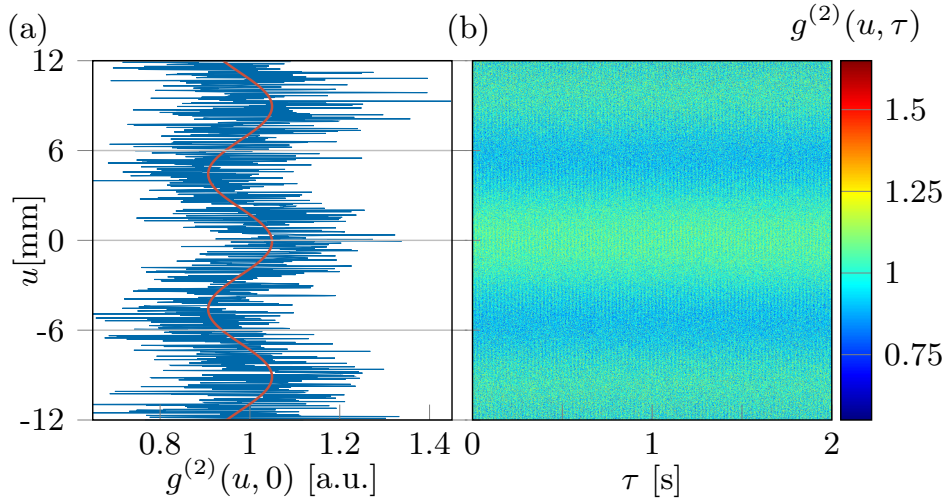

Figure 3.15: (a) Blue graph: the second-order correlation function $g^{(2)}(u, 0)$ at the correlation time $\tau = 0$. Red curve: fit function to calculate the unperturbed contrast of $37.7 \pm 3\,\%$. (b) The second-order correlation function $g^{(2)}(u, \tau)$ extracted from the data in Fig. 3.14 (a).

3.2.3 Simulation

In order to support the finding that the coherent properties of the electrons are preserved while a counter electrode is biased, simulations with the software package *Comsol* are performed. A detailed description of the electrical field distribution is given for the two experimental cases described before: first, the tip has a potential of $U_{\mathrm{SAT}} = -1600\,\mathrm{V}$ and the counter electrode $U_c = 200\,\mathrm{V}$. Second, the tip is set to only $U_{\mathrm{SAT}} = -600\,\mathrm{V}$ and the counter electrode to $U_c = 1378\,\mathrm{V}$. A further aperture is grounded at any time to ensure a homogeneous field pattern. Moreover, the energy of the electrons when exiting the assembly and the corresponding trajectories are analyzed.

In Fig. 3.16 (a) and (c) a schematic drawing of the assembly is shown. Since it has cylindrical symmetry in z-direction, a cross section of the x-y-plane is sufficient for the simulation. In two dimensions, the calculations are less extensive and time-consuming. As can be seen in the figure, a $125\,\mu$m thick tungsten wire is drawn along the x-axis at $y = 0$. An inlet area can be defined where all particles are released into the geometry with a certain direction and energy. Here, electrons with zero starting energy accelerate in x-direction. Due to computational reasons the tip radius in this simulation is chosen to be $2\,\mu$m even though the real experimental tip extension is in the nanometer range. Unfortunately, *Comsol* is not able to handle geometries which vary in size by several orders of magnitude. However, field lines far away from the tip are not affected from this fact and cause the same trajectory for the electrons. The validity of the results is justified since the microscopic field emission process is not simulated and of no concern.

For the first case, the electric field is examined in Fig. 3.16 (a). Electrons in the emission cone become accelerated and decelerated, depending on the position in the field distribution. Those electrons which pass the two apertures with 2.5 mm diameter approach a certain energy. As indicated in Fig. 3.16 (b) this limit turns out to be 1600 eV given by the tip potential. In Fig. 3.16 (c) the second case is simulated with an analogues result. Indeed, a higher counter electrode voltage leads to a bigger fraction of deflected electrons which do not pass the apertures, but again the energy of the exiting electrons approach to the energy provided from the tip potential (Fig. 3.16 (d)). This result is valid for any potential of the tip or the counter electrode. Thus, only the tip voltage and not the counter electrode voltage determines the fringe distance of an interference pattern when enhancing the electron signal [1]. Furthermore, the simulations indicate that the increase of signal is not due to a lensing effect of the electron beam. It is most likely because the field strength at the tip surface is increased which causes a higher field emission current according to Fowler-Nordheim theory.

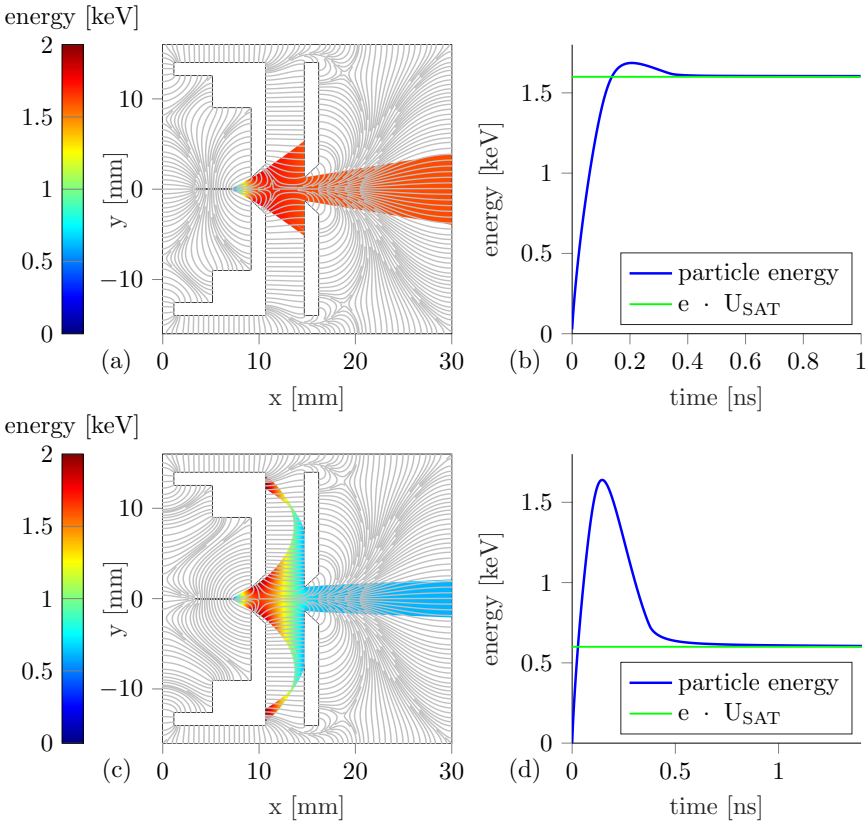

Figure 3.16: (a) Electrical field distribution in a cross section of the cathode box geometry including the tungsten tip and the two apertures. The tip at $y = 0$ is set on $U_{\mathrm{SAT}} = -1600\,\mathrm{V}$. Electrons with zero starting energy accelerate in the field between tip and counter electrode which is set on $U_c = 200\,\mathrm{V}$. The second aperture is grounded. The colour bar represents the energy of the electrons. Electric field lines are shown in pale grey schematically. (b) Average energy of the electrons as they travel along the optical axis. The approached energy 1600 eV is given by the tip potential. (c) Analogue simulation with $U_{\mathrm{SAT}} = -600\,\mathrm{V}$ and $U_c = 1378\,\mathrm{V}$. A fraction of electrons bend back onto the surface of the counter electrode. However, those electrons which pass the second electrode end up again with the energy provided from the tip (d). The acceleration processes between the different components is more distinct than in (b) leading to an electron energy of 600 eV [1]. Figure from [1]. Reprints with permission of the American Physical Society (AIP).

4 The compact biprism interferometer

Interferometric measurements in general are widely sensitive to external perturbations as small deviations of the separated waves lead to a phase shift. In the case of electron interferometry, not only mechanical vibrations, temperature drifts or rotations but also electromagnetic fields can disturb the coherent phase relation between two wave packets. This time dependent dephasing causes a reduced contrast of the interference pattern. In the context of decoherence effects described in chapter 5 long-time measurements are notably susceptible to the latter. Also, measurements of the electric AB-effect or ion interferometry are faced with this challenge [5, 56].

As already mentioned, the delay line detector with its ability to record not only spatial but also temporal information of incoming particles is a very helpful tool in the field of particle interferometry. Based on previous measurements a thematically similar experiment with regard to sensor technology is executed successfully also. Decoherence measurements have the potential to become a promising method to examine material surfaces non-invasive and thus, are relevant for sensor systems. Therefore, it is tested if a small and portable electron interferometer can be built where not only interference fringes with high contrast are produced but also dephasing mechanism are corrected and utilized for sensor applications. Combined with existing electron microscopes, surface analysis would for example highly benefit from it.
In terms of the latter the functional capability of the detector is demonstrated and extended with another electron interferometer which is integrated into the same vacuum chamber. All electronic power supplies, shielding properties and vacuum conditions remain unchanged.
This electron interferometer is very compact built with a length of only 87 mm. Still, there is an additional drift distance of 170 mm between the exit of the interferometer and the first MCP of the detector.
The design aims for the interferometer were to minimize the dimensions to construct a portable electron interferometer for sensor analysis. In contrast to the well established construction principle with two parallel ceramic rods [125], here all elements are mounted tightly in a copper shell with an outer diameter of 36 mm. The advantage is obvious: the system is extremely rigid against mechanical vibrations and the assembly is simple. Thus, all parts are already aligned. Moreover, in combination with the developed procedure of spectrum analysis by correlation theory the compact interferometer is well suited as a portable sensor for electromagnetic and vibrational frequencies [4, 112, 113]. A schematic sketch of the interferometer is given in Fig. 4.1. All parts work principally similar to the interferometer parts described in chapter 3.
A standard etched cold field emission tip creates an intense electron beam which can be aligned by a pair of deflector electrodes. The coated biprism fiber performs a wave front splitting when a positive potential compared to ground is applied.

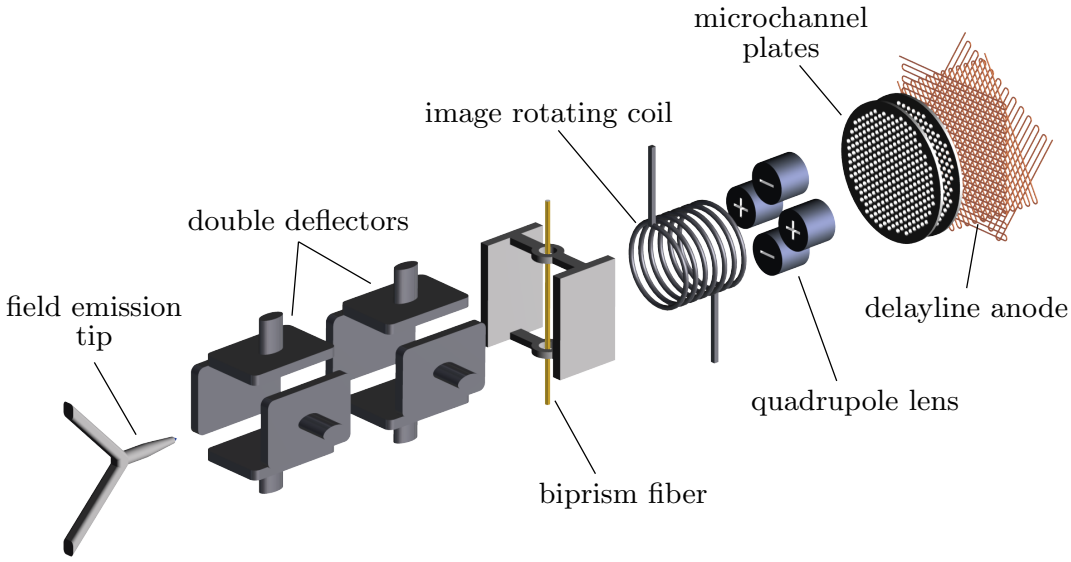

Figure 4.1: Schematic sketch of the compact interferometer [2]. A polycrystalline tungsten tip emits electron matter waves which are split by the biprism fiber. The formed interference pattern is recorded with a delayline detector.

A small misalignment can be corrected by an image rotating coil if the biprism fiber does not match with the magnifying axis of the quadrupole lens. The interference pattern periodicity is magnified to fit the spatial resolution of the detector. As already mentioned, a hexagonal delay line detector is used with a spatial and temporal resolution of $\approx 100\,\mu$m and ≈ 0.1 ns, see section 3.1.7.

A real photograph of the setup is shown in Fig. 4.2 (a) and (b). The following distances are important:

- between tip and biprism fiber: 17.2 mm.
- between fiber and the interference plane at the entrance of the quadrupole lens: 26.8 mm.
- between fiber and the grounded electrodes: 2 mm. The fiber radius is 200 nm.

The complete system is then placed in a mu-metal tube in a vacuum chamber at a pressure of $5 \cdot 10^{-10}$ mbar to ensure a long lifetime and stable emission of the tip [106].

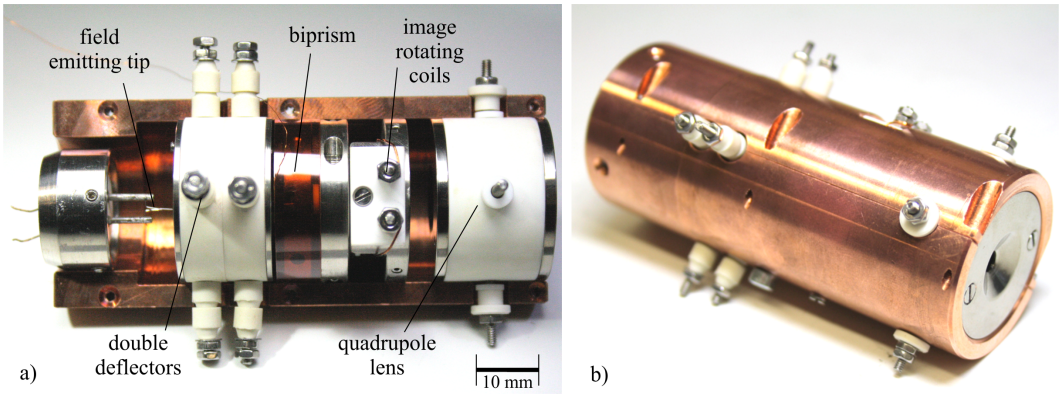

Figure 4.2: (a) Photograph of the components of the compact interferometer. The upper copper shell is removed. (b) Completely mounted interferometer with both copper half shells [2]. The protruding screws allow an electrical connection. Figure from [2]. Reprints with permission of the American Physical Society (AIP).

4.1 Fabrication of an etched tungsten tip

For the implementation of a self etched polycrystalline tungsten tip as a field emitter in the compact biprism interferometer, several process steps have to be carried out. First, tungsten is the material of choice for the field emitting tip. It has many beneficial properties described well in literature [158, 159, 101]. It offers a high mechanical robustness, the highest melting point of all metals, good thermal and electrical conductivity and a low vapour pressure. The used initial configuration of tungsten is a 125 μm thick polycrystalline wire. In general, the work function of tungsten is very low and the remolding process, changing the geometry and emission characteristics purposefully, works best [160, 161].

Actually, the emitter is built up of three parts: a so-called Siemens holder, a ceramic item with two metallic bars, a bended wire holder and a small piece of tungsten wire which is etched to a sharp tip. The short wire piece is spot welded on the wire holder which itself is spot welded on the Siemens holder.

4.1.1 Spot welding

First of all, a standard tungsten wire with 125 microns diameter and approximately 3 cm length gets folded in the middle and becomes a V-shape. Both ends then get spot welded to the metallic bars of the Siemens holder with a spot welding device manually. For a short time a high current flows through a tiny spot, ensuring a melted connection by pressing both parts together. Important parameters are the spring tension 1 N, a voltage of 1.5 V and a current of 8.8 A. Working with a spot welder requires a lot of fine tuning since the wire or the welding spot can break at any time.
The tungsten wire is quite soft. Therefore, the electrodes of the spot welding apparatus need a roughening by sandpaper before every usage to avoid adhesion. Then the wire is spot welded to the v-shaped wire holder very carefully. One has to take care that the short piece of single crystalline tungsten is aligned precisely in the middle and in forward-direction. Also the short wire must not deform by pressing it onto the wire holder.

4.1.2 Etching method

The etching process used in this thesis to manufacture very sharp tungsten tips bases on the method described in [105]. The setup is depicted in Fig. 4.3. The standard procedure for the fabrication of tungsten tips is electrochemical wet etching by dipping a tungsten wire into a potassium hydroxide solution (KOH). A micrometer screw allows a precise depth of immersion. A potential between the wire and a further electrode in the solution is applied. This electrode is orientated circularly around the wire forming a homogeneous radial field and etching rate. A migration of charge carriers takes place. The total chemical equation looks as follows:

$$\mathrm{W} + 2\,\mathrm{OH}^- + 2\,\mathrm{H_2O} \longrightarrow \mathrm{WO_4}^{2-} + 3\,\mathrm{H_2}. \tag{4.1}$$

The generation of hydrogen gas bubbles is clearly observable and should kept in distance to the wire. Due to the surface tension of the liquid a meniscus is formed besides the wire at the boundary between air and liquid. Here, the etching rate is increased leading to a necking area.

Usually, a dc potential is applied continuously until an electronic control circuit stops the etching process as soon as the bottom part of the wire drops off. Then a sharp tip remains. The cut-off time mainly determines the radius of curvature of the tip. A further etching and thus broadening of the tip apex after the drop off is not favoured.

The pulse method of [105] applied in this work overcomes the problem of an electronic circuit and enables tungsten tips with a radius in the lower nanometer range. It is shown in Fig. 4.4. Again, a dc etching phase is performed at the beginning. The duration determines the total length of the tip and the dc voltage the surface roughness of the wire. In this work best results are yielded with 20 seconds and 6 volts. After that, fast pulses are applied with pulse-on duration of 1 ms and pulse-off duration of 100 ms. During the whole process the necking part is controlled optically by a commercial microscope. When the necking part decreases to only a few microns, slower pulses with 1 second time gap are applied to react precisely in the case of a drop-off. The finished tip is cleaned with ultra-pure water to get rid off solution remnants. The pulse method is advantageous concerning the reproducibility, sharpness and the lack of a critical electronic cut-off.

In this way many attempts were done to verify the reproducibility and to optimize the apparatus for the fabrication of a tungsten tip. However, even with greatest care some troubles may occur. Dust particles on the liquid surface can attach to the necking part and influence etching behaviour and shape. Furthermore, the meniscus can decline if the tension is lowered. This is problematic as the position of the wire needs to be changed in order to recover the meniscus. Also, air pressure fluctuations in the lab cause a motion of the liquid surface and broaden the necking part.
Exemplarily, an image of such a tip is shown in Fig. 4.5.

4.2 Results

With the compact interferometer it is possible to observe electron interference fringes of high contrast. Two results are presented: On the one hand a single interference

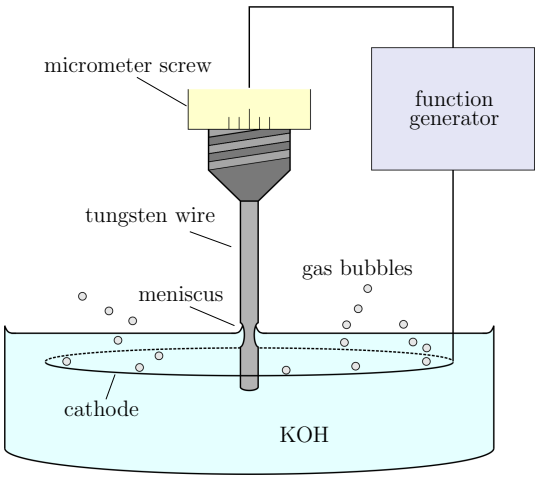

Figure 4.3: Experimental configuration in order to fabricate sharp tungsten tips. A voltage from a function generator is applied to the tungsten wire. A chemical reaction in the KOH electrolyte causes a meniscus right below the liquid surface. At a circular cathode electrode, which ensures a homogeneous radial field, gas bubbles exhaust.

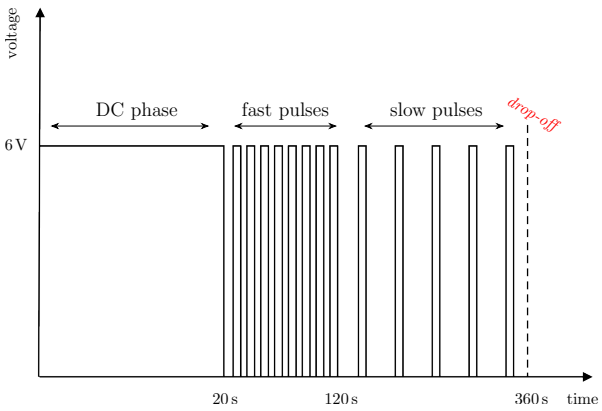

Figure 4.4: Diagram of the applied pulse series for the etching process. A first dc phase provokes the formation of a necking part due to the meniscus. With pulses the etching rate is homogeneous and the wire is smoothed. Slow pulses allow a manual switch-off in time.

pattern is recorded and evaluated in detail with regard to possible perturbing frequencies. Thereby, the correlation analysis comes into play. On the other hand a series of measurements with variable biprism voltages is performed to characterize the device concerning the achievable contrast. In each measurement $5 \cdot 10^5$ particles are detected.

4.2.1 Single measurement evaluation

Interference fringes such as illustrated in Fig. 4.6 (a) can be created reproducibly. Here, a tip voltage of $U_e = -2250\,\mathrm{V}$ and a biprism voltage of $U_{BP} = 0.559 + 0.69\,\mathrm{V}$ is used. Since the fiber is coated with a gold-palladium alloy and the grounded electrodes beside are made of titanium, contact potentials may occur which influence the effective potential interacting with the separated beams [162, 163]. From simulations with the program *Simion* (see section 4.2.3) an extra voltage of 0.69 V is extracted which has to be added to the experimentally applied biprism voltage of 0.559 V. The additional contact potential is in good agreement with the literature values for the work functions of the averaged 80/20 % gold-palladium alloy and titanium [164].

Looking closely on Fig. 4.6, one recognizes a small bend of the fringes in the middle of the rectangle. It is due to a deviation of the beam from the optical axis of the magnifying quadrupole lens. For a proper evaluation of the image, it is corrected by a fourth degree polynomial fit on the fringes. 5 points on the fringes are set manually in the analysis routine of *MatLab* which are then used to arrange and straighten the pattern. The red rectangle is displayed in Fig. 4.6 (b) without a bending. Nine fringes are clearly visible where the colour represents the number of electron hits per pixel.

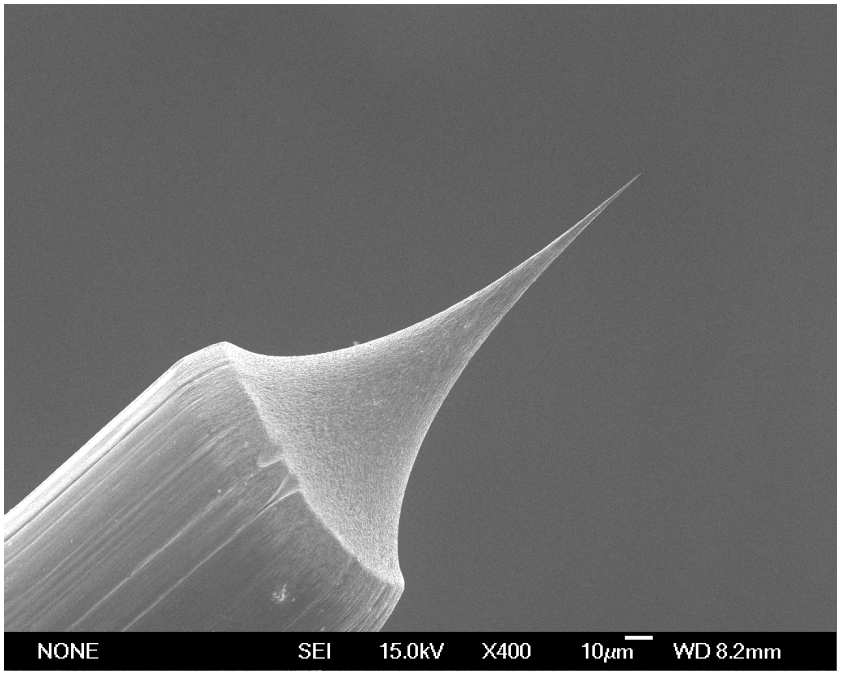

Figure 4.5: Exemplary image of an etched polycrystalline tungsten tip recorded with a scanning electron microscope. The radius of curvature is in the nanometer range. The smooth surface is clearly observable.

Averaging the intensity along the y-direction, the blue graph in Fig. 4.6(c) is obtained. In order to yield the characteristic data of the pattern, a model function $I(x)$ is fitted. By taking into account the influence of the finite fiber radius, the cosine function for a two-beam interference has to be enfolded by a squared *sinc*-function [155]. It is similar to the treatment of the double-slit experiment with finite slit sizes.

According to Eq. (2.7) $I(x)$ is given by

$$I(x) = I_0 \cdot \left(1 + K_m \cdot \cos\left(\frac{2\pi x}{s_m} + \Phi_0\right)\right) \cdot \mathrm{sinc}^2\left(\frac{2\pi x}{s_1} + \Phi_1\right) \quad . \tag{4.2}$$

The measured contrast $K_m = 37.2 \pm 5\,\%$ and the fringe distance $s_m = 0.85 \pm 0.02\,\mathrm{mm}$ are determined by the fit. The average intensity I_0, the phases Φ_0 and Φ_1 and the width of the interference pattern s_1 are additional fitting parameters. The numerical fit works well as can be seen in Fig. 4.6 (c). Compared to the theoretical fringe distance of $s_0 = 338\,\mathrm{nm}$, a total magnification factor

$$M = \frac{s_m}{s_0} = 2517 \pm 6 \tag{4.3}$$

must be considered.

4.2.1.1 Correlation analysis

For the data from Fig. 4.6 (b) a second-order correlation analysis is performed. The correlation function $g^{(2)}(u, \tau)$ is plotted in Fig. 4.7 with the correlation length u and correlation time τ between the detected particles.

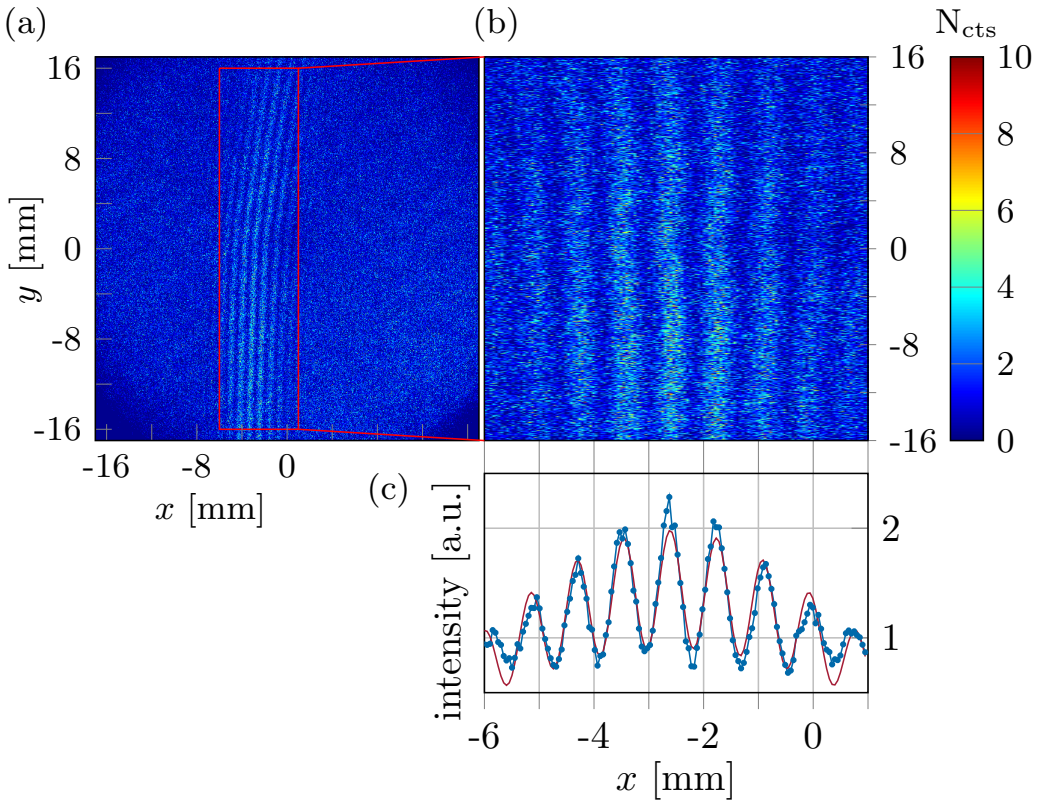

Figure 4.6: (a) Image of an interference pattern. The experimental values are $U_e = -2250\,\mathrm{V}$, $U_{BP} = 0.559 + 0.69\,\mathrm{V}$ and quadrupole voltages $+2960\,\mathrm{V}$, $-2910\,\mathrm{V}$, respectively. (b) Cutout of the area within the red rectangle. The fringes are straightened by a fourth degree polynomial to get rid of a bending. (c) Blue curve: average intensity along the y-direction of (b). Red curve: numerical fit of the intensity [2]. Figure from [2]. Reprints with permission of the American Physical Society (AIP).

By analyzing the correlation function for $\tau = 0$, the contrast K_g and fringe distance s_g of the unperturbed interference pattern can be calculated. The corresponding graph is depicted in Fig. 4.7 (a). Again, according to (2.70) a model function of the following form is fitted:

$$g^{(2)}(u,0) = 1 + \frac{K_g^2}{2} \cdot \cos\left(\frac{2\pi u}{s_g} + \Phi_g\right) + \mathcal{O} \quad . \tag{4.4}$$

The phase Φ_g and the offset $\mathcal{O}$ are further fitting parameters. A fringe distance $s_g = 0.84 \pm 0.02\,\mathrm{mm}$ is obtained with a contrast of $K_g = 42.5\,\%$. It has to be noted that perturbations indeed influenced the initial measurement and blurred the pattern because of $K_g > K_m$. The comparatively high standard deviations for both values arise from a low number of detected particles. This results in a moderate signal-to-noise ratio. Under certain conditions the involved frequencies of the external perturbation can be extracted from the recorded data [116]. Therefore, the amplitude spectrum of the correlation function $\left|\mathcal{F}\left(g^{(2)}(u,\tau)\right)(u,\omega)\right|$ is calculated. In general, it follows from Eq. (2.71) by executing a numerical FOURIER transformation in time at the spatial positions $u = M_u \cdot s_g/2$, $M_u \in \mathbb{N}_0$. At these points, the correlation function becomes

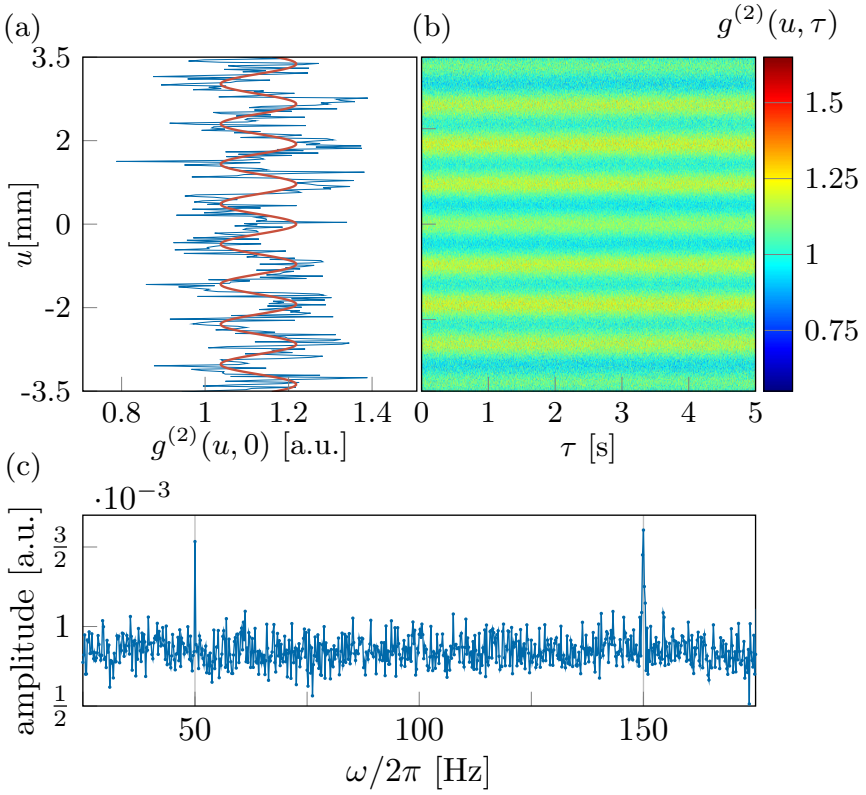

Figure 4.7: (a) Blue graph: the second-order correlation function $g^{(2)}(u,0)$ for $\tau = 0$. Red curve: fit function to yield the contrast and the fringe distance. (b) The second-order correlation function $g^{(2)}(u,\tau)$ extracted from the data in Fig. 4.6 (b). A periodic fringe pattern is revealed. (c) Plot of the amplitude spectrum. It is calculated by a numerical FOURIER transformation of $g^{(2)}(u = M_u \cdot \frac{s_g}{2}, \tau), M_u \in \mathbb{N}_0$ and subsequently averaged. Periodic perturbations of the interference fringes become unvarnished. Two characteristic frequencies at 50 Hz and 150 Hz can be identified [2]. Figure from [2]. Reprints with permission of the American Physical Society (AIP).

maximal [116]. In Fig. 4.7 (c) the average over all amplitude spectra is shown. For numerical reasons, several parameters can be entered in the *MatLab* evaluation code to optimize the computing power and to yield a realistic result with the imported data. Thereby, a spatial discretization step size of $0.371 \cdot s_g$ for the numerical correlation function turned out to be optimal [116]. Two clear peaks at 50 Hz and 150 Hz are evident probably arising from the electric network as the same origin. The corresponding spatial perturbation amplitude is calculated by using Eq. (2.76) to 14.3 nm and 14.8 nm, respectively.

The detection of the utility frequency of electric power supplies demonstrates that our device has a vast application spectrum as a sensor for external perturbation frequencies.

Considering the sensitive measurement of decoherence effects above a gold surface in the next chapter, the correlation analysis opens up new possibilities to expunge disturbing influences in the laboratory and in the evaluation of the data.

4.2.2 Series of measurements

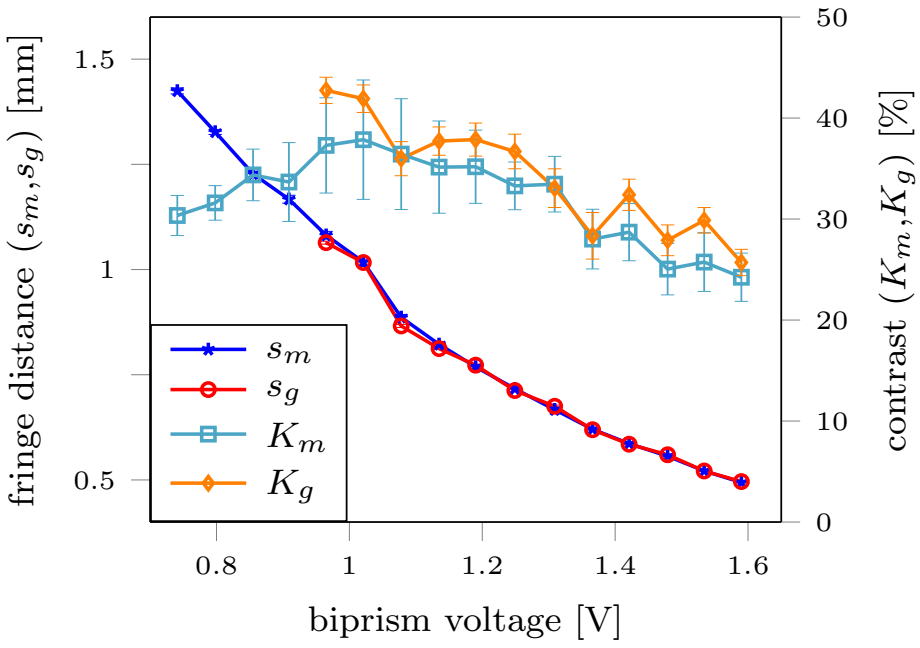

Figure 4.8: Fringe distances s_m and s_g together with the interference contrasts K_m and K_g as a function of U_f. For biprism voltages below 1 V the correlation analysis is not feasible as the influence of diffraction increases and unusable data for the $g^{(2)}$ analysis are generated. As expected from the influence of perturbations, it is $K_g \geq K_m$ [2]. Figure from [2]. Reprints with permission of the American Physical Society (AIP).

A series of measurements is taken with the compact interferometer where the voltage at the biprism fiber is varied. Sixteen data sets are recorded, going from $U_f = 0.051 + 0.69\,\mathrm{V}$ to $U_f = 0.900 + 0.69\,\mathrm{V}$. The evaluation of each data set is done similarly as described before. The results are plotted in Fig. 4.8. Here, both axes of ordinates are denoted by the fringe distance s and the contrast K. The index m refers to the measured data. The index g refers to the received fit values by the second-order correlation analysis.

According to 2.1 the fringe distances decrease with an increasing biprism voltage. This behaviour is valid for both, s_m and s_g. Also, as expected the unperturbed contrast K_g is in general higher than K_m. This is plausible since perturbations can only worsen the contrast of a recorded interference pattern. K_m offers a maximum of 38 % at $U_f \approx 1\,\mathrm{V}$.

For lower biprism voltages the influence of diffraction at the edges of the fiber becomes significant. For higher biprism voltages the transversal coherence properties of the electron source reduce the contrast according to Eq. (2.15).

The unperturbed contrast K_g shows a similar curve shape with a maximal value of 42.7 %. Four data points with a low biprism voltage are not evaluated by the correlation analysis. Due to the influence of diffraction effects the analyzing routine does not work here properly since the theoretical implementation of diffraction is highly complex and not covered in the $g^{(2)}$ correlation theory (see for example [165, 166]).

4.2.3 Simulation

With regard to the desired features of the interferometer, simulations with the software package *Simion* are performed. The attention is turned to a minimization of the design while being capable of creating interference patterns with high contrast. Of course, for the mechanical machining of the components and considering the requirements for a sufficient small superposition angle, boundaries are set for the distance between tip, biprism fiber and quadrupole lens. Taking into account the typical effective source radius of a cold tungsten field emitter of $\approx 1\,\mathrm{nm}$ [77], a distance d_{SB} of only $\approx 300\,\mu\mathrm{m}$ is simulated between tip and biprism. However, for beam adjustment a double deflector is installed in our device with two 2 mm-apertures.

The distance d_{BI} between biprism fiber and quadrupole lens, where the already created interference pattern is magnified, turns out to be more restrictive with regard to the compactness of the device. Since the magnification is limited and the pattern periodicity needs to fit the detector resolution, d_{BI} can not be chosen arbitrary small. If so, the angle of superposition would be too big. The required value of the superposition angle for this simulation is derived by a method described in detail in [5]. Hereby, it is taken advantage of the fact that the biprism fiber deflects every electron by the same angle independent of the distance normal to the fiber [23]. Thereby, the superposition angle can be gained by a classical particle trace simulation allowing conclusions about the quantum interference outcome.

All parameters that determine a minimal but resolvable fringe periodicity can be found in Eq. 2.13. It has to be mentioned that the design is further limited by electric insulation of the quadrupole lens since higher magnifications can only be achieved by increasing the voltage. As the two copper shells and the components within are densely mounted, arching will occur. In this context, the use of MEMS (micro-electromechanical system) technology could improve the compactness and reduce the necessary voltages [167, 168]. In summary, the following values are set and obtained by the simulation with respect to the measurement:

- A tip voltage of $-2250\,\mathrm{V}$.
- A biprism voltage of $(0.559 + \delta)\,\mathrm{V}$ where the contact potential is determined to $\delta = 0.69\,\mathrm{V}$.
- A quadrupole voltage of $2960\,\mathrm{V}$ normal to the fringes and $-2910\,\mathrm{V}$ parallel to them.
- $d_{SB} = 19\,\mathrm{mm}$, $d_{BI} = 28\,\mathrm{mm}$.
- $\Theta = 7 \cdot 10^{-5}\,\mathrm{rad}$.
- An unmagnified pattern periodicity of 369 nm and a magnification of 2886.

A theoretical fringe distance of 338 nm is derived which fits well to the simulation.

The good agreement of our simulations show that in principle, more complex beam path simulations can be executed with high reliability. In order to increase the sensitivity towards vibrational or electromagnetic dephasing and inertial forces, a larger beam path separation is required within a new interferometer scheme including three biprism fibers [169, 5].

5 Decoherence of electron matter waves interacting with a gold surface

5.1 The main biprism interferometer

The biprism interferometer described in this chapter is a further development of the one built by Sonnentag [67]. Many parts are adopted, mainly deflecting and magnifying assembly parts. Here, a short summary of the technical aspects is given that are essential for decoherence measurements. Technical drawings and general construction principles can be found in [67, 125, 170] more extensively.

A drawing of the interferometer setup is depicted in Fig. 5.1. The coherent electron beam is emitted by a single-atom tip. By taking advantage of applying a voltage to the first aperture (counter electrode), the count rate is increased without affecting the coherent properties of the beam (see chapter 3). Electron energy and current are tunable independently.

Due to the cylindrical shape and the use of an optical bench, all parts are well centered and in line from the beginning. However, several deflector elements and image rotating coils ensure the alignment of the beam to the optical axis as minor deviations and distortions can not be avoided completely.

As usual for biprism interferometers, the biprism fiber coated with a gold-palladium alloy causes a uniform wave front splitting of the electron matter waves with constant deflection angle for all beam paths. The typical applied voltage is of the range of a few hundred volts. For reasons of a homogeneous potential distribution the fiber is placed between two grounded electrodes. To make the creation of an interference pattern possible, the coherently illuminated area on the fiber plane needs to be wider than the fiber diameter of 350 nm.

The gold surface as a macroscopic environment for the separated electron wave packets is inserted into the beam path and is described in section 5.2 in more detail.

The Wien filter allows to correct a longitudinal shift of the two separated wave packets by using a combination of electrostatic and magnetic fields. The shift arises when the wave packets traverse deflector elements on different potentials. The Wien filter is operated in the compensated mode where the electric and magnetic force cancel each other and thus, the beam trajectory remains unaffected.

The magnification of the interference fringes is done by three electrostatic quadrupole lenses. The advantage hereby is that the magnification takes place only in one direction, depending on the polarity of the individual electrodes. Here, a magnification perpendicular to the fringe direction is desired while barely signal is lost lengthwise. Usually, the magnification factor is of the order of a few thousand.

For the detection of the interference pattern, a delayline detector is mounted to the vacuum chamber which records all incoming particles with high temporal and spatial resolution. All data is transferred to a computer which allows to store and read-out the information easily. Former interferometer experiments, which used a phosphor screen in combination with a fiber optic and a slow-scan charge-coupled device (CCD) camera to display the particle impacts [56, 67], offer several drawbacks compared to the delayline detector:

- The spatial resolution of 288×384 pixels was very low.
- Cooling of the chip was needed to reduce the dark current noise. However, the dark signal is very sensitive to the stability of the temperature.
- Blooming effects of the chip produced image errors.
- High count rates and long integration times led to a fast saturation of the pixels (full well capacity ≈ 40000).
- The detection quantum efficiency and modulation transfer function needed to be characterized. Their estimation is experimentally complex and made several assumptions necessary [56, 171, 172].
- From CCD cameras there is no temporal information available which is mandatory for the $g^{(2)}$-correlation analysis.

The whole setup is in ultra-high vacuum which is created by a scroll compressor and a turbomolecular pump. After the bake-out of the chamber those pumps are uncoupled by an angle valve. From then, the vacuum in the lower 10^{-10} mbar range is maintained only by an ion pump to keep the chamber vibration-free. Additionally, a higher pump rate is achieved by sublimating titanium from filaments which are run with a periodic electric current of 43 A. Using liquid nitrogen for an additional cryopump residual gas particles become even better absorbed.

Several demands on the interferometer have to be realized to ensure the integration of an interference pattern with high count rate and contrast. First of all, the interferometer has small components with an uniform outer diameter of 28 mm. The construction technique allows an easy change or improvement of the elements. A low mass compared to early electron microscopes and its compactness and rigidity are further advantageous [125]. Thus, a high mechanical resonance frequency of the system is achieved which makes it insusceptible to low-frequency vibrations. All optical elements are aligned by clamping them on two parallel ceramic rods.

Since the interaction with external magnetic ac fields is stronger for slow electrons, the whole interferometer is enclosed by a Mu-metal tube with a high permeability in the range of $\approx 10^5$. Therefore, those magnetic fields are reduced significantly. The disturbing influence of electric high-frequency fields is ruled out due to the metallic vacuum chamber serving as a Faraday cage.

However, unwanted stray pick-ups may occur over the electric leads for the interferometer elements which form a kind of antenna for varying signals. Former experiments showed a major susceptibility for alternating signals in the MHz regime [170]. This range is widely used for radio- and television communication.

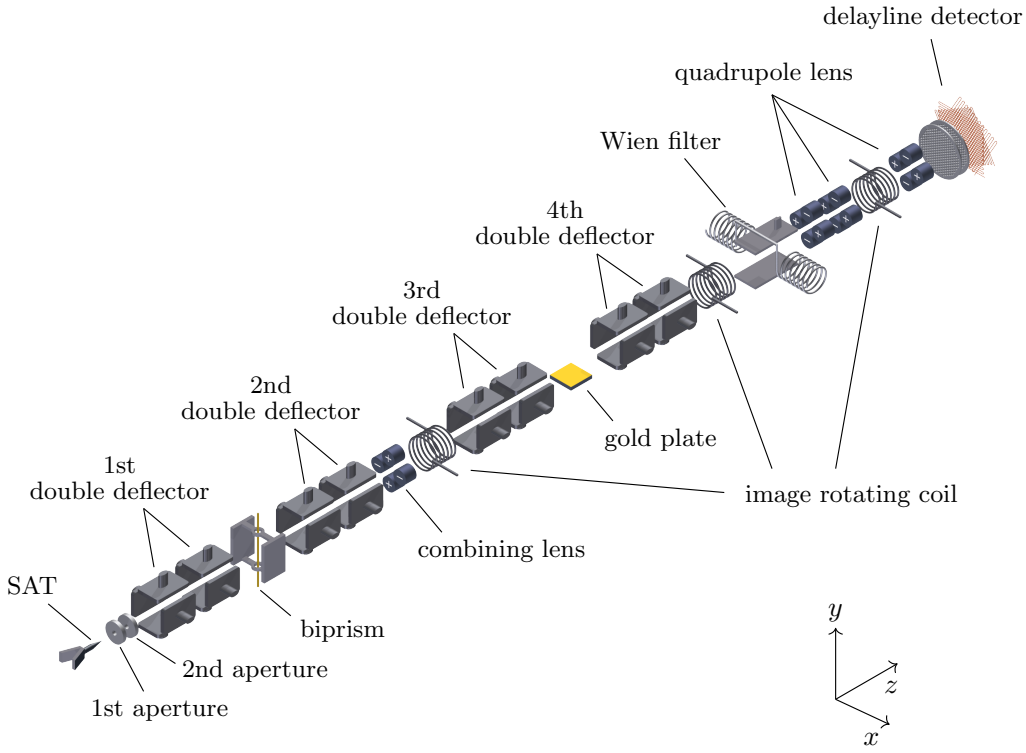

Figure 5.1: Schematic sketch of the interferometer for measuring decoherence effects of electrons above a gold surface.

For that reason all feedthroughs of the supply voltages are protected by a filter circuit. This low-pass filter mainly consists of an inductance in series with 68 μH and a capacitor in parallel with 10 nF. It is integrated as near as possible to the interferometer in the three plug connectors which are screwed on the chamber. Furthermore, ferrite shielding beads cover the small leads in the plugs as it is shown schematically in Fig. 5.2.

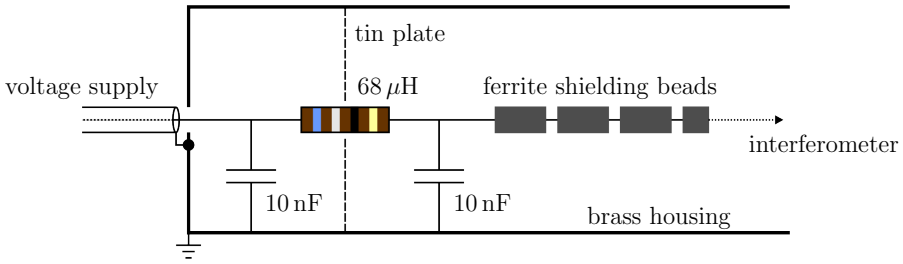

Figure 5.2: Low-pass filter consisting of one choking coil and two ceramic capacitators. Placed inside the multi-pin plugs and the cathode lead, input coupling of high-frequency electromagnetic fields is avoided. As a first approximation the threshold frequency is at 200 kHz which is sufficient for a nearby located radio- and television transmitter.

Such beads are made out of ferromagnetic material and act as a passive choke. High-frequency noise on the leads is damped but also sheath currents from the electronic devices are suppressed. Additionally, for the failure-free operation of the elements the electronic devices are run by car batteries to avoid mains hum. Only for the tip voltage it is not possible to refrain from mains operation. By means of a pick-up coil with display the influence of different sources of electromagnetic disturbance in the lab is estimated. Subsequently, effort is made to reduce this disturbance, e.g. by replacing electrical components or by improving the grounding.

All apertures in the interferometer are made of high purity titanium. They are critical with regard to electron bombardment leading to higher gas desorption and worse vacuum conditions. In particular, the stability of the electron current might be impaired [173]. Furthermore, the creation of secondary and stray electrons should be kept to a minimum. Titanium is well suited because its backscatter coefficient for electrons is notably low. A further decrease of the rate of outgassing can be achieved by annealing the aperture in vacuum with temperatures up to 1300 K.

In sum, the most important parts of the interferometer of [66, 67] are replaced and new designed, namely the field emitter, the biprism fiber, the decoherence surface and the detector. Together with new electronic power supplies, it is shown that these improvements pave the way to realize decoherence measurements above a gold surface [1–3, 116].

5.2 Gold plate

The gold plate as a macroscopic object is inserted into the electron beam path of the interferometer and thus causes the loss of contrast of the interference pattern due to decoherence mechanisms described in section 2.2. The translation is achieved solely

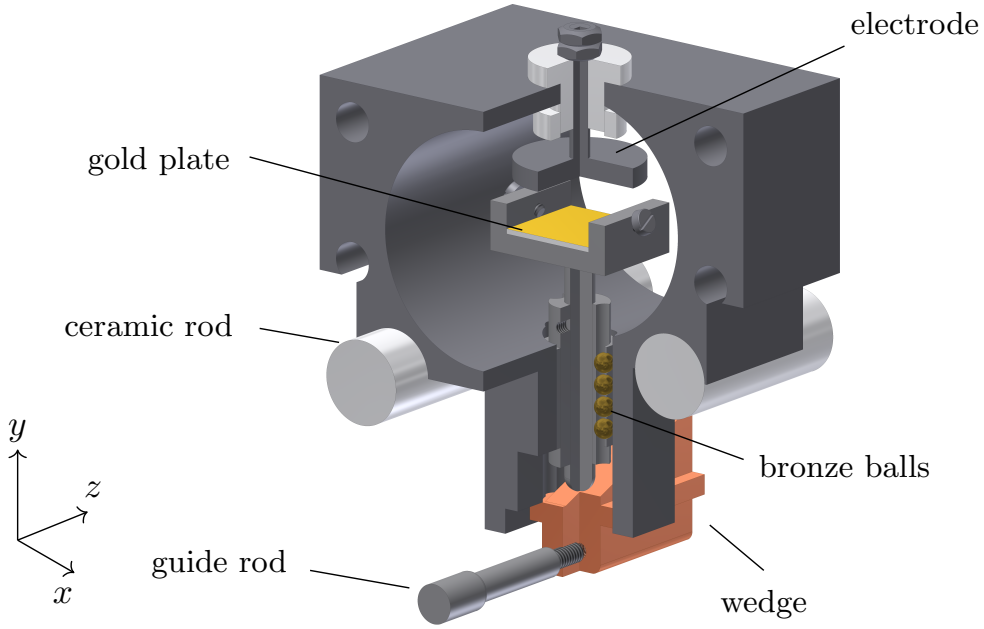

Figure 5.3: Model of the assembly in order to move the gold plate into the beam path. Like all interferometer parts the assembly is tightly clamped on two parallel ceramic rods. The inside gold plate is screwed on two sides onto a holder which is shifted vertically by a ball bearing consisting of eight bronze balls. A long guide rod is connected to a micrometer screw positioned outside of the chamber. It allows for a precise movement of the plate since the direction change of the force is carried out by a wedge. The upper electrode is grounded. The beam propagation is in z-direction.

mechanically by using a ball bearing in combination with a wedge which allows to move the holder of the gold plate in y-direction perpendicular to the beam propagation, see Fig 5.3. In order to circumvent a hole in the Mu-metal tube and to maintain the shielding, a long guide rod is connected to the wedge which changes the direction of motion of a micrometer screw by 90 degrees. The micrometer screw is positioned outside the chamber and allows for a precise adjustment of the plate height in the micrometer range. Since oil lubrication for movable parts is prohibited in vacuum, the ball bearing and the wedge is made of bronze due to its low coefficient of friction.

The first installation of a gold plate as a resistive material was done as a top layer of a strontium titanate substrate (STO) with dimensions $10*10*1$ mm. A rigorous chemical cleaning of the substrate before gold coating is performed with acetone, isopropyl alcohol and ultra-pure water while being in fluid continuously. On the application of the industry standard RCA cleaning method is waived since internal contaminants and oxide layers are without concern [174]. Moreover, short etching of the surface probably increases the surface roughness. In case of remaining small impurities, which can be observed as dark grains under a light microscope, pressurized nitrogen is used to get rid of them. Clean substrates are evaporated with 3 nm thick titanium serving as adhesive layer for gold. Subsequently, gold is coated on titanium with a thickness of 50 nm. The surface roughness is determined via atomic force microscopy (AFM) to be ≈ 5 nm. However, while working with the gold plate using a STO substrate in the interferometer experimentally, it turned out that an electric charging of the plate took place even though two grounded screws are in direct contact with the gold surface. Unfortunately, long integration times became impossible. For that reason, the STO substrate was replaced by a piece of silicon wafer with equal size serving as the carrier material of the gold layer. Indeed, due to a better conductivity the charging vanished.

5.2.1 Resistivity measurement of the plate

In order to determine the specific resistivity ρ of the gold surface, a measurement based on the VAN DER PAUW method was executed [175]. Thin layers are specified by their low thickness between a few nm up to several hundred microns.

A model to explain the dependency of the specific resistivity of thin metal layers is drafted in [176]. FUCHS describes that the conductivity σ of a metal with few atomic layers thickness drops below the conductivity of bulk metal (σ_0). The mean free path λ_0 of conduction electrons is of the same order as the material thickness d and becomes shortened. Thereby, scattering of the electrons at the boundaries takes place which is classified in elastic and inelastic scattering. As a result he receives

$$\frac{\rho}{\rho_0} = \frac{3}{4}\Big(1-\epsilon\Big)\kappa \log\frac{1}{\kappa} \approx 0.34 \quad . \tag{5.1}$$

Here, ϵ denotes the fraction of elastic scattered electrons and $\kappa = d/\lambda_0 = 2.38$. The mean free path for gold is 42 nm [177]. For very thin layers ϵ approaches to zero which means that electrons are scattered in all directions arbitrarily.

In [178] the FUCHS- SONDHEIMER- model is expanded and elaborated to more detail. However, the given formulae are still of similar form.

For $\kappa \gg 1$ the following formula is derived for our setup:

$$\frac{\rho}{\rho_0} = \left(1 + \frac{3}{8\kappa}\right)^{-1} \approx 0.53 \quad . \tag{5.2}$$

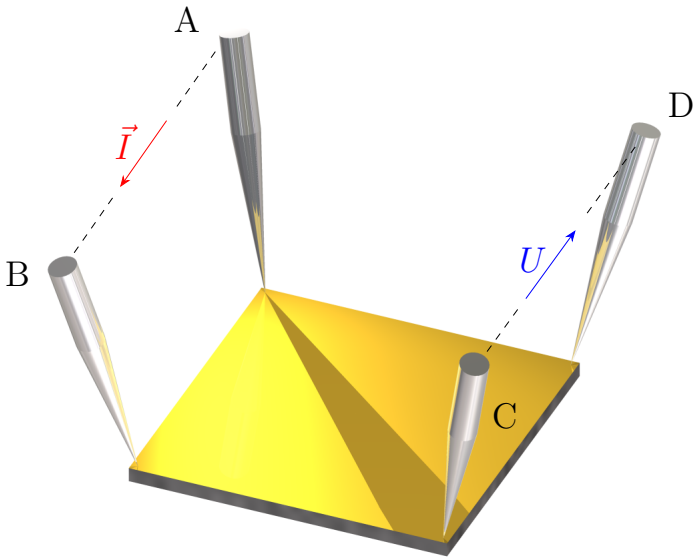

Figure 5.4: According to VAN DER PAUW four measuring tips are located at the outer rim of the sample. A current I is supplied between A and B and the potential difference U between C and D is quantified. A resistivity $R_{\mathrm{AB,CD}}$ can be determined.

A sketch of the measurement principle is depicted in Fig. 5.4. An arbitrary formed but homogeneous sample without (geometrical) holes is connected to four measuring tips (A-D) at the outer rim. The gold is coated onto a silicon wafer sample via magnetron sputtering which indicates that the thin film is connected continuously with no isolated grain boundaries. A resistivity

$$R_{\mathrm{AB,CD}} = \frac{U_{\mathrm{CD}}}{I_{\mathrm{AB}}} \tag{5.3}$$

is measured by supplying a current I_{AB} between A and B and determining the resulting potential difference U_{CD} between C and D. In the same manner by cyclic commutation of the contacts anticlockwise, $R_{\mathrm{BC,DA}}$ is quantified. By means of conformal mapping and using complex functions on an infinity half-plane it can be shown that the shape of the sample is of no importance and the following equation is valid [175]:

$$\exp\left(-\frac{\pi d}{\rho} \cdot R_{\mathrm{AB,CD}}\right) + \exp\left(-\frac{\pi d}{\rho} \cdot R_{\mathrm{BC,DA}}\right) = 1 \quad . \tag{5.4}$$

Since the gold plate has a line symmetry between the four contacts, it follows that $R_{\mathrm{AB,CD}} = R_{\mathrm{BC,DA}}$. Then, Eq. (5.4) becomes simply to

$$\rho = \frac{\pi d}{\ln 2} \cdot R_{\mathrm{AB,CD}} \quad . \tag{5.5}$$

Although a great importance was attached to the performance of the measurements, a huge discrepancy between the measured and expected resistivities exists. Inserting all measured properties into Eq. (5.5), the measured resistivity becomes to $\rho_m = 3.01 \cdot 10^{-5}\,\Omega \cdot \mathrm{m}$. Compared to literature values ($\rho = 2.2 \cdot 10^{-8}\,\Omega \cdot \mathrm{m}$) of bulk gold, this difference seems to be too large. Probable reasons for this difference are the not exactly known thickness which is determined via coating of test structures, contact problems of the measuring tips or even a too high contact pressure which flakes off the surface coating layer.

It shall be noted also that the method is exact only for point-like contacts. Moreover, a small error occurs when a measuring tip is a distance l away from the edge of the plate. It is in the range of $\Delta\rho/\rho \approx l^2 \cdot (2L^2 \ln 2)^{-1} = 0.029$ with the plate length L [175]. Applied to four measuring tips, this error increases obviously stronger.

Unfortunately, the theoretical model does not explain the discrepancy. A large uncertainty in several parameters exists and the exact application of the theory to our case is still unclear. For that reason and because the decoherence theory is calculated with literature values of the resistivity of gold, the actual value for the plate is assumed to be in the same range as the literature value.

5.3 Interference measurements

There are several demands for the experiment. A sufficient big lateral separation Δx between the separated wave packets needs to be achieved and the beams shall traverse the plate in small distance z parallel to the surface.

5.3.1 Noise sources

A prerequisite for sensitive decoherence measurements is the tracing and elimination of noise sources in the laboratory. As the room is crowded with electronic devices and cables, many various electromagnetic fields exist and may influence the measurement of an interference pattern.

In general, some parts of the equipment are not necessarily needed and can be switched off during measurements. For example, this is the case for neon tubes at the ceiling, the loudspeaker unit, computer monitors and also for AC power sockets at the side panel.

However, it turned out that none of the mentioned objects cause a reduction of the interference contrast. This finding was verified by several measurements with all combinations of switched off/on parts. Even walking in the lab does not disturb the recording since the interferometer is placed on a separated base plate.

An exception is a second computer monitor, used for alignment work and setting the correct parameters, in direct vicinity of all power supplies and the detector. The comparison of Fig. 5.5 and Fig. 5.6 states clearly that this monitor washes out the integrated image. This is easy to understand as strong electromagnetic radiation is strayed into the near located unshielded lemo cables which carry the unamplified signals.
The second monitor is therefore switched off for all serious measurements.

In order to avoid electric crosstalk with 50 Hz mains hum, power supplies and devices for the interferometer are completely run with car batteries with the exception of the

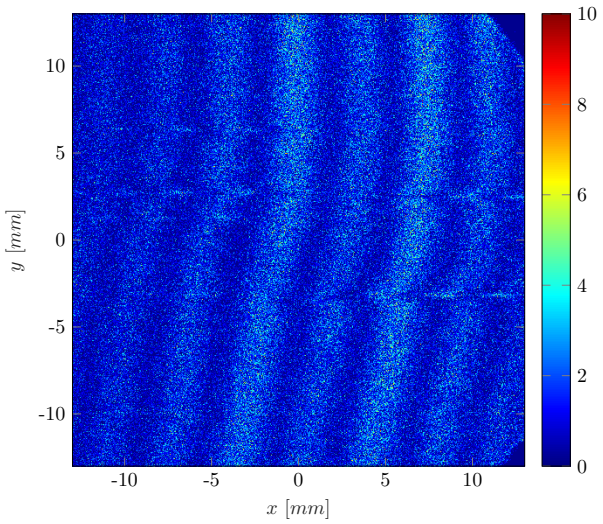

Figure 5.5: Interference pattern recorded while the second monitor is switched off.

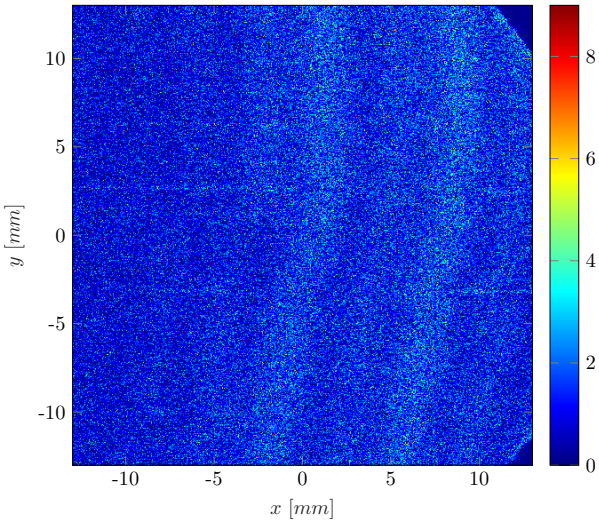

Figure 5.6: Interference pattern recorded while the second monitor is switched on.

voltage supply of the field emitter and the delayline detector. However, the detector can also be connected to the car batteries but has a high power consumption and may lead to discharge of the batteries.

To decide if the connection of the detector to the batteries is meaningful, a comparison measurement is done where an interference pattern is recorded with identical settings. In Fig. 5.7 the detector is run with the electric power from the network whereas in Fig. 5.8 it is run with the batteries.

The difference is observable on closer examination. With the correlation analysis for both measurements a contrast of 42.9 % and 45.3 %, respectively, is extracted.

The improvement in contrast is comparable small but cannot be neglected for sensitive measurements. Although there is a non-measurable uncertainty due to intensity flickering of the emitter ([106]) or thermalisation drifts of the coils, the detector is run by batteries in all following sensitive measurements.

5.3.2 Beam path separation

In general, the strength of the decoherence effect increases with increasing beam path separation, see Fig. 2.2. Therefore, it is desirable to achieve a maximal possible beam path separation above the gold surface.

For realizing large separations, one might think of simply enlarging the fiber diameter. This, however, is limited by the fact that the coherent illuminated area is finite and the required magnification afterwards would increase drastically because the superposition angle increases.

Because of that various beam path arrangements have been tested in the literature concerning biprism interferometry in order to achieve a wide separation together with an acceptable (unmagnified) fringe distance (e.g. [179, 61, 180, 67]).

Concerning the reproducibility, visibility and sufficient magnification perpendicular to the plate surface, a beam path with negative charged fiber, combining quadrupole lens, two further dividing quadrupole lenses and one last combining lens turned out to

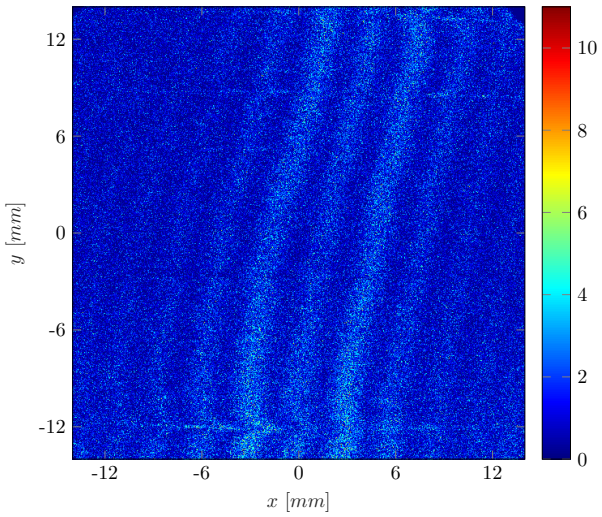

Figure 5.7: Interference pattern recorded with the delayline detector connected to the electric network.

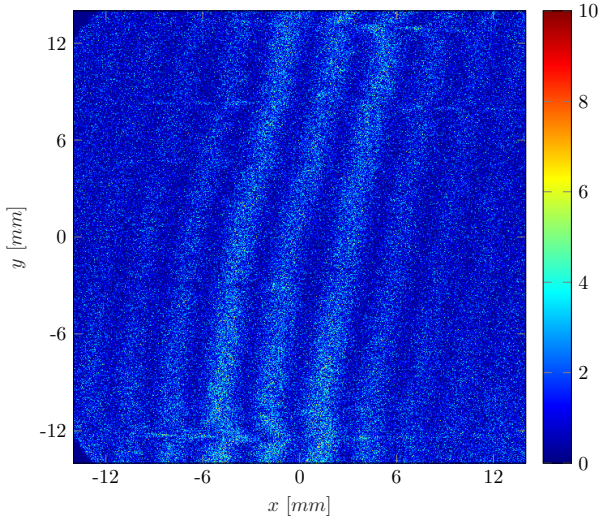

Figure 5.8: Interference pattern recorded with the delayline detector connected to the car batteries.

be optimal. This finding is supported by two different ways of simulation.

First, the software package *Simion* is used where electric fields for given geometries and trajectories of charged particles are calculated by means of finite difference methods. It is originally designed for the simulation of three dimensional lens systems and is versatile applicable for our interferometer configuration. Successful calculations in [5] were already done with *Simion*.

A second method for determining the beam path separation in our interferometer is the use of general transfer matrices as known from ray optics. For that, all parameters like voltage and distance of the relevant parts are inserted into *MATLAB*. The propagation of the electron beam is hence calculated stepwise from one part to the next one.

The following experimental data are entered in the program.

- Tip voltage: $U_e = 800\,\mathrm{V}$
- Distance from tip to biprism fiber: $78\,\mathrm{mm}$
- Distance from biprism fiber to quadrupole lens: $30\,\mathrm{mm}$
- Length of the quadrupole lens: $l_{\mathrm{QP}} = 10\,\mathrm{mm}$
- Inner radius of the quadrupole lens: $d_{\mathrm{QP}} = 3.4\,\mathrm{mm}$
- Diameter of the biprism fiber: $d_f = 350\,\mathrm{nm}$
- Distance from biprism fiber to grounded electrodes: $R = 2\,\mathrm{mm}$
- Distance from quadrupole lens to the middle of the plate: $51\,\mathrm{mm}$

The transfer matrices represent the distance to the optical axis and its enclosed angle. The beam is characterized as a vector with both components. As the beam traverses

an optical element, the corresponding transfer matrix is multiplied to the beam vector and thus changes the properties [155].

For free space distances it is simply

$$\begin{pmatrix} r_2 \\ \alpha_2 \end{pmatrix}_d = \begin{pmatrix} r_1 + d\alpha_1 \\ \alpha_1 \end{pmatrix} \quad . \tag{5.6}$$

where the angle $\alpha_2 = \alpha_1$ remains the same. For the description of the biprism fiber the transfer matrix becomes more complicated concerning Eq. (2.10):

$$\begin{pmatrix} r_2 \\ \alpha_2 \end{pmatrix}_f = \begin{pmatrix} r_1 + e \cdot U_f \cdot \frac{d_f}{2mRv_x^2} \\ \alpha_1 - \frac{\pi}{2\ln(2R/d_f)} \cdot \frac{U_f}{U_e} \end{pmatrix} \quad . \tag{5.7}$$

The quadrupole lens shows a periodic behaviour in both, the x- and y- direction [150]. As we only consider the plane which is defined by both negative charged electrodes and the tip position (x-z-plane, see Fig. 5.1), the transfer matrix becomes

$$\begin{pmatrix} r_2 \\ \alpha_2 \end{pmatrix}_{QP} = \begin{pmatrix} r_1 \cos(kl_{\mathrm{QP}}) + \alpha_1 \sin(kl_{\mathrm{QP}})/k \\ -r_1 \cdot k \cdot \sin(kl_{\mathrm{QP}}) + \alpha_1 \cos(kl_{\mathrm{QP}}) \end{pmatrix} \quad , \tag{5.8}$$

with a factor $k = \sqrt{U_{\mathrm{QP}}/(d_{\mathrm{QP}}^2 \cdot U_e)}$. For the total calculation of Δx all matrices have to be multiplied. Thereby, the starting point is the tip which is assumed to be on the optical axis with zero lateral distance. The starting angle is supposed to be the minimal angle where the beam barely does not strike the biprism fiber.

It has to be mentioned that for a precise calculation the diameter of the biprism fiber is very decisive. This is another reason why the controlled fabrication process of the fibers (see section 3.1.4) is important in our experiment. In former experiments the fiber was drawn manually without being aware of the real diameter [66, 67].

In both simulations only the relevant parts for the beam separation are considered while disregarding for example all apertures of the deflector elements. This, however, is justified as long as the beam reaches the detector at all since the apertures can only block the beam.

The voltages of the biprism fiber and the first superimposing quadrupole lens as most important properties are both listed in Table 5.1.

5.3.3 Vertical magnification

In order to determine the magnification of the quadrupole lenses along the interference fringes and perpendicular to the plate surface, the adjustable height of the gold plate within the beam path is utilized.

Therefore, for several positions of the micrometer screw an image of the plate shadow is recorded. The change of the height on the detector is associated to the adjustment

$U_{\mathrm{QP}}\,[V]$ / $-U_f\,[V]$	10	20	30	40
0.2	6.36	4.37	2.46	0.61
0.4	12.26	8.59	5.04	1.61
0.6	18.16	12.80	7.62	2.61
0.8	24.07	17.02	10.20	3.61
1.0	29.97	21.24	12.78	4.61

Table 5.1: Beam path separations at the center of the gold plate in [μm] for different pairs of biprism voltage U_f and first quadrupole voltage U_{QP}.

travel of the screw. However, the angle of inclination of the wedge for moving the plate has to be taken into account which is 22 °. That means that the change of direction from horizontal to vertical needs to be modified by a factor of 0.4 .

Exemplarily, a series of images is presented in Fig. 5.9. The pictures on the left side show the plate shadow which is moving upwards with increasing scale divisions. The specification of the precise plate position is difficult insofar as the rim is blurred due to electrons which are scattered from the surface or deflected from dust particles. Moreover, the plate seems to be curved because of aberrations from the axis of the quadrupole lenses.

However, the plate position is determined by corresponding numerical fits shown in the pictures on the right side of Fig. 5.9. The intensity is averaged for each row of the y-axis. Subsequently, a fit function of the form $f(y) = a \cdot \arctan(y - b) + c$ is applied with the fitting parameters amplitude a, displacement b and offset c. The plate position is defined as the point with the biggest slope of the fit function. Here, the change from the shadow area to the illuminated area is most distinctive. This point is represented by the displacement b where the derivative of the arc tangent is maximal. In the pictures, it is marked on the axis with red colour and with a dotted line in the images.

As the detection area is circular and the created image from *MATLAB* rectangular, a region with zero counts in the corners appears and leads to a drop of counts for $y > 10\,\mathrm{mm}$. Thereby, the fit becomes worse. However, the plate position remains the same.

The resulting values for the plate position in this example are $-14.7\,\mathrm{mm}$, $-8.5\,\mathrm{mm}$, $-2.4\,\mathrm{mm}$, $3.6\,\mathrm{mm}$, $9.6\,\mathrm{mm}$, respectively. Thus, the mean difference from one image to the next one is $6.1\,\mathrm{mm}$. The plate thereby is moved fifteen scale divisions which correspond to $60\,\mu\mathrm{m}$. In total, the vertical magnification in this example is easily

calculated: 1 mm shift on the detector screen correlates to a vertical shift of the plate of 9.8 μm.

Noticeably, the plate movement is very linear which is important for a correct evaluation of the height determination.

The knowledge of the vertical magnification allows to estimate the length proportions of detected interference fringes and to check if this magnification is sufficient to resolve decoherence effects near the surface with respect to theoretical predictions.

5.4 Measurement series

The study of decoherence effects of free electrons near a gold surface is an ambitious experimental undertaking which requires a thorough and careful handling of all interferometer parts. The sheer range of adjustable parameters of four double deflectors and quadrupole lenses is enormous. Therefore, a lot of tests and runs were performed in order to optimize the beam path concerning fringe contrast, count rate, magnification and favourable position of the plate.

Particularly, a high count rate and magnification are in direct conflict of each other. Thus, a compromise has to be found where the integration of several hundred thousand particles takes place within an acceptable time (concerning dephasing drifts or signal instabilities) and the magnification is sufficient. Besides, a too long integration time increases the probability that the single-atom tip changes its emission properties. This incident, which unfortunately happened many times, makes the measurement unusable.

In order to examine the decoherence effect dependent on the height z and beam separation Δx, the following beam path configuration is applied:

- The biprism fiber is set on negative potential compared to ground. The electron wave is split and guided away from the optical axis.
- The first image rotating coil corrects a possible misalignment between fiber and first quadrupole lens.
- The first quadrupole lens deflects the partial waves back to the optical axis.
- The magnification of the interference pattern is achieved by three further quadrupole lenses. Two of them enlarge the pattern perpendicular to the fiber axis whereas the last one ensures the magnification in z-direction.

Thereby, several demands on the beam path are fulfilled as for example a good beam path separation over the plate, a resolvable fringe distance and a sufficient number of fringes in the detector plane. In addition, the vertical magnification has to be chosen properly so that the transition region from zero decoherence to complete decoherence is captured in the active detector area.

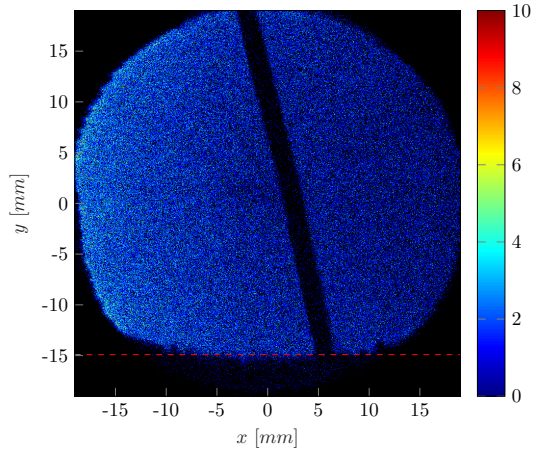

(a) Image of the plate shadow for a scale division of 21.15.

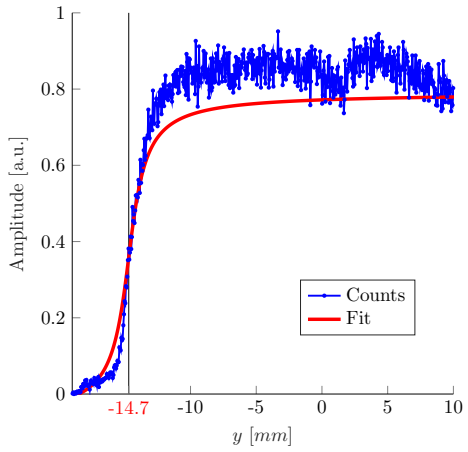

(b) Numerical determination of the plate position for a scale division of 21.15.

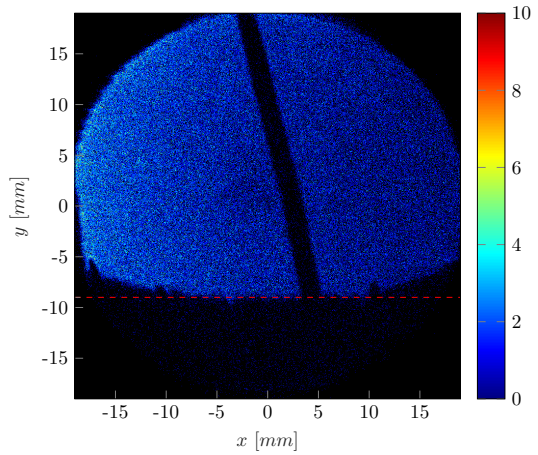

(c) Image of the plate shadow for a scale division of 21.30.

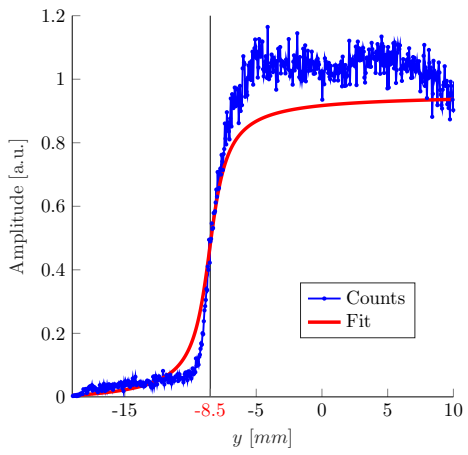

(d) Numerical determination of the plate position for a scale division of 21.30.

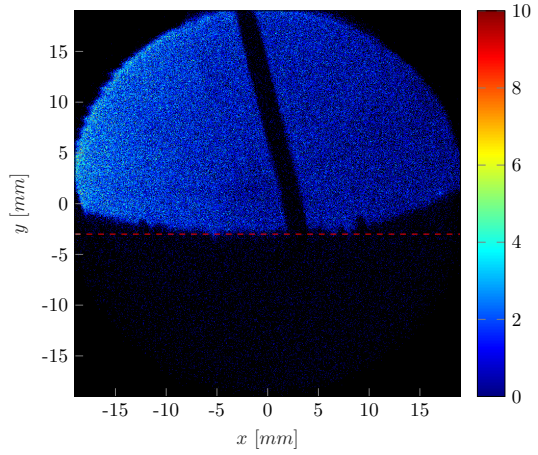

(e) Image of the plate shadow for a scale division of 21.45.

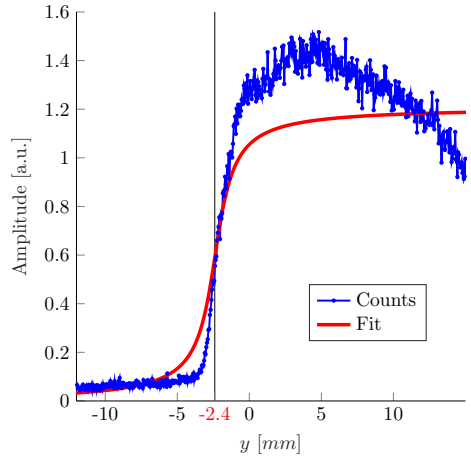

(f) Numerical determination of the plate position for a scale division of 21.45.

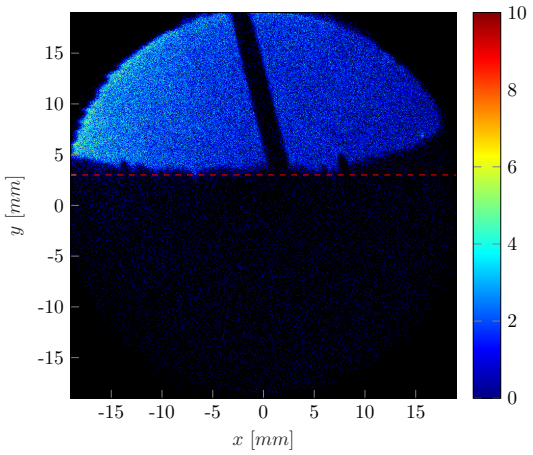

(g) Image of the plate shadow for a scale division of 21.60.

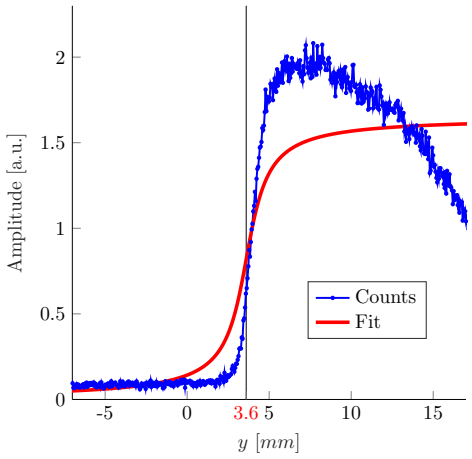

(h) Numerical determination of the plate position for a scale division of 21.60.

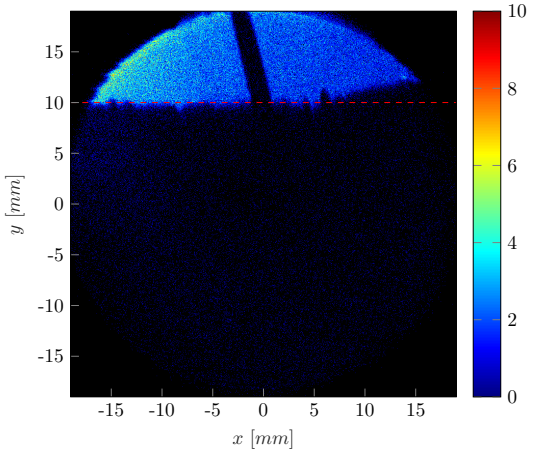

(i) Image of the plate shadow for a scale division of 21.75.

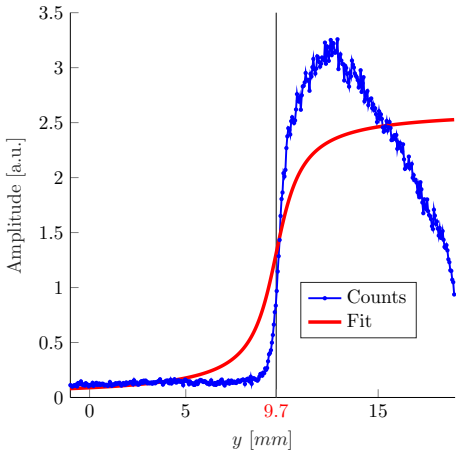

(j) Numerical determination of the plate position for a scale division of 21.75.

Figure 5.9: In order to determine the vertical magnification, a series of images at different positions of the micrometer screw is recorded. The screw is equipped with a scale. The rotation about one scale division is equal to a vertical shift of the plate of 4 μm. To extract the plate position in the pictures (a), (c), (e), (g), (i), a numerical fit is used in the corresponding plots (b), (d), (f), (h), (j) of the amplitude along the y- direction. The result is marked both, by a dashed red line in the image and on the axis in the amplitude plot.

5.4.1 Variation of Δx

The measurement series shown in Fig 5.10 represents only one among many other examples where the images are qualitatively the same. Here, the aim is to vary the beam path separation by applying different negative voltages to the biprism fiber. All residual settings are kept constant to draw conclusions from this parameter.

In this measurement series a voltage of $-1600\,\mathrm{V}$ is applied to the single-atom tip. The counter electrode is biased with 160.3 V compared to ground. The biprism voltage is altered from $-0.45\,\mathrm{V}$ to $-0.73\,\mathrm{V}$ which is equivalent with a beam path separation between 5.86 μm and 9.29 μm. For recombining the electron waves, the electrodes in the horizontal plane of the first quadrupole lens are on $-29.4\,\mathrm{V}$. For the magnification only two of three further quadrupole lenses are biased with 1852 V and 296.6 V, respectively.

The evaluation routine is for all graphs the same. Firstly, the listmode file of the detector, where all information of the recorded particles is stored, is read in *MATLAB*. Subsequently, a straight line is fitted to the plate surface in order to rotate the data and align the plate horizontally. Simultaneously, the data is limited to a selectable rectangular image section. It is displayed by creating a histogram of the data with a binning size of 0.05 . This factor defines the number of vector elements per class length of the binning.

As a next step, the position of the plate is determined as described in section 5.3.3. This is important to rescale the vertical axis and to set the zero point of the height z.

In order to correct a possible curvature of the fringes due to boundary fields of the quadrupole lenses, a fourth degree polynomial of the form $ax^4 + bx^3 + cx^2 + dx + e$ is fitted to the fringes. Therefore, six points in the histogram are selected manually. The fringes get straightened by modifying the horizontal axis with the yielded fitting parameters a, b, c, d, e. With that all fringes are perpendicular to the plate surface.

A final cut of the image section is now reasonable where the limits need to be set properly with respect to the interference pattern width. A too big image section would downgrade the contrast determination as a major part would not be covered by the fringes. A too small image section would cut off fringes and lose information of the interference pattern. In Fig. 5.10 a horizontal width of 24 mm of the detector is examined. It is slightly more than half of the diameter of the detector area (40 mm).

The upper limit in vertical direction is decisive for the number of data points. It should be chosen as big as possible to make sure that the interesting contrast transition lies within this region. However, the circular shape of the detector has to be considered when a rectangular image section is extracted. The upper corners must not protrude from the active detector area.

With the well prepared image section of the original recorded data the contrast is determined for different heights. Therefore, the image is split into horizontal slices consisting of 15 pixel lines. The number of slices is again decisive for the number of data points.

For each slice, the intensity along the fringe direction is averaged to I_0. Subsequently, the intensity distribution is fitted by the model function

$$I(x) = I_0 \cdot \left(1 + K \cdot \cos\left(\frac{2\pi x}{s} + \Phi_0\right)\right) \cdot \mathrm{sinc}^2\left(\frac{2\pi x}{s_1} + \Phi_1\right) \quad . \tag{5.9}$$

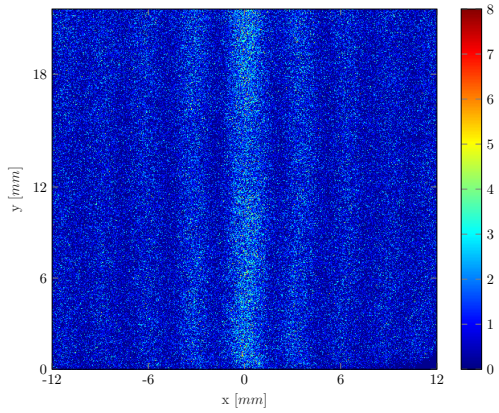

(a) $U_f = -0.45\,\mathrm{V}$.

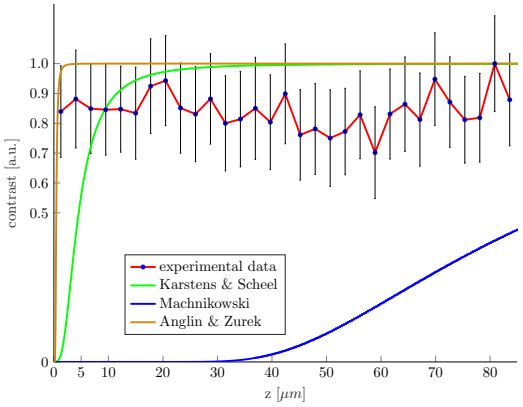

(b) $\Delta x = 5.86\,\mu\mathrm{m}$.

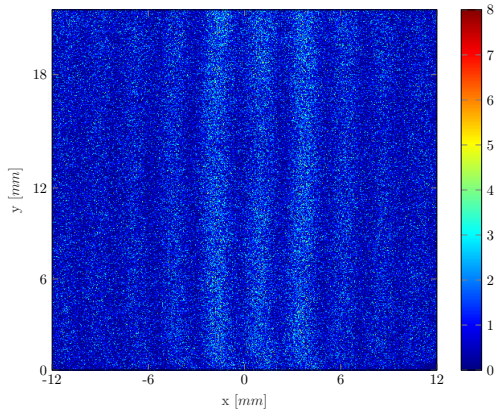

(c) $U_f = -0.51\,\mathrm{V}$.

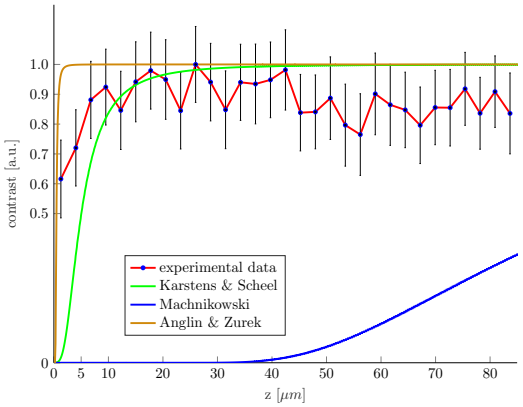

(d) $\Delta x = 6.54\,\mu\mathrm{m}$.

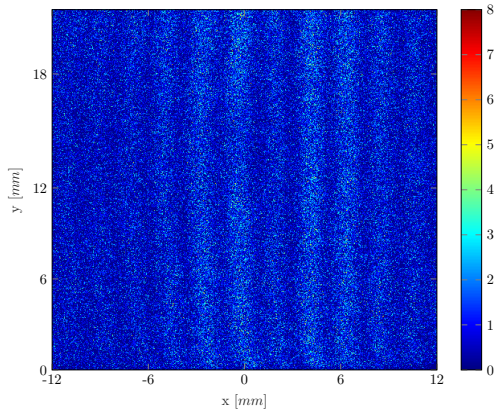

(e) $U_f = -0.56\,\mathrm{V}$.

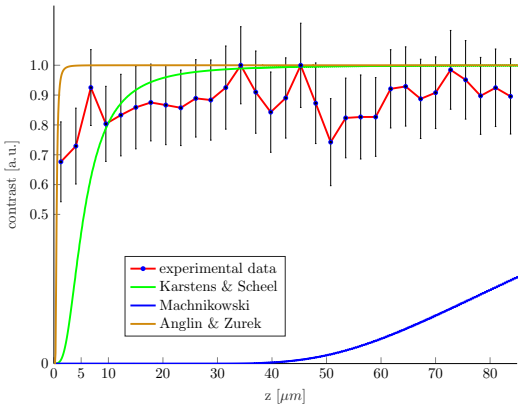

(f) $\Delta x = 7.23\,\mu\mathrm{m}$.

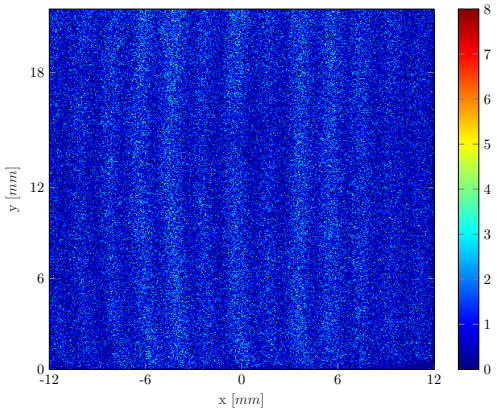

(g) $U_f = -0.62\,\mathrm{V}$.

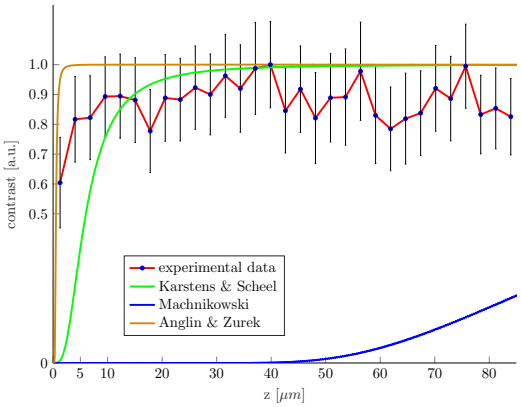

(h) $\Delta x = 7.92\,\mu\mathrm{m}$.

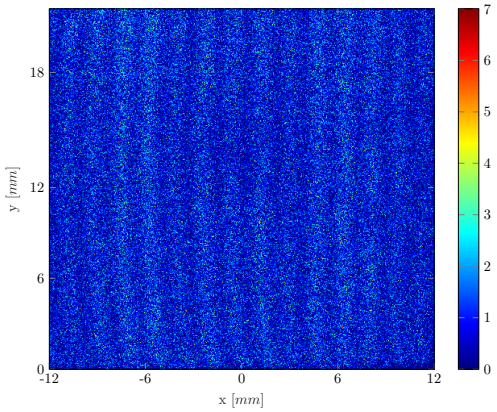

(i) $U_f = -0.67\,\mathrm{V}$.

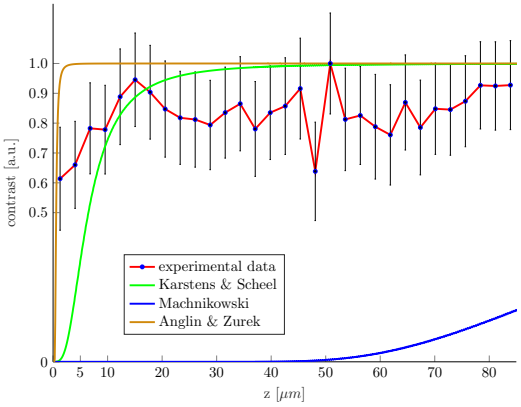

(j) $\Delta x = 8.60\,\mu\mathrm{m}$.

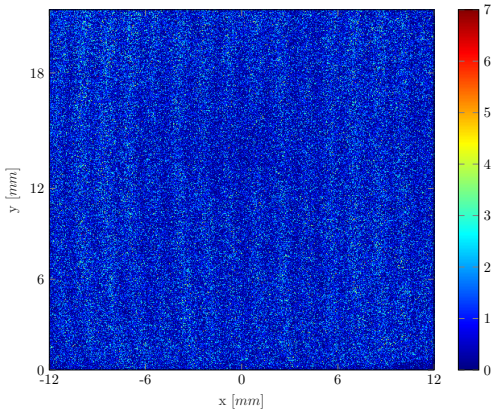

(k) $U_f = -0.73\,\mathrm{V}$.

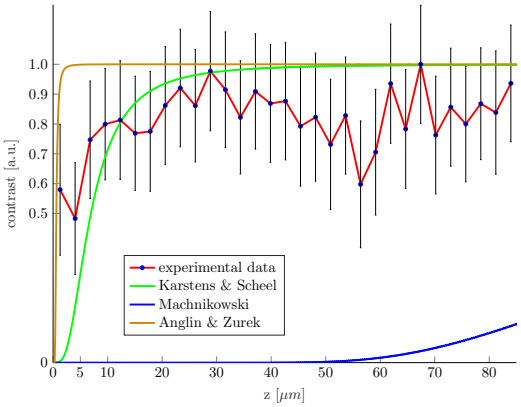

(l) $\Delta x = 9.29\,\mu\mathrm{m}$.

Figure 5.10: Measurement series of the fringe contrast for different biprism voltages U_f in order to vary the beam path separation close to a gold surface. On the left side the recorded image from the detector is shown where the plate surface is at $y = 0\,\mathrm{mm}$. The graphs on the right side illustrate the corresponding contrast of the fringes depending on the height z. Here, 1 mm on the screen correlates to $3.7\,\mu\mathrm{m}$ in vertical direction. Every data point is determined by a numerical fit of the averaged intensity distribution of 15 lines. The error bars result directly from the fit. For comparison the theoretical curves of [99, 100, 69] are plotted, too.

Due to the similarity to the double-slit experiment analysis, a *sinc*-function envelopes the distribution. The phases Φ_0, Φ_1, the fringe distance s and the width s_1 of the *sinc*-function have to be set manually as fitting parameters in order to achieve the best possible fit result. However, not every fit shows a good agreement with the experimental data regardless of the used parameters. That is due to peak fluctuations and imperfect periodicities. Thus, for every slice an error of K is yielded. The error bars in Fig. 5.10 are symmetric around the fit value.

Every image slice is optimized concerning the contrast K which is associated with a specific height. Finally, a graph is obtained with all contrast values plotted against its corresponding height values. The z-axis has to be rescaled taking into the account the vertical magnification of section 5.3.3. Here, a vertical length of 1 mm on the detector screen is equivalent to 3.7 μm over the plate.

The analysis of the contrast K as a function of the height z in all images of Fig. 5.10 shows that no significant decoherence process of free electrons interacting with a gold surface is observable. All data points are at least at 50 % of the maximal contrast value which is set to unity in each graph.

Fig. 5.10b exhibits a nearly constant run of the curve. In Fig. 5.10d, 5.10f and 5.10h there is only a slight drop of the contrast near the surface. This may be due to decoherence but other influences such as edge effects of the plate rim and a blurred borderline cannot be excluded. Fig. 5.10j and 5.10l even offer an extraordinary fall of the curve at $z \approx 50\,\mu$m that is probably due to inhomogeneities in the detection efficiency.

In summary, it can be stated that with the rather limited beam separation and contrast measurement accuracy of the current setup, a decoherence effect is implied but cannot be verified without doubt. This experimental result comes for every careful executed measurement series which was performed with the described interferometer.

For comparison all three theoretical approaches of section 2.2 are plotted in Fig. 5.10. Thereby, Machnikowski's [99] and Anglin & Zurek's [98] treatments seem not to describe well the observed behaviour of free electrons interacting with a gold surface. The height scale where the quantum-classical transition takes place deviates for both completely. Machnikowski predicts the effect on considerably higher z, merely the tail of the blue curve can be seen in the graph. His theory can therefore be clearly precluded by our experimental data. On the other hand Anglin & Zurek calculate a too weak effect where the transition is in the sub-μm range. This is simply due to the direct dependency of the rather high conductance of gold in Eq. (2.42).

At first glance the theory of Karstens & Scheel [100, 69] tend to be most promising in its predictions for the present measurement series. The order of magnitude of the transition is realistic and most of the error bars overlap with the green curve. However, no accurate and highly resolved data near the plate is available and thus, the first few data points are obviously too high. Especially the region between $z = 0 - 20\,\mu$m is not sufficiently covered and illustrated. However, it needs to be noted that the exact position of the surface can also only determined with an error shifting the experimental data and theoretical calculations along the z-direction.

Unfortunately, when the measurement series was recorded the experimental circumstances did not allow any further magnification of the relevant region with an adequate

count rate and without changing the emission properties of the tip. Also, desirably greater beam path separations were not possible to achieve. A higher biprism voltage requires a higher magnification to resolve the decreasing fringe distances. However, a further drop of the count rate combined with increasing demands to the stability of the electronic supplies could not be compensated.

Moreover, a number of only $3 \cdot 10^5$ recorded particles in each measurement does not allow a proper $g^{(2)}$- analysis of dephasing effects for each 15-line horizontal section separately. The integration time of each measurement was at approximately 25 minutes. Thereby, the stress to the tip and a potential change is hard to estimate.

5.4.2 Variation of the incident angle

A mandatory requirement for measuring decoherence effects is a parallel beam trajectory above the gold plate. Only then, the partial waves keep a constant distance to the surface and the decoherence effect becomes highly intense. In addition, all theoretical treatments are only valid for a parallel beam.

The vertical aligned electrodes of the deflector elements allow to manipulate the height and the angle of the beam with respect to the plate surface. By combining several deflectors in series, a "beam walk" can be executed by analogy with optical lasers and mirrors. Basically, a double deflector before and after the gold plate enables the optimization of the beam trajectory with regard to a parallel traverse. As can be seen in Fig. 5.11, an angular incident wave package at the entrance of the setup is aligned by a combination of deflector elements such that the region of the gold plate is crossed in constant distance.

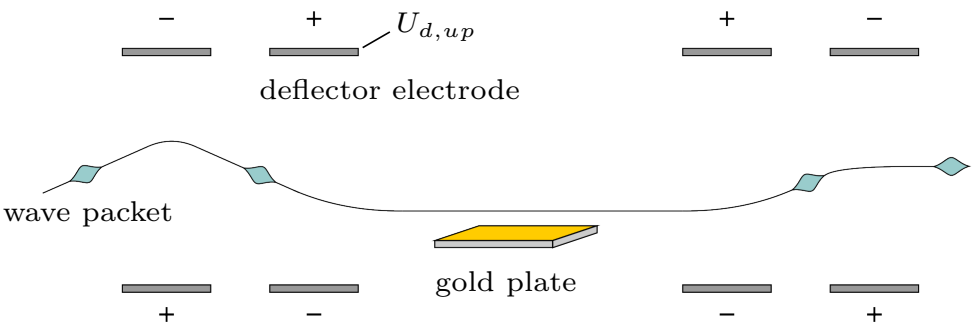

Figure 5.11: Schematic sketch of a possible beam path before and after the plate (not to scale). An angular incident wave package is aligned parallel to the plate surface by using a combination of deflector elements.

However, during experimental work it remains unclear in the first instance if the parallelism is achieved and how it can be verified.

One possibility is to pay attention to dust particles on the surface which become electrostatically charged when hit by the electrons. Even with greatest care, the presence of dust can not completely avoided which, in principle, is very unwanted. In [67] it is taken advantage of this effect for a silicon plate. While the voltage of the deflector

adjusting the angle before the plate is varied, the changing contour of the plate rim is observed which allows to draw useful conclusions.

But due to a considerable better conductivity of the gold surface, this effect turns out to be less distinctive and thus, it is more difficult to rate the current viewing angle of the plate during experimental alignment. Charges flow off quickly.

Therefore, a second method is applied in order to provide a cross check. The idea is to analyze the number of counts in the vicinity of the plate. If the surface is not orientated parallel to the beam, the latter impacts with a certain angle and releases both, backscattered and secondary electrons. Both contributions increase the detected intensity which is observed on the screen as a bright line. On the other hand, if the beam hits the plate from below its surface level, details of the coating and irregularities in thickness become more visible. Dark jagged areas near the surface appear and the boundary line of the plate smears out. Here, the summarized number of counts in these lines should be lowered.

In order to calculate the distribution of the number of counts for a given image, the plate position is determined as described in section 5.3.3 firstly. Starting from there, the residual recorded image is split into a selectable number of lines in which all contained counts are summed up. The number of counts for a certain quantity of lines is plotted against their height z. An example is shown in the measurement series of Fig. 5.12.

For a non-parallel beam, it is expected that some lines exhibit additional electrons or a lack of them and thus, a higher or lower number of detected counts. Thereby, the number of lines which are summarized determines the number of data points.

In the measurement series of Fig. 5.12 the beam path separation is kept constant with $5.58\,\mu$m but the angle of the incoming electron beam is varied. It is achieved by applying different voltages $U_{d,up}$ to the upper deflector electrode before the gold plate, as denoted for the images on the left side. The value ranges from $+12\,$V to $-12\,$V compared to ground.

The analysis of the contrast for each deflector configuration is carried out in the same way that is described in section 5.4.1. Again, no evident predication can be made whether there is a decoherence effect observable. The curve progression in all pictures is similar to the ones of Fig. 5.10.

However, the graphs on the right side of Fig. 5.12 offer a clear trend. Starting with 5.12b, where the beam is attracted strongly towards the upper deflector electrode, the first data points up to $z = 10\,\mu$m are of interest and become modified with decreasing $U_{d,up}$. In Fig. 5.12b and 5.12d the number of counts is lowered in this region due to a segregated electron beam from below the plate. As the angle between beam and plate approach to zero, all the electrons reach the detector without being blocked or scattered, see Fig. 5.12f. Obviously, this is the situation where the beam traverses the plate in constant distance. Further decreasing of $U_{d,up}$ again causes a non-zero angle between beam and plate which results in backscattered and secondary electrons. This action can be seen in Fig. 5.12h, 5.12j, 5.12l and 5.12n with growing strength.

A raise of the number of counts for $z \geq 50\,\mu$m is also explained by the generation

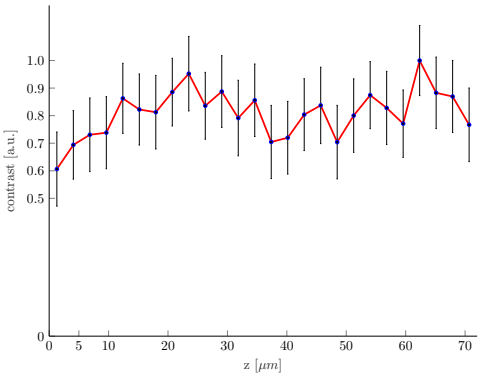

(a) $U_{d,up} = 12\,\mathrm{V}$.

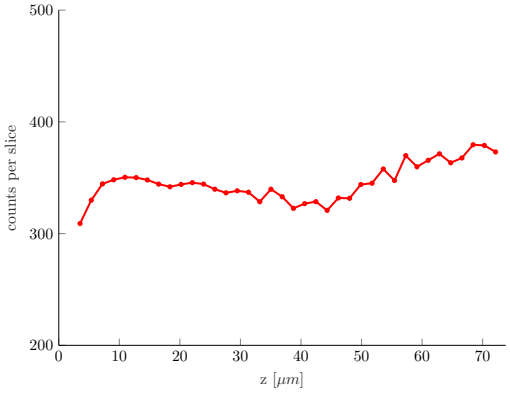

(b)

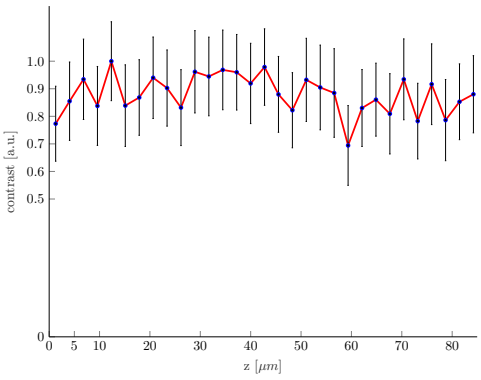

(c) $U_{d,up} = 8\,\mathrm{V}$.

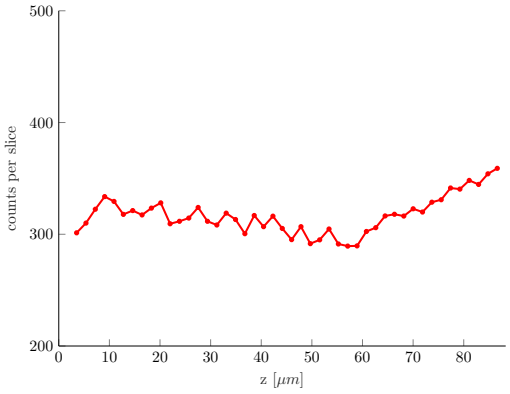

(d)

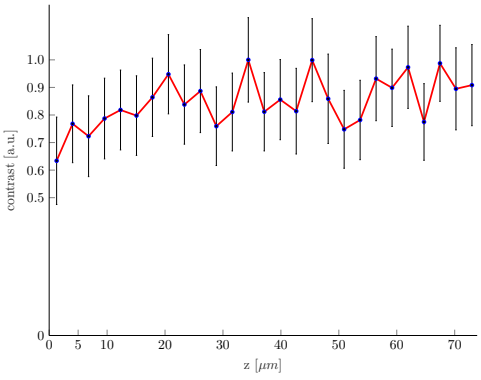

(e) $U_{d,up} = 4\,\mathrm{V}$.

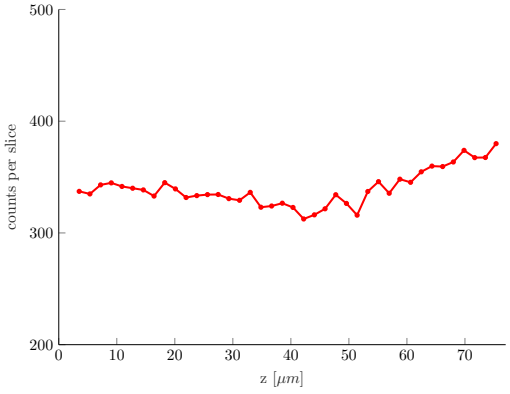

(f)

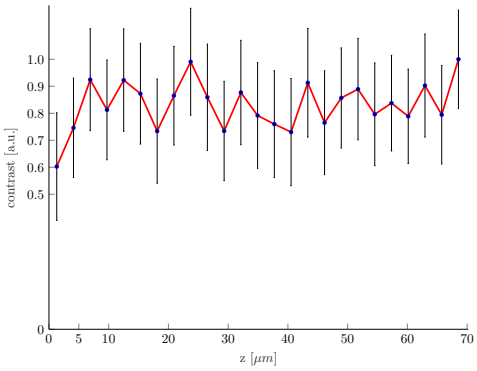

(g) $U_{d,up} = 0\,\mathrm{V}$.

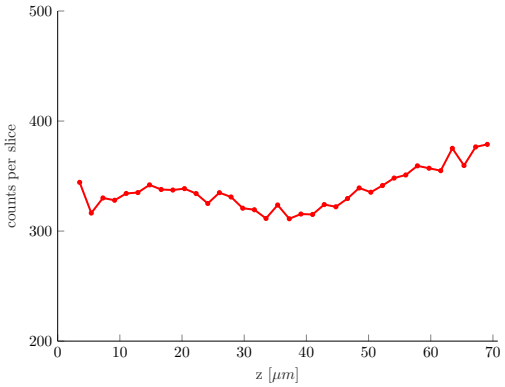

(h)

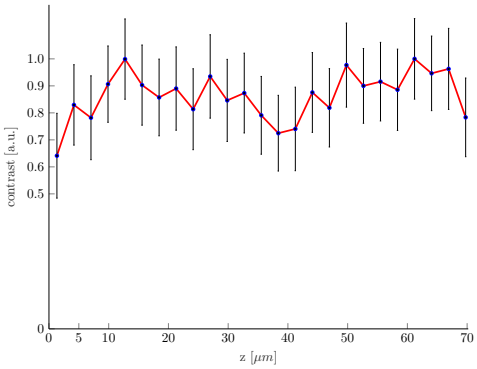

(i) $U_{d,up} = -4\,\mathrm{V}$.

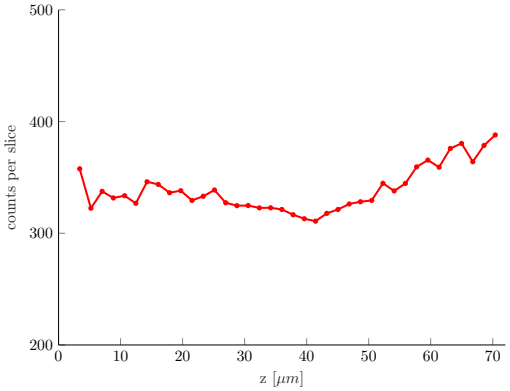

(j)

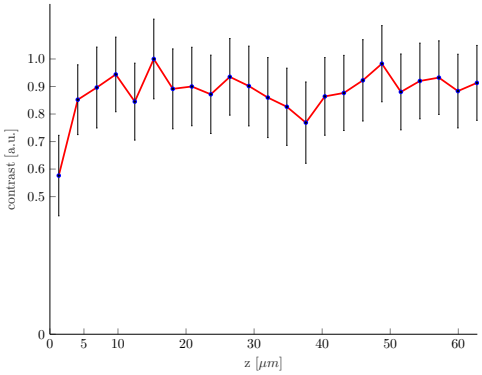

(k) $U_{d,up} = -8\,\mathrm{V}$.

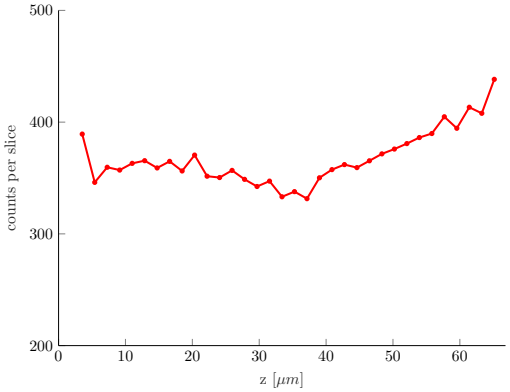

(l)

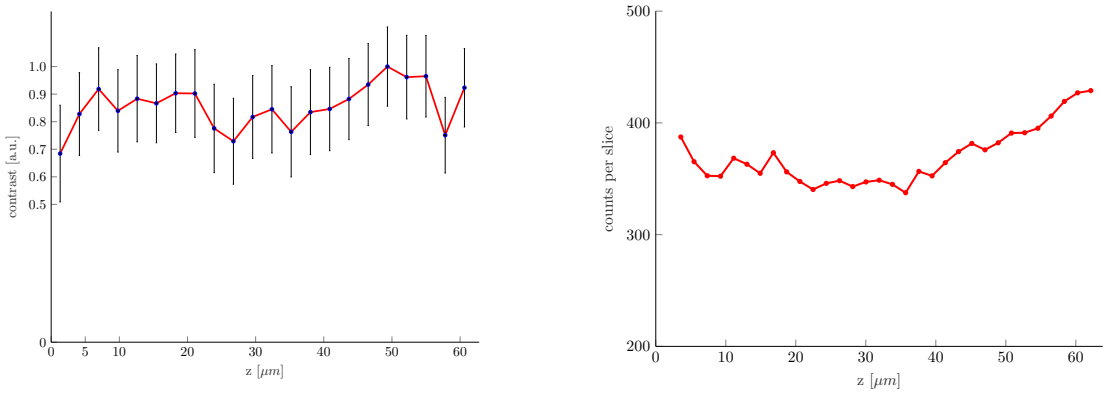

(m) $U_{d,up} = -12\,\mathrm{V}$. **(n)**

Figure 5.12: Measurement series of the fringe contrast for different voltages $U_{d,up}$ of the upper deflector electrode right before the gold plate. Thus, the angle between the electron beam and the plate surface is varied. On the left side the graphs of the contrast analysis are shown. Every data point is achieved by fitting the intensity distribution over 15 lines. The error bars directly result from the fit. The corresponding graphs on the right side illustrate the number of counts per (horizontal) slice. 10 lines are combined to a slice where the number of counts is averaged. These pictures allow to roughly estimate the degree of parallelism of the electron beam.

of stray electrons, namely at the edge of the aperture of the plate holding assembly. This is because the image section for analysis is chosen as large as possible and thus, cut out near the edge. In fact, there are two apertures with 2 mm diameter located at the entrance and exit of the plate assembly. With a length of 30 mm the angle between beam and plate is already limited to maximal 3.8 °.

The presented method allows to check the parallelism between the electron beam and the gold plate with good reliability. Thereby, the optimal configuration of the deflector element before the plate can be determined. However, this method can only be applied after the measurement is finished when the recordings and extensive analysis routine are finished. Nevertheless, it offers a new possibility to examine the parallelism in a more quantitative way which is used for posterior ongoing measurements. The measurement series of Fig. 5.10 is an example where the parameters are optimized by this method.

6 Planning of the operation of a cryostat

A next step in the study of decoherence is to expand the experimental setting to more decisive parameters. In principle, the mechanism of decoherence is besides geometric properties dependent on the concrete material properties as well as on the temperature and the electronic structure of the model system. The existing biprism interferometer is well suited for the swap of the material acting as the decoherence environment and for creating electron superposition states in general. With an additional implemented cryostat a wide temperature range of the plate can be tuned.

Here, a potential application of a cryostat system in the interferometer is planned and examined in order to study decoherence effects of electrons with a superconducting surface. Especially the fundamental question of the interaction between the beam electron superposition states and Cooper pairs shall be given.

6.1 Technical description of the cryostat

The cryostat *ST-400-2-NM Ultra High Vacuum Continuous Flow Cryostat System* is a commercial product of the company *Janis Research LLC, USA*. The decoherence plate is attached to a cold finger which can be run with either liquid nitrogen (LN) or liquid helium (LHe). Moreover, integrated coils made of phosphor bronze (an alloy of copper, tin and phosphorus) allow to heat the sample. This alloy is widely used in cryogenic physics since a good electrical conductivity is paired with a low thermal conductivity. Thus, low temperatures can be reached without adding too much heat into the system. The total temperature range of the cryostat is specified between 2 K and 500 K.

The LN or LHe is continuously guided through a highly insulated transfer line to a copper sample mount where the decoherence plate is fixed. Thereby, the flow of the cryogens is regulated with a needle valve in the transfer line.

The cryostat system is basically equipped with the following components:

- The **sample mount** is at the end of the cold finger. It is a gold-plated copper base where the sample, e.g. the decoherence plate is mounted. For that purpose, four M3 tapped holes are provided. The sample mount has an integrated heater and thermometer to control the temperature of the sample. Heating coils and thermometer are not in the UHV.

- The **radiation shield** is a cylinder surrounding the sample mount and a long region of the transfer line within the UHV. The upper end is fixed to a thermal anchor on the stainless steel section of the cold finger. Again, it is made of gold-plated copper. The shield ensures to yield low temperatures by intercepting room

temperature radiation and reducing heat load on the sample. Since we want to lead electrons nearby the decoherence plate, the shield has to be provided with two conical holes in beam direction. Probably, this will increase the minimal achievable temperature at the sample but should still be sufficient for using niobium with a critical temperature of $T_C = 9.2\,\mathrm{K}$. It should be noted that this critical temperature is valid for atmospheric pressure. However, niobium does not show a strong dependence on pressure, neither for vacuum nor for the GPa range [181].

- A highly insulated **transfer line** guides the cryogenic liquid from the storage dewar to the sample mount. Both, a vacuum insulation and a multilayer material insulation make sure that minimal cryogenic losses occur. The coarse vacuum in the line can be established easily with a rotary vane pump connected to an evacuation valve. Furthermore, the cryogenic flow within the line is regulated by a needle valve in order to set together with the heating filament any arbitrary temperature at the sample. The transfer line includes a flexible section of 183 cm and a 122 cm long storage dewar leg. A 90 degree elbow on the cryostat leg is customized to our laboratory dimensions.

- Two **electrical feedthroughs** are allocated on CF40 flanges on the cryostat body. A standard 8 pin feedthrough allows to control the internal heater and thermometer wiring and a 6 pin UHV feedthrough leads directly to the sample mount in the UHV. However, this UHV pin stays idle in our application.

- A **temperature controller** of the company *Lake Shore* offers two sensor inputs with PID control loops. This feedback mechanism calculates the difference between a desired control temperature and the measured temperature by means of a 24 bit A/D converter. A control function either in proportional, integral or derivative terms is applied for correction. The computer communication is executed via a parallel general purpose interface bus (GPIB) system employing sixteen signal lines. Thus, the desired temperature is maintained by applying power to the control heater.

In Fig. 6.1 the cryostat system is depicted. It is mounted on the vacuum chamber by a rotatable CF40 flange. The radiation shield and the sample mount are then located in the UHV. The UHV feedthrough is also mounted on a CF40 flange whereas the temperature control only requires KF (Klein Flange) connection since it is only in the helium transfer tube but not in the UHV environment. The sample on the cold finger can be accessed by removing the radiation shield. Once the upper M3 screws of the anchor are loosened, the shield can be carefully slid off the anchor. Scratches on the gold plated surface of the shield should be avoided to ensure a good shielding performance. For the mount of the gold plate, four tapped holes at the bottom of the cold finger are provided. Two holders were designed in order to establish a good thermal contact of the plate while leaving two sides of the plate blank. Above those two blank sides, the electron beam can cross without an obstacle. In Fig. 6.2 a more detailed look on the sample mount is shown. The transit of the electrons through the shield is provided via two conical apertures with only 1 mm diameter. Regarding to secondary electrons, a conical shape is beneficial. Moreover, small holes minimize the thermal load on the

plate and allow only for a maximal inclination of 2 ° of the beam with respect to the plate.

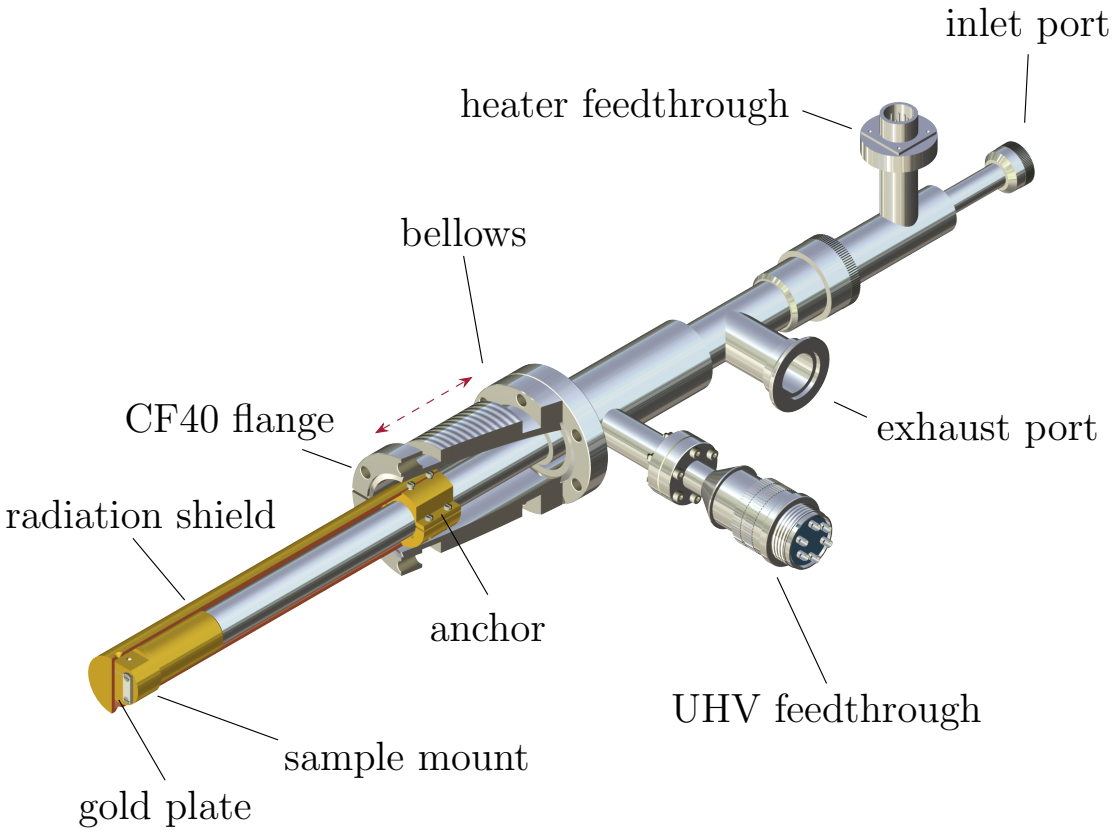

Figure 6.1: Drawing of the continuous flow cryostat system. LHe or LN enters the cryostat through the inlet port where the transfer line is inserted and a snug connection is built. The fluid reaches the sample mount region and eventually cools down our fixed decoherence plate at the bottom. For a faster and more efficient cooling, a mechanical vacuum pump can be attached to the exhaust port. The radiation shield encompasses the whole cold finger. It is mounted by an anchor. In order to move the plate vertically, a bellows is placed between chamber and cryostat flange which allows for an accurate position adjustment in the micrometer range.

In order to move the plate vertically into the beam path of the electrons, a bellows with two CF40 flanges is placed between the vacuum chamber and the cryostat. This bellows is driven automatically by a motorized linear actuator with 100 mm of travel. The actuator is powered by an electronic unit including a stepper motor and its controller with a digital readout option with 12.7 μm resolution. A RS-422/485 communication with the computer is available to adjust any desired position of the plate. This is a big advantage compared to the micrometer screw combined with the wedge of the plate assembly since lost motion and non-linear shifts are avoided. However, particular care has to be taken to not bounce with the radiation shield on the metallic interferometer bench when placing the gold plate in the optical axis. This will be a great challenge as there is no visible access while doing that. Both, simulations with a 3D computer-aided

design (CAD) software were performed and precise measurements of the chamber and part dimensions were taken in order to estimate the critical position of the bellows. Assuming the surface of the gold plate is 3 mm distant from the floor of the radiation shield (adjustable via the anchor), there is only 1.8 mm vertical space between the radiation shield and the metallic interferometer bench. The outside diameter of the shield is 33 mm which is bigger than the gap of the interferometer bench. Another issue is the precise position of the interferometer in the horizontal plane. Since the cryostat position is specified by the flange on the chamber top side and only vertical movement is possible, the interferometer must be positioned in the chamber with high accurateness. Moreover, the interferometer position must be the same after every demounting and opening of the chamber, e.g. for replacing the emitter.

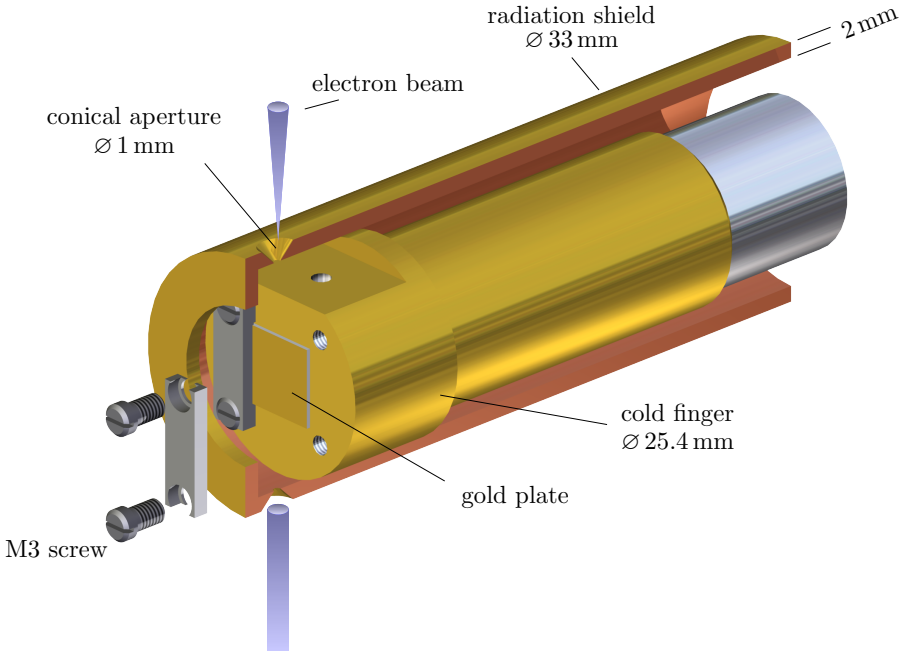

Figure 6.2: Closer look on the cold finger of the cryostat. The gold plate is mounted by two holders with M3 screws. Due to its tight contact and the surrounding radiation shield, the plate is expected to reach low temperatures of a few Kelvin. The electrons traverse parallel to the gold plate through two conical apertures of only 1 mm diameter. Thus, the angle of the beam with respect to the plate can not exceed 2 °.

Therefore, two pedestals were designed in which the interferometer bench is fixed with four protruding grub screws. The cross section is a circular segment and fits the inner diameter of the Mu-metal shielding of 78 mm. Fig. 6.3 shows a sectional view of the most relevant parts for positioning the interferometer. The interferometer bench is fixed to the pedestal by two M3 grub screws on the left and right side of the bottom plate which are dimpled in the pedestal and bear on the Mu-metal shield surface. Since the bench has a slight torsion in length direction, the grub screws are used to achieve

an upright position. The Mu-metal shield is kept centered by three M3 screws from a holding ring. This ring in turn is tightly connected to the inside of the vacuum chamber by three M4 screws. Fig. 6.3 is a view from behind but looks in principle the same from the other direction. For simplification, no interferometer parts clamped on the two ceramic rods are shown. The holding ring is not continuous along the bench length of 450 mm but only placed at both sides. Of course, the Mu-metal shield is continuous but has to be modified in order to mount the pedestals and to guide through the radiation shield of the cryostat. It is tried to keep the holes as small as possible to avoid a significant loss of shielding. Therefore, two M2 tapped holes at both sides and one hole with 35 mm diameter right in the middle of the Mu-metal shield are drilled.

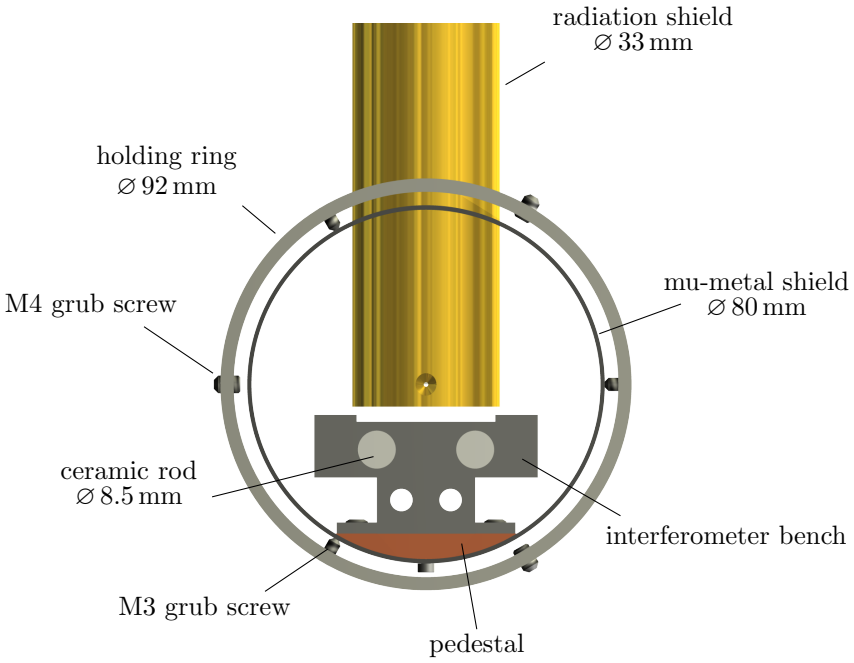

Figure 6.3: Cross section of the interferometer bench and surrounding parts. With two grub screws on the left and right side of the bottom plate, the interferometer bench is fixed to the pedestal (red area) and they allow to correct a possible torsion of the bench. The pedestal is mounted to the Mu-metal shield by a screw at the bottom. This shield in turn is connected to the chamber (not shown) by a holding ring. Three M3 screws keep the Mu-metal shield in a centered position and three M4 screws form a tight connection to the chamber.

However, compared to other commercial cryostat systems the active diameter of the cold finger of 25.4 mm is rather small and thus well suited for our application. Furthermore, by implementing solely nonmagnetic materials in the vicinity of the cold finger no magnetic disturbance of the electron beam will occur.

For a further research of decoherence effects near surfaces, the following plate materials and their properties seem to be interesting candidates:

- **Niobium** is a soft and ductile transition metal. It is one of three elemental type-II superconductors forming magnetic vortices above a certain critical field strength due to energetic considerations. The MEISSNER effect is therefore not exhibited completely. As described earlier, the critical temperature is $T_C = 9.2\,\mathrm{K}$ for atmospheric pressure but does not vary too much in vacuum [181]. Because of that a decoherence plate coated with niobium is well suited to implement it into the cryostat and run it with LHe to achieve superconductivity. Since previous decoherence effects base on the COULOMB interaction between beam electron and electron gas of the material, a deeply interesting new situation will occur when Cooper pairs come into play. Will the interaction be similar or will a new effect arise? And how to deal with a zero electric resistivity? For the fabrication of niobium surfaces, a high vacuum coating plant in the local affiliation and lots of experience is available. However, the critical temperature of niobium strongly depends on the purity of the metal. Great care in the fabrication process is therefore essential.

  In addition, the resistivity for normal conducting niobium is $\rho = 1.52 \cdot 10^{-7}\,\Omega\mathrm{m}$ for room temperature and lies between gold ($\rho = 2.2 \cdot 10^{-8}\,\Omega\mathrm{m}$) and p-doped silicon ($\rho = 1.5 \cdot 10^{-2}\,\Omega\mathrm{m}$). As a metal, niobium shows a linear dependence of the resistivity with respect to the temperature [182]. It is therefore preferable to study decoherence effects with a niobium surface over a wide temperature range. Thus, the resistivity is tuned and comparisons to earlier results can be made [66].

- **Yttrium barium copper oxide (YBCO)** is a famous representative of high-temperature superconductors [183]. With a specific crystalline arrangement of copper and oxygen (perovskite structure consisting of layers), this cuprate reveals astonishing characteristics like a critical temperature of $T_C = 92\,\mathrm{K}$. Therefore, it is possible to cool down YBCO to the superconducting phase with only liquid nitrogen. Not only the high T_C is a surprising feature which cannot be explained by the microscopic BCS theory [184], but also the fact that YBCO is a ceramic compound and not a metallic conductor. However, YBCO has a rather low resistivity in the normal conducting phase of $\rho \approx 10^{-5}\,\Omega\mathrm{m}$ for room temperature and shows again a linear curve progression within the operating range of our cryostat [185].

  The fabrication process and its accompanying properties of YBCO is well documented in literature. In our department it is possible to manufacture a YBCO layer of 100 nm thickness on a strontium titanate substrate (STO). For already 20 nm layer thickness, good superconducting properties become apparent [186]. However, the surface roughness of approximately 10 nm is slightly worse than for the gold coating on a piece of silicon wafer. Furthermore, it is known that heating of the YBCO layer with 150 °C for weeks leads to oxygen diffusion of the material and lowers the critical temperature [186]. As we need a bake-out of the chamber for a few days in order to reach an optimal pressure, it has to be checked if the superconducting material will resist this thermal strain. As for niobium, the purity of the YBCO surface is also decisive to ensure superconductivity with liquid nitrogen.

- An interesting candidate for testing decoherence properties over a wide resistivity range of the plate seems to be **vanadium dioxide**. VO_2 is a dark solid compound which appears in different configurations. At around 65 °C a reorganization of the crystalline structure takes place. Below and above this point, the electric and optical properties vary strongly [187]. The oxide is therefore suited for a wide variety of applications involving thermally activated electronic or optical switching devices [188]. A detailed examination of nanowires of VO_2 offered that the metal-insulator transition is accompanied by a triple point with one metallic phase and two insulating phases [189]. The metallic phase is entered within picoseconds when increasing the temperature above the triple point. By chance reference [190] describes some measurements which perfectly fit to our setup. A sample which is also square in shape with $d = 95\,\text{nm}$ is tested with various sweep rates of the temperature around the triple point. A hysteresis loop is recorded for increasing and decreasing temperatures. Importantly, the sheet resistance ($\rho_\square = \rho/d$) drops from $\rho_\square \approx 10^6\,\Omega$ at 25 °C to $\rho_\square < 10^3\,\Omega$ at 90 °C which is a difference of more than three orders of magnitude. The sweep rate of the temperature has no significant influence on this result.

  With our cryostat system, this massive resistance change is therefore easily to achieve. However, a Si/SiO_2 substrate is used in combination with pulsed laser deposition of the vanadium dioxide at $\approx 600\,°C$ [190]. The physical outcome of this process is similar to thermal evaporation which relinquishes to laser beams and can be executed in our facilities. Nevertheless, a cheaper and more efficient process for vast areas is preferably desired. A broad overview of fabrication methods is presented in [191]. The choice of preference is again magnetron sputtering as it is used for coating the biprism fiber with gold-palladium. Sputtering is the most common physical vapour deposition process for growing thin films of VO_2. The advantages like film uniformity, scalability to larger substrates and deposition efficiency are quite obvious. An argon ion discharge is trapped by a permanent magnet to enhance the ion bombardment on the vanadium target. The sputter rate in an argon-oxygen atmosphere is increased. Many studies were taken to standardize the influence of the process parameters (temperature, oxygen partial pressure, plasma ratio of oxygen and argon, voltage at the target) with respect to the thin film [192, 193].

The interaction between a moving charge in the vicinity of a surface in the superconducting phase is an open question in general. There are three crucial properties for a superconductor. Not only the critical temperature T_C, but also a critical magnetic field B_C and a critical current density $\vec{j}_C$ influence the stability of the superconducting phase. All of them are in direct link to each other [194], see Fig. 6.4. For example, the empiric finding $B_C \propto (1 - T/T_C)^2$ states that with increasing magnetic field the critical temperature T_C decreases.

A first theoretical description of superconductivity was given by the brothers London in 1935 when they proposed a frictionless motion of a superconducting electron

density n_s in terms of the time derivative of the current density [195]:

$$\frac{\partial \vec{j}}{\partial t} = \frac{n_s q^2}{m} \vec{E} \quad . \tag{6.1}$$

In principle, it is a variation of OHM's law. By taking the curl of Eq. (6.1) and using MAXWELL equations, a characteristic length turns out. This LONDON penetration depth is calculated to $\lambda_L = \sqrt{m/\mu_0 n_s q^2}$. A differential equation

$$\nabla^2 \vec{B} = \frac{1}{\lambda_L^2} \vec{B} \tag{6.2}$$

can be obtained which describes an exponential decay of the magnetic field in the superconductor in the order of λ_L. The experimental observed MEISSNER effect is therefore well explained. Moreover, a further result is that shielding currents arise in a thin layer near the surface in order to expel the magnetic field. Thus, a critical field B_c will exist since the superconducting state cannot maintain arbitrary high currents. It is proportional to the penetration depth and the critical current density, $B_c \propto \lambda_L \, j_c$.

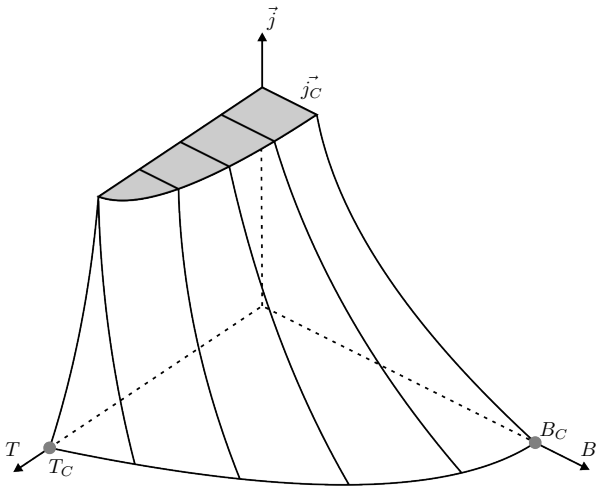

Figure 6.4: Qualitative limits of the critical properties temperature, magnetic field and current density of a superconductor. Within the three-dimensional space the superconducting phase prevails.

In order to understand the decoherence mechanism between an electron and a superconductor, it is indispensable to describe the electromagnetic interaction of the electron and the superconductor firstly. However, this probably is a difficult undertaking as the analytical description of the interaction between the induced field of the electron and the supercurrents near the surface becomes complicated. Usually in classical electromagnetism, a given charge distribution $\rho(\vec{r})$ is used to calculate the electric potential $\Phi(\vec{r})$ with respect to boundary value conditions. Here, the POISSON equation $\Delta\Phi(\vec{r}) = -\frac{1}{\varepsilon_0} \cdot \rho(\vec{r})$ must be solved appropriately.

In a superconducting state there is an attractive interaction between electrons on the FERMI surface which leads to the formation of Cooper pairs trough the exchange

of phonons. Within the framework of the widely accepted BCS-theory, these Cooper pairs, consisting of two electrons with opposite momentum and spin, are responsible for many electronic properties of the superconductor [184]. Yet, the application of the POISSON equation on Cooper pairs in the superconducting material is not clear. The issue of the interaction between electron waves and Cooper pairs is of great relevance and is crucial for the decoherence measurement of electrons near a superconducting surface. To my knowledge, there is neither a theoretical nor an experimental work on the question of how the superconducting state is influenced by a free moving charge or an arbitrary electric field.

Hereby, many facts will play a role: the critical current and magnetic field is extremely dependent on the crystal orientation of the superconductor. The angle of propagation is relevant. Also, deformations of the crystal lattice have significant influence on the critical properties and hence the interaction. The choice of the substrate is thereby important. Those properties and features have to be determined experimentally at the particular workpiece. Furthermore, it remains unclear if the moving electron interacts only with the Cooper pairs or the normal conducting electrons in the superconductor. The LONDON equations describe the electrodynamic of a superconductor neglecting the normal conducting component completely. For slow varying currents in time this is justified, but for fast varying currents the normal conducting electrons become accelerated and produce losses by scattering. For that reason, a superconductor can carry only dc currents without loss. Ac currents experience a resistance.

Assuming a typical electron count rate at the detector of $10^6\,\mathrm{Hz}$ and a velocity of $1.88 \cdot 10^7\,\mathrm{ms}^{-1}$ when applying an emission voltage of 1000 V. Thus, the electrons need $5.3 \cdot 10^{-8}\,\mathrm{s}$ to traverse the one meter long chamber. That means that in average only 0.053 electrons are in the interferometer at the same time. Even by taking into account that the field emission is a POISSON process with time distances between consecutive electrons in the μs range [196, 3], one can reliably presume having only one single electron near the superconductor at a given time.

From the view of the superconductor a magnetic field is formed according to the LORENTZ transformation of electric and magnetic fields [197, 198] which may disturb the superconducting phase and has to be considered for precise estimations of the interaction between the beam electron and the superconductor. In [199] the magnetic field is derived by transforming from the static electric field of the point charge's rest frame into a relatively moving frame. Due to its shape the magnetic field passes rapidly the surface with steep rising and falling edges. However, the specific field distribution of the moving electron is not simply spherical as one might expect. In principle this is a consequence of the hairy ball theorem which states that a tangential vector field on a spherical shell must vanquish at least at one point [200]. Because of symmetry considerations this instance is valid for the tangential component of a magnetic field on all points of the surface. Only a constant radial component remains. If it is non-zero then it must be a magnetic monopole which is forbidden by the MAXWELL equations. In other words:

$$\int_S \mathrm{d}^3 r\, \nabla \vec{B} = 0 = \int_{\partial S} \mathrm{d}^2 r\, \vec{B} = 4\pi r_S^2 \cdot \mathrm{radial}(B) \quad . \tag{6.3}$$

Since the magnetic field of a moving charge does not vanish, it cannot be spherically

symmetric. Moreover, the ac-effect in a superconducting material has desirably to be analyzed theoretically.

In literature, there are values for the critical field B_C and the penetration depth λ_L but must be treated with some reservation as every experimental situation is different. It is for niobium $B_C \approx 200\,\mathrm{mT}$ and $\lambda_L \approx 40\,\mathrm{nm}$, for YBCO $B_C \approx 160\,\mathrm{mT}$ and $\lambda_L \approx 140\,\mathrm{nm}$ [201]. The situation becomes even more complicated for thin films of thickness d when $\lambda_L \geq d$. Then, the critical field and current have to be modified to [194]

$$B_{C,d} = 2\sqrt{6} B_C \frac{\lambda_L}{d} \quad , \tag{6.4}$$

$$j_{C,d} = \frac{\sqrt{2}}{12\pi\sqrt{3}} \frac{cB_C}{\lambda_L} \quad . \tag{6.5}$$

Also, the Meissner effect has to be considered since the moving electrons induce a magnetic field which has to be shielded by supercurrents from the surface. It is then interesting to see whether these currents move along with the beam electrons and generate hence a which-path-information. In contrast to a normal conductor, the interaction of the electrons with the supercurrents may lead to a deflection of the electron trajectory. Moreover, since the critical current of the superconductor depends on temperature and magnetic field and is maximal for $T = 0$ and $B = 0$, a significant change of the electron count rate of the single-atom tip is possibly able to cause the transition between normal and superconducting phase when the temperature is kept near T_C. Either by exceeding the critical current or the critical temperature, the transition probably leads to a spontaneous change of the contrast of the interference pattern.

7 Conclusion and outlook

Single-particle interferometers offer a wide range of applications due to their high phase sensitivity and versatile operation possibilities. A long historical development culminated for example in the detection of black holes [40], separated Bose-Einstein condensates on an atom chip [202], tests of quantum information processes via neutrons [203] or interferometry with charged particles in general [24]. Hereby, biprism electron interferometers played an important role as trailblazers for plenty of scientific activities [204]. The presented thesis largely conforms with the canon of prosperous experiments towards state of the art hybrid quantum systems, where the precise understanding of the classical-quantum border is essential, and promising applications in the field of sensor technology [95, 205].

In order to embark this path, typical deficits in electron interferometry like unpredictable emission processes or ineffective detection methods had to be characterized and improved. Thereupon, the already existing interferometer setup was modified. Many parts were adopted and checked for their suitability. Existing procedures and mechanical handlings had to be called into question.

Particular attention was paid to the field emitter. It is the most crucial but at the same time the most fragile component of the interferometer. Here, the emission of coherent electrons takes place which is associated with substantial requirements to this dynamical process.

The implementation of a single-atom tip into the interferometer was synonymous with a drastic improvement of data acquisition. The brightness was increased notably compared to conventional cold field emitters. The reduction of the source size to only one emitting atom enhanced the spatial coherence of the electrons. Moreover, stability problems of former experiments, where the emission center changed from time to time [56], have been overcome due to energetic and formation reasons. An absolute fixed emission center of the SAT is advantageous for the adjustment of all experimental parameters and the recording of interferograms with high contrast. Furthermore, after several hours of working the tip condition can be regenerated with a simple heating procedure. In contrast to earlier experiments, the initial beam properties become reestablished reliably.

In this work it could be demonstrated that all beneficial features of a SAT become even more apparent in a biprism interferometer.

Thereby, it is made use of a well-known technique where the intensity of an electron source is increased. Two counter electrodes are placed in front of the SAT. While the SAT is biased with a negative polarity, the first counter electrode is set to a positive voltage and the second electrode is grounded. Besides a tunable and considerable

higher signal rate, the question of the preservation of the coherence had to be clarified. Due to acceleration and deceleration effects it remained unclear if the coherence of the electrons is lowered or even lost. However, by means of interferometric measurements it could be shown that this is not the case for the application of such an electron gun. The analysis of a measurement series regarding the interference pattern periodicity, number of fringes and interference contrast showed that the electron energy and the transversal coherence of the electrons are kept constant, independent of the applied voltage to the counter electrode. At the same time the intensity of the electron beam was increased by a factor of 6.4 similar to the FOWLER-NORDHEIM relation. On the basis of shifting wave packages with a Wien filter it was possible to evaluate the longitudinal coherence length to 82 nm. The corresponding energy width is an important value for field emitter and could be stated for our single-atom tips to 377 meV. Again, these values remain unchanged for different counter electrode voltages.

Moreover, the setup enabled the generation of slow coherent electrons with energies well below the extraction limit of the tip. The required energy for the conducting electrons of tungsten to tunnel into vacuum is then provided mostly from the counter electrode. With a counter electrode voltage of 1378 V the generation of 600 eV electrons succeeded combined with a reasonable count rate of 1138 Hz. These electrons built up an interference pattern with a contrast of 37.7 %. The energy of the free electrons always correspond to the tip potential. It was verified in this thesis by beam path simulations. Depending on the current tip status and on the experimental circumstances, there is no principle border for low-energy electron interferences in a biprism interferometer.

The presented electron gun design is of major relevance in all applications where intense beams of coherent or slow electrons are required. To name just a few, there are microwave chip-based designs [74], electron diffraction microscopy [108, 109, 157] and sensitive sensors for inertial forces [63]. Of course, the concept is also applicable to interferometers with ionized atoms [56, 24].

In a nutshell, the used electron gun design has three advantages for single-particle interferometry:

- The signal rate at the detector is increased and allows to adjust the beam trajectory more easily. In particular, it is helpful when the interference pattern is strongly magnified.

- The detection of a lot more particles is provided within a realistic integration time. On the other hand, for a desired number of recorded particles the integration time is lowered and the risk of a change of the tip shape during the measurement is decreased. Also, the accurateness of a potential correlation analysis is increased with an increasing number of hits.

- The gradual reduction of the electron energy for a given tip allows to increase the strength of interaction with the gold plate and the environment in general. Potential sensor applications become more sensitive.

Another important technical improvement regards the detection method.
Until the last two decades the usage of a phosphor screen was the primary choice to visualize charged particles in biprism interferometry. Followed by a camera system the images could be transferred to a computer. However, this procedure offered several drawbacks such as a lack of temporal information, damaged dark regions in the fluorescent layer, inability of long-term integration and a low resolution of the chip. According to practical considerations, the camera had to operate in absolute darkness which impeded an instantaneous adjustment of the electron beam largely.

With the purchase of a delayline detector entirely new opportunities opened up. The described problems with the phosphor screen ceased to exist and a direct detection method was established. In this thesis it could be pointed out that a delayline detector is well suited for the data acquisition of a biprism interferometer. Interference patterns with high contrast could be recorded with little expense due to a modern electronic readout and the comfortable storage in data files. Its time information is a mandatory tool for the development towards a sensor of electromagnetic perturbations.

In order to catch that goal a compact interferometer as a prototype was built and presented. This interferometer is limited in size to only 87 mm length. Interference fringes with a contrast up to 42.7 % could be achieved. The small dimensions and robustness are perfectly suited to act as a mobile device for detecting electromagnetic and vibrational perturbations. By using the spatial and temporal information of every particle impact it was possible to identify dephasing frequencies of 50 Hz and 150 Hz with spatial perturbation amplitudes around 14 nm.

These frequencies obviously result from the surrounding electric network in the laboratory. Thus, the compact interferometer is able to scout for disturbing influences in research facilities and other sensitive areas.

With regard to the future development of a reliable, versatile and highly efficient sensor, the idea of combining the compact interferometer assembly with the electron gun design seems to be very promising together with a higher detection sensitivity with slower electrons. Thus, the benefits of a simple construction and enhanced brightness of the tip unite. Moreover, this setup allows to use electrons with an arbitrary energy and enables a tunable susceptibility to external electromagnetic perturbations.

A further minimization of the sensing biprism interferometer can be achieved by mounting the electron source onto a micro positioning stage. The electron beam can be adjusted precisely to the optical axis and the deflectors become redundant. By shortening the distance between source and biprism fiber, the space between biprism and the interference plane can be reduced as well to keep the superposition angle constant. This ensures an even compacter arrangement.

Besides design optimization, the sensing device needs to be calibrated properly with respect to dephasing influences. This could be achieved by a perturbation source like a HERTZian electric dipole with defined strength and frequency that has to be implemented in the setup permanently.

Important steps towards a mobile sensor for electromagnetic and vibrational frequencies are described, but there is still room for improvements of the current setup.

A major focus of this thesis is on decoherence of superposition states of free electrons in the vicinity of a gold surface. The preferable task was to clarify open questions of this fundamental problem and to compare the results with new [100, 69] and earlier existing [98, 99] theories.

Therefore, the old setup of [67] was adopted and largely modified. In particular, it was taken advantage of the successful operation of the interferometer with the electron gun design, new biprism fabrication methods, the novel delayline detector and correlation analysis techniques.

The fabrication of a 50 nm thick gold layer on a silicon wafer substrate proceeded well with a surface roughness of $\approx 5\,\mathrm{nm}$ and could be implemented in the interferometer. Due to the extremely wide parameter space of all components, the initial time-consuming and difficult beam adjustment could be further refined and optimized. A reliable method to quantify the current height scale over the plate was demonstrated and applied. Also, the decisive beam path separation was derived by means of transfer matrices. Simulations with the software *Simion* supported this approach.

Finally, several different measurements series were recorded with promising and deliberately chosen settings. The evaluation for all of them revealed within natural tolerances the same result for the contrast in dependency of the height z. Thus, one exemplary measurement series for varying both, the beam path separation and the angle between plate and beam, were precisely examined and presented.

As a fundamental result, two theoretical treatments describing the decoherence of free electrons above a gold surface seem not to fit to our data. Due to the 6 orders of magnitude lower resistivity of gold compared to silicon the effect in the description of Anglin and Zurek is considerably weak distinctive [98]. However, this description cannot be ruled out completely as there might be another responsible effect for the contrast loss near the surface. On the other hand Machnikowski's ansatz covers the quantum-classical transition for clearly too large heights. His approach ends up in a too strong decoherence mechanism and can be ruled out. The theory of Scheel and Karstens tends to be the most promising one since the parameter fit of all curves is similar to the experimental trend. However, especially for distances below $5\,\mu\mathrm{m}$ a higher number of counts and thus, a higher data point density could not achieved without risking the cancellation of the measurement series. There is no question that a more accurate data acquisition is requested for a quantitative evaluation where a possible fit factor corresponds to the strength of decoherence. Unfortunately, it was also not possible to apply in these measurement series a second-order correlation analysis since the number of counts did not suffice for proper results.

In order to cross-check the whole interferometer and equipment and to test it for suitability, a silicon plate was installed later on. Thereby, all other components, in particular the single-atom tip, stayed untouched.

Meanwhile in further approaches beyond the scope of this thesis, decoherence effects for electrons above the silicon surface could be recorded successfully and images similar to [66] were determined. This suggests that the setup is able to perform such sensitive measurements and that the data for gold is reliable. Further tests for gold are planned.

As a next step the dependency of decoherence on the temperature and material properties such as conductivity needs to be investigated. It is crucial for a fully understanding of the decohering interaction with regard to potential alternative mechanisms. With COULOMB interaction in mind, superconductors, metals and semiconductors differ among others in their surface and electronic properties. Particularly for superconductors without dc resistivity the description with moving image charges in the plate as for normal conductors has to be reconsidered.

For that reason a commercial cryostat system was purchased in view of a capable temperature range between $2 - 500\,\mathrm{K}$. A detailed description of all components and the operation principle is given in this work. Although the cryostat was used up to now only for successful test runs, one further advantage will definitely be the accurate read out of the cold finger position. Compared to the current setup, a hole has to be drilled in the shielding tube and the positioning of the cold finger is challenging as there is no optical access.

Three promising candidates for a temperature study were described in more detail. Niobium as a well-known elementary superconductor ($T_C = 9.2\,\mathrm{K}$), yttrium barium copper oxide ($T_C = 92\,\mathrm{K}$) as a high temperature superconductor and the exotic compound vanadium dioxide with rapid changes of the optical properties when reaching $65\,^{\circ}\mathrm{C}$.

So far there is no theoretical prediction for the decoherence of free electrons above a superconducting surface due to COULOMB interaction. Solely KARSTENS and SCHEEL worked out first estimations for helium ions near a niobium surface on the basis of a two-fluid model of the dielectric function [100]. They concluded that the decoherence time suddenly increases by up to three orders of magnitude when passing the critical temperature. Therefore, such erratic behaviour of the decoherence strength is also expected for electrons.

Concerning fundamental questions in the area of decoherence measurements, further ideas are:

- In order to circumvent the parallelism problem during the traverse of the electrons, replacing the gold plate by a gold ball would be an interesting concept. For any beam trajectory there is a symmetrical crossing of the ball surface with a minimal distance. This concept is commonly used for boundary value problems in classical electrodynamics [206]. However, the theoretical description would be difficult and is yet not available as the decoherence strength would be position-dependent above the plate. The experimental realization requires a perfect spherical shape of the gold ball with diameters in the cm range. A holding adapter for the cold finger of the cryostat is then needed.

- For a further reduction of the energy width of the beam electrons, a system of two Wien filter could be used. One acts as the presented wave packet shifter and the second one serves as a highly precise monochromator. Thereby, the longitudinal coherence length and potentially the contrast increases [207]. Moreover, for different excitations of the Wien filter a quantum eraser unit can be formed [24]. The effect of the first Wien filter is undone by the second one. The contrast is completely restored as long as no measurement has taken place between. By

looking on the pictures in [24] it is evident that no irreversible interaction with the electromagnetic background field has taken place.

- In the context of surface-induced decoherence effects a closer look on the contrast for fringes near the biprism fiber surface is appropriate. Beam electrons which are deflected close to the fiber also suffer a loss of their coherence properties due to the interaction with the fiber material and the emission of bremsstrahlung of the acceleration process. However, this effect might be rather weak regarding the small diameter and deflection angle. An observation, if possible at all, would require a considerably higher magnification of the interference pattern. Even more interesting is the question if there is a measurable difference of the effect when installing two biprism fibers in the interferometer where the conductivity of the materials vary completely.

- A well prepared single-atom tip, made of tungsten and iridium and applied in this work, offers only one atom as emission spot. Thereby, one would assume that this implies the minimal possible source extension with perfect coherence properties. However, progress with new electron sources made of lanthanum hexaboride (LaB_6) is achieved [208] where it is taken advantage of the low work function of only 2.07 eV (work function of tungsten: 4.5 eV). In general, the work function determines the brightness and the energy spread of the electron beam. Thus, recent improvements in the fabrication of LaB_6 nanowires allowed to establish an ultrabright and monochromatic point source which can be operated tens of hours without current or intensity fluctuations [208]. Thereby, the brightness is increased by one order of magnitude compared to SATs [78].

  The implementation of such a LaB_6 point source into the biprism interferometer would highly improve the longitudinal coherence properties and the signal of the beam. Higher contrast values and more sensitive measurements would be possible. Also, stochastic current fluctuations and a general decay of emission current with time would be eliminated. Nevertheless, the effort for fabricating those tips is enormous and only feasible with outstanding experience and equipment. Thus, the hurdles for own fabrication are high but can be circumvented by establishing a cooperation.

8 Bibliography

[1] A. Pooch, M. Seidling, N. Kerker, R. Röpke, A. Rembold, W. T. Chang, I. S. Hwang, and A. Stibor, "Coherent properties of a tunable low-energy electron-matter-wave source", Phys. Rev. A **97**, 013611 (2018).

[2] A. Pooch, M. Seidling, M. Layer, A. Rembold, and A. Stibor, "A compact electron matter wave interferometer for sensor technology", Applied Physics Letters **110**, 223108 (2017).

[3] G. Schütz, A. Rembold, A. Pooch, S. Meier, P. Schneeweiss, A. Rauschenbeutel, A. Günther, W. Chang, I. Hwang, and A. Stibor, "Biprism electron interferometry with a single atom tip source", Ultramicroscopy **141**, 9 (2014).

[4] A. Rembold, G. Schütz, W. T. Chang, A. Stefanov, A. Pooch, I. S. Hwang, A. Günther, and A. Stibor, "Correction of dephasing oscillations in matter-wave interferometry", Phys. Rev. A **89**, 033635 (2014).

[5] G. Schütz, A. Rembold, A. Pooch, H. Prochel, and A. Stibor, "Effective beam separation schemes for the measurement of the electric Aharonov-Bohm effect in an ion interferometer", Ultramicroscopy **158**, 65 (2015).

[6] G. Schütz, A. Rembold, A. Pooch, W. Chang, and A. Stibor, "Electron matter wave interferences at high vacuum pressures", Measurement **68**, 201 (2015).

[7] I. Newton, "New Theory about Light and Colours", Philosophical Transactions (1665-1678) **6**, 3075 (1671).

[8] C. Huygens, *Traité de la lumière: Ou sont expliquées les causes de ce qui luy arrive dans la reflexion, et dans la refraction Et particulierement dans l'etrange refraction du cristal d'Islande ; Avec un discours de la cause de la pesanteur* (Pierre Vander Aa, 1690).

[9] T. Young, "Experimental demonstration of the general law of the interference of light", Philosophical Transactions of the Royal society of London **94**, 1 (1804).

[10] J. C. Jamin, "Neuer Interferential-Refractor", Annalen der Physik und Chemie **98**, 345 (1856).

[11] A. A. Michelson and E. W. Morley, "On the Relative Motion of the Earth and of the Luminiferous Ether", American Journal of Science **34**, 333 (1887).

[12] L. Zehnder, "Ein neuer Interferenzrefraktor", Zeitschrift für Instrumentenkunde **11**, 275 (1891).

[13] L. Mach, "Ueber einen Interferenzrefraktor", Zeitschrift für Instrumentenkunde **12**, 89 (1892).

[14] A. Pérot and C. Fabry, "On the Application of Interference Phenomena to the Solution of Various Problems of Spectroscopy and Metrology", The Astrophysical Journal **9**, 87 (1899).

[15] J. C. Maxwell, *A treatise on electricity and magnetism*, Vol. 1 (Clarendon press, 1881).

[16] A. Einstein, "Über einen die Erzeugung und Verwandlung des Lichtes betreffenden heuristischen Gesichtspunkt", Annalen der Physik **17**, 132 (1905).

[17] M. Planck, "Ueber das Gesetz der Energieverteilung im Normalspectrum", Annalen der Physik **309**, 553 (1901).

[18] A. H. Compton, "A Quantum Theory of the Scattering of X-rays by Light Elements", Physical Review **21**, 483 (1923).

[19] L. De Broglie, "Waves and Quanta", Nature **112**, 540 (1923).

[20] C. Davisson and L. H. Germer, "Diffraction of Electrons by a Crystal of Nickel", Phys. Rev. **30**, 705 (1927).

[21] H. Boersch, "Fresnelsche Elektronenbeugung", Naturwissenschaften **28**, 709 (1940).

[22] G. Möllenstedt and H. Düker, "Fresnelscher Interferenzversuch mit einem Biprisma für Elektronenwellen", Naturwissenschaften **42**, 41 (1955).

[23] G. Möllenstedt and H. Düker, "Beobachtungen und Messungen an Biprisma-Interferenzen mit Elektronenwellen", Zeitschrift für Physik **145**, 377 (1956).

[24] F. Hasselbach, "Progress in electron- and ion-interferometry", Reports on Progress in Physics **73**, 016101 (2010).

[25] C. Jönsson, "Elektroneninterferenzen an mehreren künstlich hergestellten Feinspalten", Zeitschrift für Physik **161**, 454 (1961).

[26] "The most beautiful experiment", PhysicsWorld **September**, 15 (2002).

[27] H. Rauch, W. Treimer, and U. Bonse, "Test of a single crystal neutron interferometer", Physics Letters A **47**, 369 (1974).

[28] R. Colella, A. W. Overhauser, and S. A. Werner, "Observation of Gravitationally Induced Quantum Interference", Physical Review Letters **34**, 1472 (1975).

[29] O. Carnal and J. Mlynek, "Young's double-slit experiment with atoms: A simple atom interferometer", Physical Review Letters **66**, 2689 (1991).

[30] D. W. Keith, C. R. Ekstrom, Q. A. Turchette, and D. E. Pritchard, "An Interferometer for Atoms", Physical Review Letters **66**, 2693 (1991).

[31] M. Kasevich and S. Chu, "Atomic Interferometry Using Stimulated Raman Transitions", Physical Review Letters **67**, 181 (1991).

[32] D. S. Weiss, B. C. Young, and S. Chu, "Precision Measurement of the Photon Recoil of an Atom Using Atomic Interferometry", Physical Review Letters **70**, 2706 (1993).

[33] C. R. Ekstrom, J. Schmiedmayer, M. S. Chapman, T. D. Hammond, and D. E. Pritchard, "Measurement of the electric polarizability of sodium with an atom interferometer", Physical Review A **51**, 3883 (1995).

[34] T. L. Gustavson, P. Bouyer, and M. A. Kasevich, "Precision Rotation Measurements with an Atom Interferometer Gyroscope", Physical Review Letters **78**, 2046 (1997).

[35] A. Peters, K. Y. Chung, and S. Chu, "Measurement of gravitational acceleration by dropping atoms", Nature **400**, 849 (1999).

[36] M. R. Andrews, C. G. Townsend, H.-J. Miesner, D. S. Durfee, D. M. Kurn, and W. Ketterle, "Observation of Interference Between Two Bose Condensates", Science **275**, 637 (1997).

[37] M. Arndt, O. Nairz, J. Vos-Andreae, C. Keller, G. Van der Zouw, and A. Zeilinger, "Wave–particle duality of C_{60} molecules", Nature **401**, 680 (1999).

[38] B. Brezger, L. Hackermüller, S. Uttenthaler, J. Petschinka, M. Arndt, and A. Zeilinger, "Matter-Wave Interferometer for Large Molecules", Physical Review Letters **88**, 100404 (2002).

[39] S. Eibenberger, S. Gerlich, M. Arndt, M. Mayor, and J. Tüxen, "Matter–wave interference of particles selected from a molecular library with masses exceeding 10000 amu", Physical Chemistry Chemical Physics **15**, 14696 (2013).

[40] B. P. Abbott, R. Abbott, and T. D. e. a. Abbott (LIGO Scientific Collaboration and Virgo Collaboration), "Observation of Gravitational Waves from a Binary Black Hole Merger", Phys. Rev. Lett. **116**, 061102 (2016).

[41] M. Armano, H. Audley, G. Auger, J. T. Baird, M. Bassan, P. Binetruy, M. Born, D. Bortoluzzi, N. Brandt, M. Caleno, *et al.*, "Sub-Femto-g Free Fall for Space-Based Gravitational Wave Observatories: LISA Pathfinder Results", Physical Review Letters **116**, 231101 (2016).

[42] R. B. Hurst, M. Mayerbacher, A. Gebauer, K. U. Schreiber, and J.-P. R. Wells, "High-accuracy absolute rotation rate measurements with a large ring laser gyro: establishing the scale factor", Applied Optics **56**, 1124 (2017).

[43] Y. Margalit, Z. Zhou, S. Machluf, D. Rohrlich, Y. Japha, and R. Folman, "A self-interfering clock as a "which path" witness", Science **349**, 1205 (2015).

[44] M. Arndt and C. Brand, "Interference of atomic clocks", Science **349**, 1168 (2015).

[45] H. Müntinga, H. Ahlers, M. Krutzik, A. Wenzlawski, S. Arnold, D. Becker, K. Bongs, H. Dittus, H. Duncker, N. Gaaloul, *et al.*, "Interferometry with Bose-Einstein Condensates in Microgravity", Physical Review Letters **110**, 093602 (2013).

[46] B. Barrett, L. Antoni-Micollier, L. Chichet, B. Battelier, T. Lévèque, A. Landragin, and P. Bouyer, "Dual matter-wave inertial sensors in weightlessness", Nature Communications **7**, 13786 (2016).

[47] S. M. Dickerson, J. M. Hogan, A. Sugarbaker, D. M. S. Johnson, and M. A. Kasevich, "Multiaxis Inertial Sensing with Long-Time Point Source Atom Interferometry", Physical Review Letters **111**, 083001 (2013).

[48] T. Kovachy, P. Asenbaum, C. Overstreet, C. A. Donnelly, S. M. Dickerson, A. Sugarbaker, J. M. Hogan, and M. A. Kasevich, "Quantum superposition at the half-metre scale", Nature **528**, 530 (2015).

[49] W. H. Zurek, "Decoherence, einselection, and the quantum origins of the classical", Rev. Mod. Phys. **75**, 715 (2003).

[50] K. Hornberger, S. Uttenthaler, B. Brezger, L. Hackermüller, M. Arndt, and A. Zeilinger, "Collisional Decoherence Observed in Matter Wave Interferometry", Physical Review Letters **90**, 160401 (2003).

[51] K. Walter, B. A. Stickler, and K. Hornberger, "Collisional decoherence of polar molecules", Physical Review A **93**, 063612 (2016).

[52] L. Hackermüller, K. Hornberger, B. Brezger, A. Zeilinger, and M. Arndt, "Decoherence of matter waves by thermal emission of radiation", Nature **427**, 711 (2004).

[53] K. Hornberger, L. Hackermüller, and M. Arndt, "Influence of molecular temperature on the coherence of fullerenes in a near-field interferometer", Physical Review A **71**, 023601 (2005).

[54] J. P. Cotter, S. Eibenberger, L. Mairhofer, X. Cheng, P. Asenbaum, M. Arndt, K. Walter, S. Nimmrichter, and K. Hornberger, "Coherence in the presence of absorption and heating in a molecule interferometer", Nature Communications **6**, 7336 (2015).

[55] T. Juffmann, H. Ulbricht, and M. Arndt, "Experimental methods of molecular matter-wave optics", Reports on Progress in Physics **76**, 086402 (2013).

[56] U. Maier, *Ein Biprisma-Interferometer für Ionen*, Ph.D. thesis, Universität Tübingen (1997).

[57] F. Hasselbach and U. Maier, "Quantum Coherence and Decoherence", ISQM-Tokyo 98 ed Y. Y. Ono and K. Fujikawa (Amsterdam: Elsevier) , 299 (1999).

[58] Y. Aharonov and D. Bohm, "Significance of Electromagnetic Potentials in the Quantum Theory", Phys. Rev. **115**, 485 (1959).

[59] G. Möllenstedt and W. Bayh, "Elektronen-Biprisma-Interferenzen mit weit getrennten kohärenten Teilbündeln", Naturwissenschaften **48**, 400 (1961).

[60] G. Möllenstedt and W. Bayh, "Kontinuierliche Phasenschiebung von Elektronenwellen im kraftfeldfreien Raum durch das magnetische Vektorpotential eines Solenoids", Physik Journal **18**, 299 (1962).

[61] W. Bayh, "Messung der kontinuierlichen Phasenschiebung von Elektronenwellen im kraftfeldfreien Raum durch das magnetische Vektorpotential einer Wolfram-Wendel", Zeitschrift für Physik **169**, 492 (1962).

[62] E. J. Post, "Sagnac effect", Reviews of Modern Physics **39**, 475 (1967).

[63] F. Hasselbach and M. Nicklaus, "Sagnac experiment with electrons: Observation of the rotational phase shift of electron waves in vacuum", Phys. Rev. A **48**, 143 (1993).

[64] R. Hanbury Brown, "The question of correlation between photons in coherent light rays", Nature **178**, 1447 (1956).

[65] H. Kiesel, A. Renz, and F. Hasselbach, "Observation of Hanbury Brown–Twiss anticorrelations for free electrons", Nature **418**, 392 (2002).

[66] P. Sonnentag and F. Hasselbach, "Measurement of Decoherence of Electron Waves and Visualization of the Quantum-Classical Transition", Phys. Rev. Lett. **98**, 200402 (2007).

[67] P. Sonnentag, *Ein Experiment zur kontrollierten Dekohärenz in einem Elektronen-Biprisma-Interferometer*, Ph.D. thesis, Universität Tübingen (2006).

[68] J. R. Anglin and W. H. Zurek, "A Precision Test Of Decoherence", eprint arXiv:quant-ph/9611049 (1996).

[69] S. Scheel and S. Y. Buhmann, "Path decoherence of charged and neutral particles near surfaces", Phys. Rev. A **85**, 030101 (2012).

[70] H.-S. Kuo, I.-S. Hwang, T.-Y. Fu, Y.-C. Lin, C.-C. Chang, and T. T. Tsong, "Noble Metal/W(111) Single-Atom Tips and Their Field Electron and Ion Emission Characteristics", Japanese Journal of Applied Physics **45**, 8972 (2006).

[71] D. Ehberger, J. Hammer, M. Eisele, M. Krüger, J. Noe, A. Högele, and P. Hommelhoff, "Highly Coherent Electron Beam from a Laser-Triggered Tungsten Needle Tip", Phys. Rev. Lett. **114**, 227601 (2015).

[72] P. Hommelhoff, Y. Sortais, A. Aghajani-Talesh, and M. A. Kasevich, "Field Emission Tip as a Nanometer Source of Free Electron Femtosecond Pulses", Phys. Rev. Lett. **96**, 077401 (2006).

[73] J. Hammer, J. Hoffrogge, S. Heinrich, and P. Hommelhoff, "Phase-Resolved Electron Guiding in Optimized Chip-Based Microwave Potentials", Physical Review Applied **2**, 044015 (2014).

[74] J. Hammer, S. Thomas, P. Weber, and P. Hommelhoff, "Microwave Chip-Based Beam Splitter for Low-Energy Guided Electrons", Phys. Rev. Lett. **114**, 254801 (2015).

[75] F. Warken, E. Vetsch, D. Meschede, M. Sokolowski, and A. Rauschenbeutel, "Ultra-sensitive surface absorption spectroscopy using sub-wavelength diameter optical fibers", Optics Express **15**, 11952 (2007).

[76] F. Warken, *Ultradünne Glasfasern als Werkzeug zur Kopplung von Licht und Materie*, Ph.D. thesis, Universität Bonn (2007).

[77] B. Cho, T. Ichimura, R. Shimizu, and C. Oshima, "Quantitative Evaluation of Spatial Coherence of the Electron Beam from Low Temperature Field Emitters", Phys. Rev. Lett. **92**, 246103 (2004).

[78] C.-C. Chang, H.-S. Kuo, I.-S. Hwang, and T. T. Tsong, "A fully coherent electron beam from a noble-metal covered W(111) single-atom emitter", Nanotechnology **20**, 115401 (2009).

[79] O. Jagutzki, V. Mergel, K. Ullmann-Pfleger, L. Spielberger, U. Spillmann, R. Dörner, and H. Schmidt-Böcking, "A broad-application microchannel-plate detector system for advanced particle or photon detection tasks: large area imaging, precise multi-hit timing information and high detection rate", Nuclear Instruments and Methods in Physics Research Section A: Accelerators, Spectrometers, Detectors and Associated Equipment **477**, 244 (2002).

[80] S. S. O. Jagutzki, A. Czasch, "Performance of a compact position-sensitive photon counting detector with image charge coupling to an air-side anode", Proc. SPIE **8727**, 12 (2013).

[81] E. Joos, "Decoherence Through Interaction with the Environment," in *Decoherence and the Appearance of a Classical World in Quantum Theory* (Springer Berlin Heidelberg, Berlin, Heidelberg, 1996) pp. 35–136.

[82] E. Schrödinger, "Die gegenwärtige Situation in der Quantenmechanik", Naturwissenschaften **23**, 823 (1935).

[83] H. D. Zeh, "On the interpretation of measurement in quantum theory", Foundations of Physics **1**, 69 (1970).

[84] H. D. Zeh, "Toward a quantum theory of observation", Foundations of Physics **3**, 109 (1973).

[85] W. H. Zurek, "Pointer basis of quantum apparatus: Into what mixture does the wave packet collapse?", Phys. Rev. D **24**, 1516 (1981).

[86] W. P. Putnam and M. F. Yanik, "Noninvasive electron microscopy with interaction-free quantum measurements", Phys. Rev. A **80**, 040902 (2009).

[87] T. Pfau, S. Spälter, C. Kurtsiefer, C. R. Ekstrom, and J. Mlynek, "Loss of Spatial Coherence by a Single Spontaneous Emission", Phys. Rev. Lett. **73**, 1223 (1994).

[88] M. S. Chapman, T. D. Hammond, A. Lenef, J. Schmiedmayer, R. A. Rubenstein, E. Smith, and D. E. Pritchard, "Photon Scattering from Atoms in an Atom Interferometer: Coherence Lost and Regained", Phys. Rev. Lett. **75**, 3783 (1995).

[89] D. A. Kokorowski, A. D. Cronin, T. D. Roberts, and D. E. Pritchard, "From Single- to Multiple-Photon Decoherence in an Atom Interferometer", Phys. Rev. Lett. **86**, 2191 (2001).

[90] M. Brune, E. Hagley, J. Dreyer, X. Maitre, A. Maali, C. Wunderlich, J. M. Raimond, and S. Haroche, "Observing the Progressive Decoherence of the Meter in a Quantum Measurement", Phys. Rev. Lett. **77**, 4887 (1996).

[91] C. J. Myatt, B. E. King, Q. A. Turchette, C. A. Sackett, D. Kielpinski, W. M. Itano, C. Monroe, and D. J. Wineland, "Decoherence of motional states of trapped ions", Journal of Modern Optics **47**, 2181 (2000).

[92] S. Haroche, "Nobel Lecture: Controlling photons in a box and exploring the quantum to classical boundary", Rev. Mod. Phys. **85**, 1083 (2013).

[93] C. Guerlin, J. Bernu, S. Deleglise, C. Sayrin, S. Gleyzes, S. Kuhr, M. Brune, J.-M. Raimond, and S. Haroche, "Progressive field-state collapse and quantum non-demolition photon counting", Nature **448**, 889 (2007).

[94] M. Mohseni, J. S. Lundeen, K. J. Resch, and A. M. Steinberg, "Experimental Application of Decoherence-Free Subspaces in an Optical Quantum-Computing Algorithm", Phys. Rev. Lett. **91**, 187903 (2003).

[95] M. Wallquist, K. Hammerer, P. Rabl, M. Lukin, and P. Zoller, "Hybrid quantum devices and quantum engineering", Physica Scripta **2009**, 014001 (2009).

[96] A. W. Harrow and A. Montanaro, "Quantum computational supremacy", Nature **549**, 203 (2017).

[97] S. Boixo, S. V. Isakov, V. N. Smelyanskiy, R. Babbush, N. Ding, Z. Jiang, M. J. Bremner, J. M. Martinis, and H. Neven, "Characterizing quantum supremacy in near-term devices", Nature Physics **14**, 595 (2018).

[98] J. R. Anglin, J. P. Paz, and W. H. Zurek, "Deconstructing decoherence", Phys. Rev. A **55**, 4041 (1997).

[99] P. Machnikowski, "Theory of which path dephasing in single electron interference due to trace in conductive environment", Phys. Rev. B **73**, 155109 (2006).

[100] K. Karstens, *Pfaddekohärenz von Elektronen und Ionen in der Nähe dielektrischer Oberflächen*, Master's thesis, Universität Rostock (2014).

[101] F. Charbonnier, "Developing and using the field emitter as a high intensity electron source", Applied Surface Science **94-95**, 26 (1996).

[102] E. Rokuta, T. Itagaki, T. Ishikawa, B.-L. Cho, H.-S. Kuo, T. Tsong, and C. Oshima, "Single-atom coherent field electron emitters for practical application to electron microscopy: Buildup controllability, self-repairing function and demountable characteristic", Applied Surface Science **252**, 3686 (2006).

[103] B. W. Ward, J. A. Notte, and N. P. Economou, "Helium ion microscope: A new tool for nanoscale microscopy and metrology", Journal of Vacuum Science & Technology B: Microelectronics and Nanometer Structures Processing, Measurement, and Phenomena **24**, 2871 (2006).

[104] T.-Y. Fu, L.-C. Cheng, C.-H. Nien, and T. T. Tsong, "Method of creating a Pd-covered single-atom sharp W pyramidal tip: Mechanism and energetics of its formation", Phys. Rev. B **64**, 113401 (2001).

[105] W.-T. Chang, I.-S. Hwang, M.-T. Chang, C.-Y. Lin, W.-H. Hsu, and J.-L. Hou, "Method of electrochemical etching of tungsten tips with controllable profiles", Review of Scientific Instruments **83**, 083704 (2012).

[106] K. S. Yeong and J. T. L. Thong, "Life cycle of a tungsten cold field emitter", Journal of Applied Physics **99**, 104903 (2006).

[107] I.-S. Hwang, W.-T. Chang, C.-Y. Lin, and W.-H. Hsu, "Low-Energy Electron Diffractive Imaging Based on a Single-Atom Electron Source", Microscopy and Microanalysis **21**, 839 (2015).

[108] J.-N. Longchamp, T. Latychevskaia, C. Escher, and H.-W. Fink, "Low-energy electron holographic imaging of individual tobacco mosaic virions", Applied Physics Letters **107**, 133101 (2015).

[109] T. Latychevskaia, W.-H. Hsu, W.-T. Chang, C.-Y. Lin, and I.-S. Hwang, "Three-dimensional surface topography of graphene by divergent beam electron diffractions", Nature Communications **8** (2017).

[110] M. Gulde, S. Schweda, G. Storeck, M. Maiti, H. K. Yu, A. M. Wodtke, S. Schäfer, and C. Ropers, "Ultrafast low-energy electron diffraction in transmission resolves polymer/graphene superstructure dynamics", Science **345**, 200 (2014).

[111] P. Kruit, R. Hobbs, C.-S. Kim, Y. Yang, V. Manfrinato, J. Hammer, S. Thomas, P. Weber, B. Klopfer, C. Kohstall, T. Juffmann, M. Kasevich, P. Hommelhoff, and K. Berggren, "Designs for a quantum electron microscope", Ultramicroscopy **164**, 31 (2016).

[112] A. Günther, A. Rembold, G. Schütz, and A. Stibor, "Multifrequency perturbations in matter-wave interferometry", Phys. Rev. A **92**, 053607 (2015).

[113] A. Rembold, G. Schütz, R. Röpke, W. T. Chang, I. S. Hwang, A. Günther, and A. Stibor, "Vibrational dephasing in matter-wave interferometers", New Journal of Physics **19**, 033009 (2017).

[114] A. Stibor, K. Hornberger, L. Hackermüller, A. Zeilinger, and M. Arndt, "Talbot-Lau interferometry with fullerenes: Sensitivity to inertial forces and vibrational dephasing", Laser Physics **15**, 10 (2005).

[115] A. Rembold, *Second-order correlation analysis of multifrequency dephasing in single-particle interferometry*, Ph.D. thesis, Universität Tübingen (2017).

[116] A. Rembold, R. Röpke, G. Schütz, J. Fortagh, A. Stibor, and A. Günther, "Second-order correlations in single-particle interferometry", New Journal of Physics **19**, 103029 (2017).

[117] F. Lenz and G. Wohland, "Effect of chromatic aberration and partial coherence on the interference pattern of an electron biprism interferometer", Optik **67**, 315 (1984).

[118] W. H. Zurek, "Preferred States, Predictability, Classicality and the Environment-Induced Decoherence", Progress of Theoretical Physics **89**, 281 (1993).

[119] J. R. Anglin and W. H. Zurek, "Decoherence of quantum fields: Pointer states and predictability", Phys. Rev. D **53**, 7327 (1996).

[120] E. Joos and H. D. Zeh, "The emergence of classical properties through interaction with the environment", Zeitschrift für Physik B Condensed Matter **59**, 223 (1985).

[121] T. H. Boyer, "Penetration of the electric and magnetic velocity fields of a non-relativistic point charge into a conducting plane", Phys. Rev. A **9**, 68 (1974).

[122] T. W. Darling, F. Rossi, G. I. Opat, and G. F. Moorhead, "The fall of charged particles under gravity: A study of experimental problems", Rev. Mod. Phys. **64**, 237 (1992).

[123] W. H. Zurek, "Reduction of the Wavepacket: How Long Does it Take?" in *Frontiers of Nonequilibrium Statistical Physics*, edited by G. T. Moore and M. O. Scully (Springer US, Boston, MA, 1986) pp. 145–149.

[124] F. Petruccione and H.-P. Breuer, *The theory of open quantum systems* (Oxford Univ. Press, Berlin, 2002).

[125] F. Hasselbach, "A ruggedized miniature UHV electron biprism interferometer for new fundamental experiments and applications", Zeitschrift für Physik B Condensed Matter **71**, 443 (1988).

[126] M. Nicklaus and F. Hasselbach, "Wien filter: A wave-packet-shifting device for restoring longitudinal coherence in charged-matter-wave interferometers", Phys. Rev. A **48**, 152 (1993).

[127] F. Hasselbach, H. Kiesel, and P. Sonnentag, "Exploration of the Fundamentals of Quantum Mechanics by Charged Particle Interferometry", in *Decoherence: Theoretical, Experimental, and Conceptual Problems*, edited by P. Blanchard, E. Joos, D. Giulini, C. Kiefer, and I.-O. Stamatescu (Springer Berlin Heidelberg, 2000) pp. 201–212.

[128] P. Sonnentag and F. Hasselbach, "Decoherence of electron waves due to induced charges moving through a nearby resistive material", Brazilian Journal of Physics **35**, 385 (2005).

[129] R. Alicki, M. Horodecki, P. Horodecki, R. Horodecki, L. Jacak, and P. Machnikowski, "Optimal strategy for a single-qubit gate and the trade-off between opposite types of decoherence", Phys. Rev. A **70**, 010501 (2004).

[130] J. v. Neumann, "Mathematische Begründung der Quantenmechanik", Nachrichten von der Gesellschaft der Wissenschaften zu Göttingen, Mathematisch-Physikalische Klasse **1927**, 1 (1927).

[131] J. Barth, R. Johnson, M. Cardona, and E. Palik, "Handbook of optical constants of solids II", Academic Press, New York (1991).

[132] N. Wiener, "Generalized harmonic analysis", Acta Math. **55**, 117 (1930).

[133] A. Khintchine, "Korrelationstheorie der stationären stochastischen Prozesse", Mathematische Annalen **109**, 604 (1934).

[134] Y. Saito, *Carbon nanotube and related field emitters: fundamentals and applications* (John Wiley & Sons, 2010).

[135] D. Temple, "Recent progress in field emitter array development for high performance applications", Materials Science and Engineering: R: Reports **24**, 185 (1999).

[136] L. Reimer, *Scanning electron microscopy: physics of image formation and microanalysis*, Vol. 45 (Springer, 2013).

[137] N. De Jonge, Y. Lamy, K. Schoots, and T. H. Oosterkamp, "High brightness electron beam from a multi-walled carbon nanotube", Nature **420**, 393 (2002).

[138] K. Jousten, K. Böhringer, R. Börret, and S. Kalbitzer, "Growth and current characteristics of stable protrusions on tungsten field ion emitters", Ultramicroscopy **26**, 301 (1988).

[139] H.-W. Fink, "Point source for ions and electrons", Physica Scripta **38**, 260 (1988).

[140] H.-S. Kuo, I.-S. Hwang, T.-Y. Fu, Y.-H. Lu, C.-Y. Lin, and T. T. Tsong, "Gas field ion source from an Ir/ W < 111> single-atom tip", Applied physics letters **92**, 063106 (2008).

[141] A. Knoblauch, C. Wilbertz, T. Miller, and S. Kalbitzer, "Field electron emission properties of a supertip", Journal of Physics D: Applied Physics **29**, 470 (1996).

[142] F. Warken, A. Rauschenbeutel, and T. Bartholomäus, "Fiber Pulling Profits from Precise Positioning-Precise motion control improves manufacturing of fiber optical resonators.", Photonics Spectra **42**, 73 (2008).

[143] A. Stiebeiner, R. Garcia-Fernandez, and A. Rauschenbeutel, "Design and optimization of broadband tapered optical fibers with a nanofiber waist", Opt. Express **18**, 22677 (2010).

[144] J. D. Carter and J. D. D. Martin, "Energy shifts of Rydberg atoms due to patch fields near metal surfaces", Phys. Rev. A **83**, 032902 (2011).

[145] G. Sagué, E. Vetsch, W. Alt, D. Meschede, and A. Rauschenbeutel, "Cold-Atom Physics Using Ultrathin Optical Fibers: Light-Induced Dipole Forces and Surface Interactions", Phys. Rev. Lett. **99**, 163602 (2007).

[146] M. Peskin and A. Tonomura, "Lect", Notes Phys **340**, 115 (1989).

[147] Y. Aharonov and D. Bohm, "Further Considerations on Electromagnetic Potentials in the Quantum Theory", Phys. Rev. **123**, 1511 (1961).

[148] R. G. Chambers, "Shift of an Electron Interference Pattern by Enclosed Magnetic Flux", Phys. Rev. Lett. **5**, 3 (1960).

[149] G. Wohland, *Messung der Kohärenzlänge von Elektronen im Elektroneninterferometer mit Wien-Filter*, Ph.D. thesis, Universität Tübingen (1981).

[150] H. Wollnik, *Optics of Charged Particles* (Academic Press, 1987).

[151] RoentDek, *MCP Delay Line Detector Manual* (RoentDek Handels GmbH, version: 11.0.1803.1).

[152] RoentDek, *The Roentdek FAMP8, (D)FAMP6, PreFAMP6, FAMP3, FAMP1+, bFAMP3 and bFAMP1* (RoentDek Handels GmbH, version: 11.0.1701.1).

[153] RoentDek, *The Roentdek Constant Friction Discriminators CFD8c, CFD7x, CFD4c, CFD1c and CFD 1x* (RoentDek Handels GmbH, version: 11.0.1701.1).

[154] RoentDek, *TDC8HP System Manual* (RoentDek Handels GmbH, version: 11.0.1505.1).

[155] E. Hecht, *Optik*, 6th ed. (De Gruyter, Incorporated, 2014).

[156] E. Rokuta, H.-S. Kuo, T. Itagaki, K. Nomura, T. Ishikawa, B.-L. Cho, I.-S. Hwang, T. Tsong, and C. Oshima, "Field emission spectra of single-atom tips with thermodynamically stable structures", Surface Science **602**, 2508 (2008).

[157] W.-T. Chang, C.-Y. Lin, W.-H. Hsu, M.-T. Chang, Y.-S. Chen, E.-T. Hwu, and I.-S. Hwang, "Low-voltage coherent electron imaging based on a single-atom electron", ArXiv e-prints: 1512.08371 (2015).

[158] W. P. Dyke, J. K. Trolan, W. W. Dolan, and G. Barnes, "The Field Emitter: Fabrication, Electron Microscopy, and Electric Field Calculations", Journal of Applied Physics **24**, 570 (1953).

[159] A. V. Crewe, D. N. Eggenberger, J. Wall, and L. M. Welter, "Electron Gun Using a Field Emission Source", Review of Scientific Instruments **39**, 576 (1968).

[160] I. Sokolovskaia, "Surface migration of tungsten atoms in an electric field", Soviet Physics-Technical Physics **1**, 1147 (1956).

[161] L. W. Swanson and L. C. Crouser, "Total-Energy Distribution of Field-Emitted Electrons and Single-Plane Work Functions for Tungsten", Phys. Rev. **163**, 622 (1967).

[162] E. Krimmel, G. Möllenstedt, and W. Rothemund, "Measurement of contact potential differences by electron interferometry", Applied Physics Letters **5**, 209 (1964).

[163] W. Brünger, "Elektroneninterferometer mit Feldemissionskathode zur Messung von Kontaktpotentialdifferenzen im Ultrahochvakuum", Zeitschrift für Physik A Hadrons and nuclei **250**, 263 (1972).

[164] P. Walker and W. H. Tarn, *CRC Handbook of Metal Etchants* (CRC Press, Boca Raton, Fla, 1990).

[165] J. Komrska, V. Drahoš, and A. Delong, "Intensity Distributions in Electron Interference Phenomena Produced by an Electrostatic Bi-prism", Optica Acta: International Journal of Optics **14**, 147 (1967).

[166] J. Komrska and B. Vlachová, "Justification of the Model for Electron Interference Produced by an Electrostatic Biprism", Optica Acta: International Journal of Optics **20**, 207 (1973).

[167] R. Saini, Z. Jandric, K. Tsui, T. Udeshi, and D. Tuggle, "Manufacturable MEMS microcolumn", Microelectronic Engineering **78-79**, 62 (2005).

[168] J. Fox, R. Saini, K. Tsui, and G. Verbeck, "Microelectromechanical system assembled ion optics: An advance to miniaturization and assembly of electron and ion optics", The Review of scientific instruments **80**, 093302 (2009).

[169] J. F. Clauser, "Ultra-high sensitivity accelerometers and gyroscopes using neutral atom matter-wave interferometry", Physica B+C **151**, 262 (1988).

[170] M. Nicklaus, *Ein Sagnac-Experiment mit Elektronenwellen*, Ph.D. thesis, Universität Tübingen (1989).

[171] M. R. Torr and J. Devlin, "Intensified charge coupled devices for use as a space-borne spectrographic image-plane detector system", Appl. Opt. **21**, 3091 (1982).

[172] W. D. Ruijter, "Imaging properties and applications of slow-scan charge-coupled device cameras suitable for electron microscopy", Micron **26**, 247 (1995).

[173] P. Brauchle, *Elektronenstrahl-Messgerät mit Feldemissionskathode*, Ph.D. thesis, Universität Tübingen (1986).

[174] M. Itano, F. W. Kern, M. Miyashita, and T. Ohmi, "Particle removal from silicon wafer surface in wet cleaning process", IEEE Transactions on Semiconductor Manufacturing **6**, 258 (1993).

[175] L. J. van der Pauw, "A method of measuring specific resistivity and Hall effect of discs of arbitrary shapes", Philips Research Reports **13**, 1 (1958).

[176] K. Fuchs, "The conductivity of thin metallic films according to the electron theory of metals", Mathematical Proceedings of the Cambridge Philosophical Society **34**, 100 (1938).

[177] G. Raschke, *Molekulare Erkennung mit einzelnen Gold–Nanopartikeln*, Ph.D. thesis, Ludwig-Maximilians-Universität München (2005).

[178] E. H. Sondheimer, "The mean free path of electrons in metals", Advances in physics **1**, 1 (1952).

[179] R. Buhl, "Interferenzmikroskopie mit Elektronenwellen", Zeitschrift für Physik **155**, 395 (1959).

[180] H. Schmid, *Ein Elektronen-Interferometer mit 300 Mikrometer weit getrennten kohärenten Teilbündeln zur Erzeugung hoher Gangunterschiede und Messung der Phasenschiebung durch das magnetische Vektorpotential bei metallisch abgeschirmtem Magnetfluß*, Ph.D. thesis, Eberhard-Karls-Universität Tübingen (1985).

[181] C. Buzea and K. Robbie, "Assembling the puzzle of superconducting elements: a review", Superconductor Science and Technology **18**, R1 (2005).

[182] A. Soni and G. S. Okram, "Resistivity and thermopower measurement setups in the temperature range of 5-325 K", Review of Scientific Instruments **79**, 125103 (2008).

[183] J. G. Bednorz and K. A. Müller, "Possible highTc superconductivity in the Ba-La-Cu-O system", Zeitschrift für Physik B Condensed Matter **64**, 189 (1986).

[184] J. Bardeen, L. N. Cooper, and J. R. Schrieffer, "Theory of Superconductivity", Phys. Rev. **108**, 1175 (1957).

[185] M. Gurvitch and A. T. Fiory, "Resistivity of $La_{1.825}Sr_{0.175}CuO_4$ and $YBa_2Cu_3O_7$ to 1100 K: Absence of saturation and its implications", Phys. Rev. Lett. **59**, 1337 (1987).

[186] D. Kölle and staff, private communication (2013).

[187] E. E. Chain, "Optical properties of vanadium dioxide and vanadium pentoxide thin films", Appl. Opt. **30**, 2782 (1991).

[188] M. Soltani, M. Chaker, E. Haddad, and R. Kruzelesky, "1× 2 optical switch devices based on semiconductor-to-metallic phase transition characteristics of VO2 smart coatings", Measurement Science and Technology **17**, 1052 (2006).

[189] J. H. Park, J. M. Coy, T. S. Kasirga, C. Huang, Z. Fei, S. Hunter, and D. H. Cobden, "Measurement of a solid-state triple point at the metal–insulator transition in VO_2", Nature **500**, 431 (2013).

[190] M. Gurvitch, S. Luryi, A. Polyakov, and A. Shabalov, "Nonhysteretic behavior inside the hysteresis loop of VO_2 and its possible application in infrared imaging", Journal of Applied Physics **106**, 104504 (2009).

[191] J. Nag and R. F. H. Jr, "Synthesis of vanadium dioxide thin films and nanoparticles", Journal of Physics: Condensed Matter **20**, 264016 (2008).

[192] F. Guinneton, L. Sauques, J.-C. Valmalette, F. Cros, and J.-R. Gavarri, "Optimized infrared switching properties in thermochromic vanadium dioxide thin films: role of deposition process and microstructure", Thin Solid Films **446**, 287 (2004).

[193] N. R. Mlyuka and R. T. Kivaisi, "Correlation between optical, electrical and structural properties of vanadium dioxide thin films", Journal of Materials Science **41**, 5619 (2006).

[194] M. Tinkham, *Introduction to Superconductivity*, Vol. 1 (Courier Corporation, 2004).

[195] F. London and H. London, "The electromagnetic equations of the supraconductor", Proceedings of the Royal Society of London A: Mathematical, Physical and Engineering Sciences **149**, 71 (1935).

[196] H. Kiesel, A. Renz, and F. Hasselbach, "Observation of Hanbury Brown-Twiss anticorrelations for free electrons", Nature **418**, 392 (2002).

[197] H. Lorentz, "Electromagnetic phenomena in a system moving with any velocity smaller than that of light", Koninklijke Nederlandse Akademie van Wetenschappen Proceedings Series B Physical Sciences **6**, 809 (1903).

[198] H. Daniel, *Elektrodynamik-Relativistische Physik*, Vol. 2 (Walter de Gruyter, 1997).

[199] D. J. Griffiths, "Electrodynamics", Introduction to Electrodynamics, 3rd ed., Prentice Hall, Upper Saddle River, New Jersey , 301 (1999).

[200] M. Eisenberg and R. Guy, "A proof of the hairy ball theorem", The American Mathematical Monthly **86**, 571 (1979).

[201] W. Martienssen and H. Warlimont, "Springer Handbook of Condensed Matter and Materials Data", Springer Handbook of Condensed Matter and Materials Data, Edited by W. Martienssen and H. Warlimont. 2005 XVIII, 1120 p. 1025 illus. With CD-ROM. 3-540-44376-2. Berlin: Springer, 2005. , 1025 (2005).

[202] T. Schumm, S. Hofferberth, L. M. Andersson, S. Wildermuth, S. Groth, I. Bar-Joseph, J. Schmiedmayer, and P. Krüger, "Matter-wave interferometry in a double well on an atom chip", Nature physics **1**, 57 (2005).

[203] Y. Hasegawa, R. Loidl, G. Badurek, M. Baron, and H. Rauch, "Violation of a Bell-like inequality in single-neutron interferometry", Nature **425**, 45 (2003).

[204] H. Lichte, "Gottfried Möllenstedt and his electron biprism: four decades of challenging and exciting electron physics", Microscopy **47**, 387 (1998).

[205] S. Wu, E. Su, and M. Prentiss, "Demonstration of an Area-Enclosing Guided-Atom Interferometer for Rotation Sensing", Phys. Rev. Lett. **99**, 173201 (2007).

[206] J. D. Jackson, *Classical electrodynamics* (John Wiley & Sons, 2012).

[207] F. Hasselbach, "Selected topics in charge particle interferometry", Scanning Microscopy **11**, 345 (1997).

[208] H. Zhang, J. Tang, J. Yuan, Y. Yamauchi, T. T. Suzuki, N. Shinya, K. Nakajima, and L.-C. Qin, "An ultrabright and monochromatic electron point source made of a LaB_6 nanowire", Nature nanotechnology **11**, 273 (2016).

Appended publications

Publication 1

Coherent properties of a tunable low-energy electron-matter-wave source

A. Pooch, M. Seidling, N. Kerker, R. Röpke, A. Rembold, W.T. Chang, I.S. Hwang and A. Stibor
Phys. Rev. A **97**, 013611 (2018)
doi: 10.1103/PhysRevA.97.013611

Coherent properties of a tunable low-energy electron-matter-wave source

A. Pooch,[1] M. Seidling,[1] N. Kerker,[1] R. Röpke,[1] A. Rembold,[1] W. T. Chang,[2] I. S. Hwang,[2] and A. Stibor[1,*]

[1]*Institute of Physics and Center for Collective Quantum Phenomena in LISA*$^+$*, University of Tübingen, Auf der Morgenstelle 15, 72076 Tübingen, Germany*

[2]*Institute of Physics, Academia Sinica, Nankang, Taipei 11529, Taiwan, Republic of China*

(Received 23 November 2017; published 12 January 2018)

A general challenge in various quantum experiments and applications is to develop suitable sources for coherent particles. In particular, recent progress in microscopy, interferometry, metrology, decoherence measurements, and chip-based applications rely on intensive, tunable, coherent sources for free low-energy electron-matter waves. In most cases, the electrons get field emitted from a metal nanotip, where its radius and geometry toward a counter electrode determines the field distribution and the emission voltage. A higher emission is often connected to faster electrons with smaller de Broglie wavelengths, requiring larger pattern magnification after matter-wave diffraction or interferometry. This can be prevented with a well-known setup consisting of two counter electrodes that allow independent setting of the beam intensity and velocity. However, it needs to be tested if the coherent properties of such a source are preserved after the acceleration and deceleration of the electrons. Here, we study the coherence of the beam in a biprism interferometer with a single atom tip electron field emitter if the particle velocity and wavelength varies after emission. With a Wien filter measurement and a contrast correlation analysis we demonstrate that the intensity of the source at a certain particle wavelength can be enhanced up to a factor of 6.4 without changing the transverse and longitudinal coherence of the electron beam. In addition, the energy width of the single atom tip emitter was measured to be 377 meV, corresponding to a longitudinal coherence length of 82 nm. The design has potential applications in interferometry, microscopy, and sensor technology.

DOI: 10.1103/PhysRevA.97.013611

I. INTRODUCTION

The quest to find the optimal particle source for a specific application in quantum physics has determined the progress in matter-wave experiments for atoms [1,2], neutrons [3], molecules [4,5], electrons [6,7], and ions [6,8]. New sources for free electron waves led to sophisticated recent developments in microscopy [9–13], laser-induced single-particle interference [14], or time-resolved dephasing measurements [15–17]. Particularly, to study the Coulomb-induced decoherence of an electron superposition close to a metallic, semi-, or superconducting surface [18–21], a source is desirable that allows the tuning of the electrons energy by remaining their coherence. The energy determines the velocity and therefore the interaction time of the quantum state with the environment. Most of the sources in interference experiments so far were etched metal tips with a diameter of several ten nanometers. By adding a monolayer of iridium or palladium the emission area can be reduced down to the size of a single atom at the end of a pyramidal atom stack (single atom tip (SAT) [22–24]). The electron-field emission follows the theory of Fowler and Nordheim [22,24,25] and the extraction voltage is determined by the properties of the tip, such as the material and the geometry, in relation to the distance and dimensions of a counter electrode. It is difficult to fabricate the geometry of a tip exactly on the nanometer scale, even if progress was made to control the tip profile during electrochemical etching [26]. As a result, individual tips have different extraction voltages for which the field emission will start, leading to varying intensity to velocity relations between different tips.

For that reason, in electron biprism interferometers the tip radius was manufactured as small as possible to get a low extraction voltage resulting in an intense and spatially coherent beam with a large electron wavelength. The electron emission signal was then enhanced by increasing the tip voltage. However, as a consequence, the resulting matter waves have larger energies and therefore shorter wavelengths, leading to smaller diffraction or interference fringes. Assuming a limited detection resolution and area, this in turn requires larger pattern magnification, which again reduces the signal. This problem can easily be addressed with a well-known technique used in electron microscopes by implementing two counter electrodes (apertures) behind the tip. They allow us to control the velocity (and wavelength) of the electrons independently to the emission intensity. By setting a low tip voltage in combination with a high first counter-electrode voltage relative to a second grounded aperture, a high emission intensity of slow electrons can be realized. However, this method was not applied in most biprism interferometers so far. The reason could be that it remains unclear how the lateral and longitudinal coherence of the particles are affected by accelerating and decelerating the particle, since the wavelength is not constant any more after emission. Therefore, in this geometry a combination of two factors influence the electrons. First, there is a position-dependent change of the electrons velocity leading to different wavelengths. And second, there is a lens effect of the electrodes.

*alexander.stibor@uni-tuebingen.de

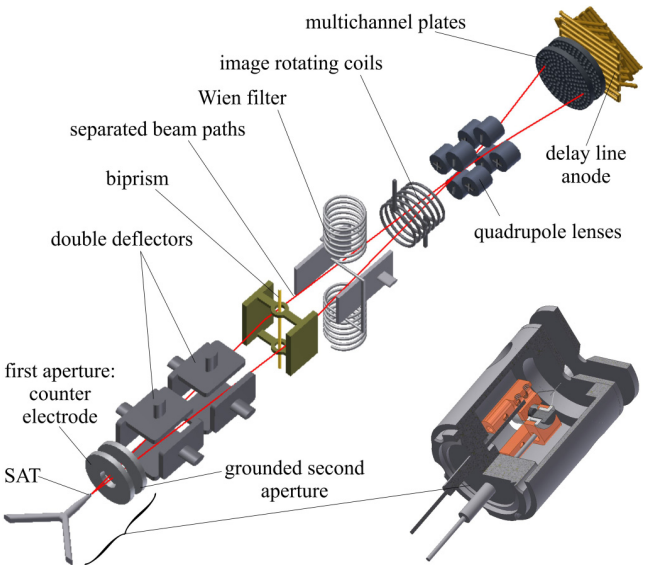

FIG. 1. Sketch of the experimental setup and the separated beam paths (red line) to measure the coherent properties of the single atom tip at different tip and counter-electrode settings and beam intensities in a biprism electron interferometer (not to scale). Inset: Mechanical drawing of the SAT field emission source realization in our setup with the two apertures (to scale).

In this article we describe such a beam source and test in a biprism electron interferometer how the lateral and longitudinal coherence of the particles are affected after tuning the intensity of the beam and keeping the wavelength constant behind the second aperture. We demonstrate with an iridium SAT that neither lens effects of the apertures nor the acceleration and deceleration of the electrons change their lateral coherence properties. Furthermore, the longitudinal coherence length and the energy spread of the emitted electrons are measured with a Wien filter [27]. These properties also remain unchanged. Our source allows us to increase the coherent low-energy electron emission by a factor of 6.4 at a constant matter wavelength, resulting in a constant interference contrast, pattern periodicity, and amount of fringes. The results have applications in matter-wave interferometry [6,24], in Aharonov-Bohm studies [28,29], decoherence measurements [18–21], electron-diffraction microscopy [11–13], time-resolved ultrafast electron diffraction [30], and for the development of a quantum electron microscope [9,10].

II. EXPERIMENT

A sketch of the experimental setup is illustrated in Fig. 1. The aim of the experiment is to increase the electron emission without changing the transversal and longitudinal coherence of the matter waves. The de Broglie wavelength, which is reciprocal to the particle velocity, should thereby be kept constant. This is possible with a configuration where the field emission tip, in our case a SAT [22–24], is set on a low negative potential U_{SAT} and a counter electrode is set on a positive potential U_c. Since only the field between these components is relevant for the emission process, the electron-beam intensity can be increased by raising the positive voltage of the counter electrode. In the following beam line, the electrons get decelerated by a second, grounded electrode to the low velocity corresponding to the electrical potential of the tip. Thereby, lower electron energies can be realized compared to the conventional high-voltage field emission directly to a grounded aperture. This is a well-known setup. However, it needs to be demonstrated that the longitudinal and transversal coherence of the beam is not reduced by the accelerating and decelerating process.

To study the coherent properties of this emitter setup, it is integrated in a biprism electron interferometer. It includes several beam optic parts from a former experiment by Sonnentag *et al.* [18]. The beam is adjusted by two double deflectors toward an electrostatic biprism. It consists out of a gold-palladium-coated glass fiber with a diameter of 400 nm [24] between two grounded electrodes. Just like the optical biprism for light, the electrostatic biprism separates coherently the electron waves from the emitter [6,31]. By applying a positive voltage U_f on the fiber, the biprism bends all beam paths by the same angle and combines them at the entrance of a magnifying quadrupole lens. The partial beams interfere and form a fringe pattern parallel to the biprism fiber. Directly after the biprism, the beam traverses a Wien filter, consisting of two opposing electrodes and two magnetic coils. As a result of the finite-energy spread of the emitted electrons, the separated partial waves can be described by matter-wave packages. The Wien filter allows us to shift them longitudinally relative to each other and to measure thereby the longitudinal coherence length of the beam [27]. To align the orientation of the fringes towards the magnifying axis of the quadrupole lens, an image rotating coil is positioned around the beam path behind the Wien filter. The interference pattern is magnified by two quadrupole lenses in the transverse direction normal to the biprism fiber with a magnification factor of several thousand. The electrons are amplified by two multichannel plates and detected with a delay line anode [32]. The position and point in time for every single electron event is recorded allowing a second-order correlation data analysis [15–17,33]. The red line in Fig. 1 illustrates a possible beam path according to the wave-particle duality. The whole setup is in an ultrahigh vacuum chamber at a pressure of $<5\times10^{-10}$ mbar and magnetically shielded by a mu-metal tube.

III. SIMULATION

For a detailed description of the electrical-field distribution between the tip, the counter electrode, and the second electrode, simulations with the program *Comsol* were performed. The results are illustrated in Fig. 2. Two cases were studied: first, the tip is set on a potential of -1600 V, the counter electrode on 200 V and the second aperture is grounded. This combination of voltages is used in most of our presented data. As can be seen in the cross section of Fig. 2(a) a 125-μm-thick tungsten wire is orientated horizontally at $y = 0$. Electrons with zero starting energy accelerate in x direction. As it is simulated in Fig. 2(b), those electrons passing the two apertures with 2.5-mm diameter keep moving on the optical axis and approach an energy of 1600 eV given by the tip potential. Due to computational reasons the tip radius in this geometry is set to be 2 μm, even if the actual physical tip radii are typically

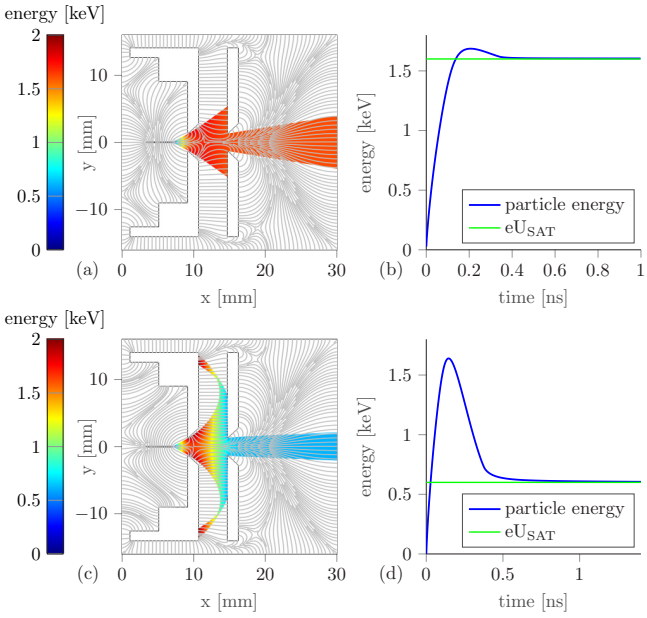

FIG. 2. (a) Simulation of the electrical-field distribution with a cross section of the cathode box geometry, including the tungsten tip and the two apertures. The tip defines the optical axis at $y = 0$. It is set on a potential of $U_{SAT} = -1600$ V and emits electrons with 0 eV starting energy. They accelerate in the electric field between the tip and the counter electrode, which is set on a voltage $U_c = 200$ V. The second aperture is grounded. The color bar represents the energy of the electrons. Also the electric field lines are shown in pale gray schematically. (b) The average energy of the electrons plotted versus time as they travel along the optical axis. They get accelerated by the first electrode and decelerated by the second, approaching the energy corresponding to the tip potential $eU_{SAT} = 1600$ eV. (c) Same geometry as in (a) with the settings $U_{SAT} = -600$ V and $U_c = 1378$ V. Some of the electron trajectories bend back onto the surface of the counter electrode. However, those electrons passing the second electrode end up at a significantly lower velocity compared to (a). (d) The acceleration and deceleration between the counter and second aperture is more distinct than in (b) leading to an electron energy of 600 eV.

around 50 nm. However, this does not change the results for the electric field lines further away from the tip. For the calculation of the electron trajectories the starting energy and direction of the emission is selected manually. The field emission itself could not be simulated, and thus the exact field strength at the tip surface is not relevant. Certainly, it increases with increasing counter electrode voltage U_c. Figure 2 also indicates that the coherent signal enhancement is not due to a lensing effect of the electron beam.

In the second case, simulated in Fig. 2(c), the tip is set on a low voltage of −600 V. To keep the relative potential high, 1378 V were applied on the counter electrode. This setting emerged to be the limit for creating interference fringes with minimal tip voltage in the experiment. In the simulations it leads to particle trajectories where electrons even get deflected back onto the counter electrode. The electrons close to the optical axis reach the final energy of only 600 eV in the interferometer with a corresponding large matter wavelength. As it will be verified in the next section, those slow electrons do not lose their coherent properties.

IV. RESULTS

For the characterization of the intensity enhancement and the coherent properties of our field-emission setup, we compared two situations. In the first one, the counter electrode is grounded and the tip voltage is increased. This is the usual operating mode in most biprism matter-wave interferometers so far [6]. The second case demonstrates our method for the coherent signal enhancement. Thereby, the tip is set on a fixed potential and the first counter electrode is varied such as simulated in the last section. In both cases the second electrode is grounded.

Figures 3(a) to 3(c) show the results for the first case. The tip voltage is increased stepwise starting at a negative tip voltage of $U_{SAT} = -1560$ V. The biprism voltage $U_{BP} = 0.331$ V is kept constant. This leads to a field emission toward the first and second apertures that are both grounded in these measurements. As expected and revealed in the inset of Fig. 3(a), the increase in signal behaves according to the Fowler-Nordheim theory, even though some signal is blocked by the apertures. In Fig. 3(b) the resulting fringe distances s after interference are shown for increasing tip voltages. They decrease due to the shorter matter wavelengths λ in combination with a lower quadrupole magnification at the higher electron energies. The fringe distances vary between $s = 2.59$ mm ($\lambda = 31.1$ pm) and $s = 1.89$ mm ($\lambda = 28.9$ pm) in Fig. 3(b). Figure 3(c) presents the interference contrast given after a second-order correlation analysis that reduces dephasing from the environment (noise from the electricity network, vibrations, slow fringe drifts, etc.) [15–17,33].

The results of our study for the second case are presented in Figs. 3(d) to 3(f). Here, the tip and the biprism are set on a fixed potential of $U_{SAT} = -1600$ V and $U_{BP} = 0.331$ V resulting in an electron-matter wavelength of 30.7 pm. The voltage of the first counter electrode is varied between $U_c = -119.7$ V and 199.7 V. The last value corresponds nearly to the simulation in Fig. 2(a). The second electrode is again grounded. The signal on the detector increases by a factor of ∼6.4 compared to the situation where no voltage is applied to the counter electrode [such as in Fig. 3(a)]. A linear behavior in a Fowler-Nordheim representation of the measured signal versus the potential difference between the SAT and the counter electrode can also be observed. However, the de Broglie wavelengths and particle velocities do not vary significantly, as it is expected according to our simulations and as it can be deduced from the constant fringe distance in Fig. 3(e). Furthermore, the interference contrast of around 50% in Fig. 3(f) does not change significantly, indicating constant transversal and longitudinal coherences. To perform a separate test of a possible variation of the transversal coherence length, the amount of visible fringes in the interference pattern were determined at the maximal and minimal first-aperture voltage. The corresponding correlation corrected [15–17,33] interference pattern are illustrated in Fig. 4. The amount of counted fringes, revealing the field of coherent superposition, does not change throughout these measurements, verifying a constant transversal coherent illumination of the biprism fiber.

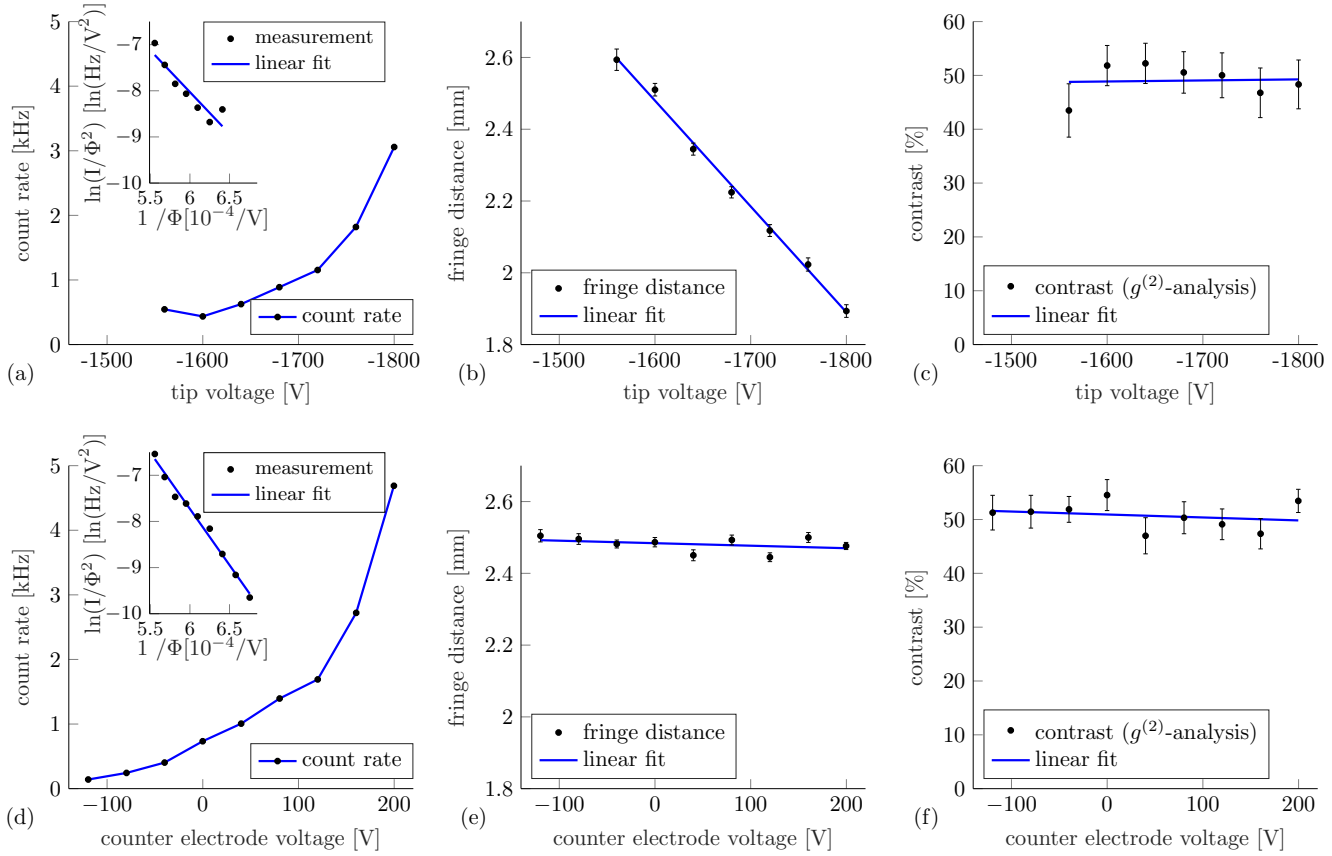

FIG. 3. Comparison of the behavior in count rate, fringe distance, and contrast between the increase of tip voltage toward a grounded counter electrode [(a) to (c)] and the application of a counter voltage to the first aperture [(d) to (f)]. (a) Count rate at the detector plane versus the tip field emission voltage. Inset: plot according to the Fowler-Nordheim relation, where Φ equals the tip voltage. (b) Decrease of the measured fringe distances due to the higher electron energies, resulting in shorter de Broglie wavelengths and lower quadrupole magnifications. (c) The determined dephasing corrected contrast remains constant in this range of tip voltages. (d) In contrast to (a) the count rate is determined as a function of the aperture voltage, keeping the tip voltage constant at -1600 V. Inset: plot according to the Fowler-Nordheim relation, where Φ equals the potential difference between the tip and the counter electrode. (e) The fringe distance does not change over all different aperture voltages due to the constant electron energy according to the simulations in Fig. 2(b). (f) Also, the interference contrast remains constant in the measurement region.

A possible change in longitudinal coherence for different voltages on the first aperture can be tested with the Wien filter [27]. Thereby, the measurements were conducted in the "matched mode", where the action of the electric field **E** from the Wien filter condensator cancels the one of the magnetic field **B** from the Wien coils along the optical beam axis. This "Wien condition" is fulfilled for $e\,\mathbf{E} + e\,(\mathbf{v} \times \mathbf{B}) = 0$, with the particle velocity **v**. By measuring the contrast change for different values of **E** and **B**, the longitudinal coherence length can be dertermined [27]. The tip and biprism voltages were kept constant at the same values as above ($U_{\mathrm{SAT}} = -1600\,\mathrm{V}$, $U_{\mathrm{BP}} = 0.331\,\mathrm{V}$). Starting from $+72$ V, the Wien condensator voltage was stepwise decreased to -99 V. At each step the current in the Wien coils was increased until the fringe pattern shifts back to the original position to assure the "matched mode". Then a signal of several 10^5 counts was recorded for the three different aperture voltages $U_c = 0\,\mathrm{V}$, 100.2 V, and 199.7 V, while only minimal phase shifts were noted from these changes of the settings. Subsequently, the average intensity along the fringe-direction was determined within a section of the spatial interference pattern. The resulting distribution was fitted with the model function $I(x) = I_0[1 + C\cos(\frac{2\pi x}{s} + \phi_0)]\mathrm{sinc}^2(\frac{2\pi x}{s_1} + \phi_1)$, according to a method described elsewhere [34]. Thereby, C is the interference contrast and s the fringe distance. The phases ϕ_0, ϕ_1, the average intensity I_0, and the width of the interference pattern s_1 are additional fitting parameters. The resulting contrast distributions are shown in Fig. 5. The data indicates that the contrast is significantly reduced by electromagnetic dephasing from the electricity network. Due to different count rates, the signal integration times were significantly longer for an aperture voltage of 0 V, leading to a stronger dephasing compared to 100.2 and 199.7 V. This causes a higher contrast loss. In fact, there is no contrast determinable at the 0 V aperture setting for Wien filter voltages higher than $\sim$30 V. For that reason, it is not possible to determine if the longitudinal coherence is preserved for different aperture voltages by the spatial interferences only. It was necessary to reveal and correct the dephasing by a second-order correlation analysis that includes the spatial and temporal differences of the electron

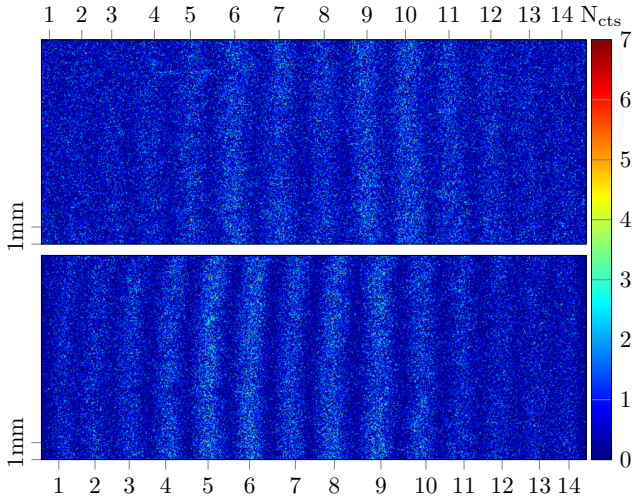

FIG. 4. Comparison of two interferograms with different voltages at the counter electrode $U_c = -119.7\,\mathrm{V}$ (top picture) and $U_c = +199.7\,\mathrm{V}$ (bottom picture), both at a fix tip voltage of $U_{\mathrm{SAT}} = -1600\,\mathrm{V}$. The interferograms exhibit the same amount of interference fringes (denoted by the number on the horizontal axis) and width of interference, revealing the transversal coherence of the interfering electrons is not influenced by the counter electrode voltage. A length scale is shown in the left bottom corner and the color bar represents the number of hits per pixel. Both pictures contain 3×10^5 counts and are dephasing corrected by second-order correlation analysis [15–17,33]. The undisturbed interference contrasts were thereby determined to be $51.3 \pm 3.2\,\%$ at $-119.7\,\mathrm{V}$ and $53.5 \pm 2.2\,\%$ at $+199.7\,\mathrm{V}$. The original uncorrected contrasts in the spatial pattern, determined by the model function described in the text, were $30.6 \pm 2.1\%$ and $33.9 \pm 2.2\%$, respectively.

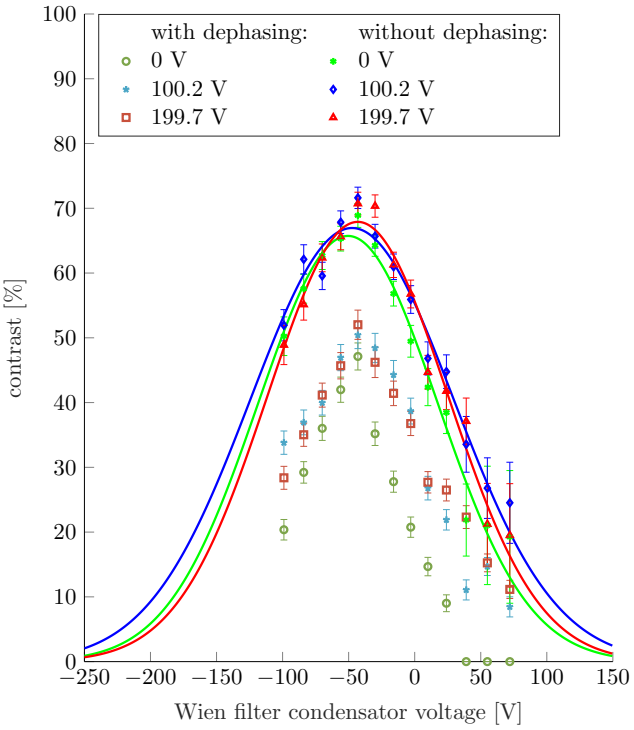

FIG. 5. Measurement of the interference contrast as a function of different Wien filter condensator voltages for a tip potential $U_{\mathrm{SAT}} = -1600\,\mathrm{V}$ and three different voltages for the first aperture ($U_c = 0\,\mathrm{V}$, 100.2 V, and 199.7 V). The determined contrast revealed by intensity evaluation of the spatial interference pattern is shown in green circles, blue stars, and red squares, respectively. The data is strongly dephased by the network frequency at 50 Hz. For that reason a $g^{(2)}$-correlation analysis using spatial and temporal differences of particle events at the detector [15–17,33] was applied, providing the unperturbed contrast distribution (green stars, blue diamonds, and red triangles). Gaussian fits to the data (green, blue, and red lines, corresponding to 0 V, 100.2 V, and 199.7 V, respectively) reveal comparable longitudinal coherence lengths with no significant variations for the different aperture voltages.

events at the delay line detector as described in detail elsewhere [15–17,33]. The resulting unperturbed contrast data is also plotted in Fig. 5, revealing contrast rates up to 71.6%. Thereby, a dephasing amplitude of $\sim 0.4\,\pi$ was determined. Three Gauss fits were applied to the data sets. According to Ref. [27] the coherence length l_c equals the longitudinal shift of the separated partial wave packages between two points where the contrast vanishes. This was defined to be the case when the contrast drops to 10% of its maximum value. The necessary voltage U_{cl} for this shift is connected to the width of the Gaussian fit σ by $U_{\mathrm{cl}} = \sqrt{2 \cdot \ln 10} \cdot \sigma$. For a given Wien filter condensator voltage U_{WF} the shift of the wave packets is calculated by $\Delta y = \frac{L}{2D} \frac{\Delta x}{U_{\mathrm{SAT}}} \cdot U_{\mathrm{WF}}$, where L is the length of the Wien filter condensator plates and D the distance between them. Δx denotes the distance between the separated beam paths at the center of the Wien filter [27]. It can be determined by $\Delta x = \Theta d_{\mathrm{WF-QP}}$, with $d_{\mathrm{WF-QP}}$ being the distance between the Wien filter and the quadrupole and the superposition angle Θ which can be calculated by the applied voltages U_{SAT} and U_{BP} [34,35]. The resulting data reveal longitudinal coherence lengths of 82 ± 9 nm for 0 V on the first aperture, 93 ± 10 nm for 100.2 V, and 82 ± 8 nm for 199.7 V. The energy widths of the emitted beams can be determined by $\Delta E = \frac{2U_{\mathrm{SAT}}\lambda}{\pi l_c}$. This leads to energy widths of 377 ± 40 meV, 334 ± 37 meV, and 377 ± 35 meV, respectively. Our results are in good agreement with the literature value for the energy spread of SAT field emitters of 0.4 eV [36]. The consistency within the error bars of the longitudinal coherence lengths for different aperture voltages verifies our conclusion that the coherent beam properties are not affected by our method of intensity enhancement.

Several applications in microscopy, interferometry, or sensor technology require slow coherent electrons [11–13]. Our method can generate such matter waves with energies that are significantly lower than for typical field emission tips. To test the limits of the technique in our setup, we reduced the tip voltage to the values simulated in Figs. 2(c) and 2(d). Thereby, the tip voltage was set to -600 V were no emission is observed with a grounded counter electrode, since it is significantly lower than the minimal extraction voltage of the SAT. However, in combination with an aperture voltage of 1378 V a reasonable count rate of 1138 ± 2 Hz after magnification was detected. The energy of the particles corresponds to a de Broglie wavelength of 50 pm. The slower the electrons are, the more susceptible they are for dephasing by external oscillations. This can also be observed in the deduced interference contrast of

19.8 ± 1 % from the spatial integrated image compared to the determined contrast after correlation analysis of 37.7 ± 3 %. For the same reason a larger dephasing amplitude of $\sim 0.435\,\pi$ was determined. The measured pattern periodicity on the detector was 9.0 ± 0.3 mm. From a comparison with the theoretical value at the entrance of the quadrupole before magnification of 928 nm, we deduce a magnification factor of 9730 ± 290.

V. CONCLUSION

We demonstrated in an electron biprism matter-wave interferometer that the coherent properties of a beam are not affected by accelerating and decelerating the electrons or the associated lens effects. As a result, it was possible to increase the signal by a factor of 6.4 at a certain matter wavelength while remaining full transversal and longitudinal coherence. It was realized by a simple design known from electron microscopy, installing a field emission tip in combination with two counter electrodes. Thereby, a single atom tip is set on a voltage well below its minimal extraction voltage. Field emission is initiated by the application of a positive voltage on a counter electrode. The second electrode is grounded and decelerates the electrons to the energy corresponding to the low tip potential. This is also verified in particle beam simulations. By measurement of the interference pattern periodicity, amount of fringes, and interference contrast, it could be demonstrated that the velocity and transversal coherence of the electrons are kept constant with increasing first-aperture voltage and signal intensity. Additionally, it was also possible to determine the energy width of the single-atom tip emitter to be 377 ± 40 meV for 0 V on the first aperture. It corresponds to a longitudinal coherence length of 82 ± 9 nm and does not change significantly for different counter aperture voltages. The experiment also showed that slow electrons are susceptible to external dephasing perturbations. For that reason, it was required to remove the significant dephasing from the 50 Hz electricity network by a correlation analysis [15–17,33].

The method also enabled the generation of slow coherent electrons with energies significantly lower than the ones corresponding to the minimum extraction voltage of the tip. We demonstrated this by interfering electrons with 600 eV and a counter-electrode voltage of 1378 V, still revealing a large contrast of 37.7 ± 3 %. Our technique is of relevance in all applications where an intense beam of tunable, slow, and coherent electrons is required such as for microwave chip-based designs [37], electron diffraction microscopy [11–13], sensitive sensors for inertial forces [38], vibrational [17] or electromagnetic [16] dephasing, and decoherence studies [18–21].

ACKNOWLEDGMENTS

This work was supported by the Deutsche Forschungsgemeinschaft through the research Grant No. STI 615/3-1 and the Vector Stiftung. A.S. acknowledges support from the Bridging Fund of the University of Tübingen and A.R. from the Evangelisches Studienwerk e.V. Villigst.

[1] A. D. Cronin, J. Schmiedmayer, and D. E. Pritchard, Rev. Mod. Phys. **81**, 1051 (2009).
[2] J. R. Anglin and W. Ketterle, Nature **416**, 211 (2002).
[3] H. Rauch and S. A. Werner, *Neutron Interferometry: Lessons in Experimental Quantum Mechanics, Wave-particle Duality, and Entanglement*, Vol. 12 (Oxford University Press, Oxford, 2015).
[4] K. Hornberger, S. Gerlich, P. Haslinger, S. Nimmrichter, and M. Arndt, Rev. Mod. Phys. **84**, 157 (2012).
[5] T. Juffmann, H. Ulbricht, and M. Arndt, Rep. Prog. Phys. **76**, 086402 (2013).
[6] F. Hasselbach, Rep. Prog. Phys. **73**, 016101 (2010).
[7] H. Batelaan, Rev. Mod. Phys. **79**, 929 (2007).
[8] F. Hasselbach and U. Maier, in *Proceedings of ISQM'98, Tokyo*, edited by Y. A. Ono and K. Fujikawa (Elsevier, Amsterdam, 1999), p. 299.
[9] W. P. Putnam and M. F. Yanik, Phys. Rev. A **80**, 040902(R) (2009).
[10] P. Kruit, R. G. Hobbs, C.-S. Kim *et al.*, Ultramicroscopy **164**, 31 (2016).
[11] I.-S. Hwang, W.-T. Chang, C.-Y. Lin, W.-H. Hsu, Microsc. Microanal. **21**, 839 (2015).
[12] T. Latychevskaia, W.-H. Hsu, W.-T. Chang, C.-Y. Lin, and I.-S. Hwang, Nat. Commun. **8**, 14440 (2017).
[13] J.-N. Longchamp, T. Latychevskaia, C. Escher, and H.-W. Fink, Appl. Phys. Lett. **107**, 133101 (2015).
[14] D. Ehberger, J. Hammer, M. Eisele, M. Krüger, J. Noe, A. Högele, and P. Hommelhoff, Phys. Rev. Lett. **114**, 227601 (2015).
[15] A. Rembold, G. Schütz, W. T. Chang, A. Stefanov, A. Pooch, I. S. Hwang, A. Günther, and A. Stibor, Phys. Rev. A **89**, 033635 (2014).
[16] A. Günther, A. Rembold, G. Schütz, and A. Stibor, Phys. Rev. A **92**, 053607 (2015).
[17] A. Rembold, G. Schütz, R. Röpke, W.-T. Chang, I.-S. Hwang, A. Günther, and A. Stibor, New J. Phys. **19**, 033009 (2017).
[18] P. Sonnentag and F. Hasselbach, Phys. Rev. Lett. **98**, 200402 (2007).
[19] P. Machnikowski, Phys. Rev. B **73**, 155109 (2006).
[20] S. Scheel and S. Y. Buhmann, Phys. Rev. A **85**, 030101(R) (2012).
[21] J. R. Anglin, J. P. Paz, and W. H. Zurek, Phys. Rev. A **55**, 4041 (1997).
[22] H.-S. Kuo, I.-S. Hwang, T.-Y. Fu, Y.-C. Lin, C.-C. Chang, and T.-T. Tsong, Jpn. J. Appl. Phys. **45**, 8972 (2006).
[23] H.-S. Kuo, I.-S. Hwang, T.-Y. Fu, Y.-H. Lu, C.-Y. Lin, and T.-T. Tsong, Appl. Phys. Lett. **92**, 063106 (2008).
[24] G. Schütz, A. Rembold, A. Pooch, S. Meier, P. Schneeweiss, A. Rauschenbeutel, A. Günther, W. T. Chang, I. S. Hwang, and A. Stibor, Ultramicroscopy **141**, 9 (2014).
[25] R. Fowler and L. Nordheim, Proc. R. Soc. London A **119**, 173 (1928).
[26] W.-T. Chang, I.-S. Hwang, M.-T. Chang *et al.*, Rev. Sci. Instrum. **83**, 083704 (2012).
[27] M. Nicklaus and F. Hasselbach, Phys. Rev. A **48**, 152 (1993).
[28] Y. Aharonov and D. Bohm, Phys. Rev. **115**, 485 (1959).

[29] G. Schütz, A. Rembold, A. Pooch, H. Prochel, and A. Stibor, Ultramicroscopy **158**, 65 (2015).
[30] M. Gulde, S. Schweda, G. Storeck, M. Maiti, H. K. Yu, A. M. Wodtke, S. Schäfer, and C. Ropers, Science **345**, 200 (2014).
[31] G. Möllenstedt and H. Düker, Z. Phys. A **145**, 377 (1956).
[32] O. Jagutzki, V. Mergel, K. Ullmann-Pfleger, L. Spielberger, U. Spillmann, R. Dörner, and H. Schmidt-Böcking, Nucl. Instrum. Methods Phys. Res., Sect. A **477**, 244 (2002).
[33] A. Rembold, R. Röpke, G. Schütz, J. Fortágh, A. Stibor, and A. Günther, New J. Phys. **19**, 103029 (2017).
[34] A. Pooch, M. Seidling, M. Layer, A. Rembold, and A. Stibor, Appl. Phys. Lett. **110**, 223108 (2017).
[35] F. Lenz and G. Wohland, Optik **67**, 315 (1984).
[36] E. Rokuta, H.-S. Kuo, T. Itagaki, K. Nomura, T. Ishikawa, B.-L. Cho, I. S. Hwang, T. T. Tsong, and C. Oshima, Surf. Sci. **602**, 2508 (2008).
[37] J. Hammer, S. Thomas, P. Weber, and P. Hommelhoff, Phys. Rev. Lett. **114**, 254801 (2015).
[38] F. Hasselbach and M. Nicklaus, Phys. Rev. A **48**, 143 (1993).

Publication 2

A compact electron matter wave interferometer for sensor technology

A. Pooch, M. Seidling, M. Layer, A. Rembold and A. Stibor
Appl. Phys. Lett. **110**, 223108 (2017)
doi: 10.1063/1.4984839

A compact electron matter wave interferometer for sensor technology

A. Pooch, M. Seidling, M. Layer, A. Rembold, and A. Stibor
Institute of Physics and Center for Collective Quantum Phenomena in LISA$^+$, University of Tübingen, Auf der Morgenstelle 15, 72076 Tübingen, Germany

(Received 28 March 2017; accepted 18 May 2017; published online 1 June 2017)

Remarkable progress can be observed in recent years in the controlled emission, guiding, and detection of coherent, free electrons. Those methods were applied in matter wave interferometers leading to high phase sensitivities and precise sensor technologies for dephasing influences such as mechanical vibrations or electromagnetic frequencies. However, the previous devices have been large laboratory setups. For future sensor applications or tests of the coherence properties of an electron source, small, portable interferometers are required. Here, we demonstrate a compact biprism electron interferometer that can be used for mobile applications. The design was optimized for small dimensions by beam path simulations. The interferometer has a length between the tip and the superposition plane before magnification of only 47 mm and provides electron interference patterns with a contrast up to 42.7%. The detection of two dephasing frequencies at 50 and 150 Hz was demonstrated applying second order correlation and Fourier analysis of the interference data. *Published by AIP Publishing.* [http://dx.doi.org/10.1063/1.4984839]

Matter wave interferometers for electrons[1–4] have significantly improved in the last few decades. They are applied to measure the rotational phase shift due to the Sagnac effect[5] and to study Coulomb-induced quantum decoherence,[6,7] the magnetic Aharonov-Bohm effect,[8–11] or the Talbot-Lau effect for magnetic field sensing.[12] The topic is influenced by recent technical innovations and improvements concerning the beam source,[13–15] the precise electron guiding,[3,16] the coherent beam path separation,[4,14,17,18] and the development of spatial and temporal single-particle detection methods.[19–22] The progress has potential applications in electron microscopy[23,24] and sensor technology for inertial forces,[25] mechanical vibrations,[21] and electromagnetic frequencies.[19,20]

Small deviations of the partial waves in the two separated beam paths in a matter wave interferometer lead to a clear phase shift on the detector after they get superposed. This simple feature makes interferometric measurements extremely sensitive towards external perturbations. In contrast to neutral atoms, the phase of electron matter waves can be shifted not only by mechanical vibrations, temperature drifts, or rotations of the setup but also by external electromagnetic frequencies. Usually, these perturbations lead to a time dependent dephasing, causing a "wash-out" of the temporally integrated interference pattern that can be observed in a reduced interference contrast. This is particularly a challenge for sensitive long-time phase measurements such as proposed for the measurement of the electric Aharonov-Bohm effect,[26] decoherence measurements,[7] or the interferometry of ions.[27,28]

We recently demonstrated in a biprism electron interferometer[4] that such dephasing effects can on the one hand be corrected and on the other hand used for an accurate measurement of the perturbation frequencies.[20,21] Thereby, the dephasing was detected and reduced with the high spatial and temporal single-particle resolution of a delay line detector.[22] A second-order correlation analysis in combination with a Fourier analysis was performed on the detection events after the interference was recorded. It can reveal multifrequency electromagnetic oscillations and mechanical vibrations. The spectrum of the unknown external frequencies, their amplitudes, the interference contrast, and the pattern periodicity can be extracted from a spatially "washed-out" pattern.[19–21] For that reason, electron matter wave interferometers have a high potential in sensor technology. However, due to their large dimensions, current experimental setups are not suitable for portable sensor applications.[2–4] To apply an electron interferometer as a sensor for electromagnetic and vibrational frequencies or for the mobile analysis of the coherence of a beam source, it is necessary to construct a small and transportable device.

In this article, we present a compact biprism matter wave interferometer for free electrons with minimized distances between all parts and a high mechanical stability. The distance between the tip and the superposition plane before magnification is only 47 mm including all components for beam guiding and diffraction. In combination with the recently developed tools for spectrum analysis by correlation theory,[19–21] the compact setup is an important prerequisite for a portable, mobile sensor based on matter wave interferometry with electrons.

The setup of the biprism interferometer is illustrated in Fig. 1. The source for coherent electrons is a field emission tip that can be prepared by pulsed etching of a polycrystalline tungsten wire.[29] The beam gets aligned by two deflection electrodes to coherently illuminate a biprism fiber. It acts as a beam splitter for the electron matter waves, if a small positive voltage is applied on the fiber. The electric force bends the separated beam paths towards each other and superimposes them in front of a magnifying quadrupole lens. The key feature of the electron biprism, analogue to the optical biprism, is that all possible beam paths get deflected by the same angle, leading to a common angle of superposition at the entrance of the quadrupole.[2] The superposition of the

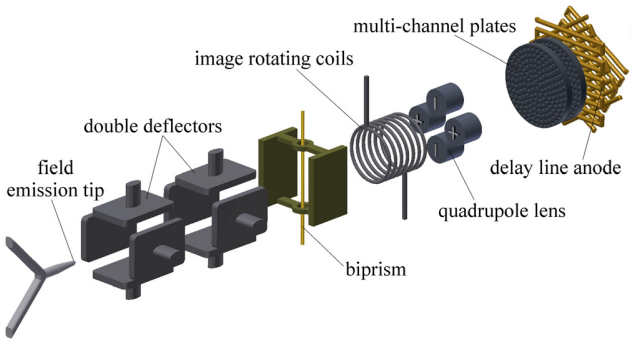

FIG. 1. Sketch of the compact biprism electron interferometer (not to scale). The coherent electron beam is field emitted by a tungsten tip and guided by double deflectors. A biprism fiber separates and combines the partial matter waves that interfere at the entrance of a magnifying quadrupole. An image rotating coil can rotate the resulting pattern for alignment. The magnified interferogram is amplified by two multi-channel plates and detected by a delay line detector.

two partial beams leads to an interference pattern parallel to the biprism fiber. The interferogram has a typical pattern periodicity of several hundred nanometers and needs to be magnified by the quadrupole lens to fit the spatial resolution of the multi-channel plate (MCP) detector. Such lenses are optimal suited for biprism interferometry since it is only necessary to magnify the pattern in the direction normal to the interferences. A small misalignment of the biprism fiber towards the magnifying axis can be corrected by an image rotating coil. In our experiment, a drift distance of 170 mm between the exit aperture of the quadrupole lens and the MCPs of the detector was chosen. The electron signal gets amplified by the MCP and detected by a hexagonal delay line (Roentdek, model DLD40X) with a spatial and temporal resolution of $\sim$100 μm and $\sim$0.1 ns.

An image of the interferometer is shown in Figs. 2(a) and 2(b). The whole setup is fixed between two grounded copper half-shells with a length of 87 mm and an outer diameter of 36 mm. They make the setup extremely rigid against mechanical vibrations and ensure alignment of the parts. After attachment of the two shells, most components are automatically well centered towards the optical axis. Only the tip cannot be prepared exactly in the middle, due to the mounting and etching procedure. For that reason, the tip holder is aligned during installation by four screws attached to the shells. Further beam alignment towards the optical axis is performed during operation by the double deflectors. Some individual parts are identical or based on constructions used in interferometers by Hasselbach.[1,3] The field emission

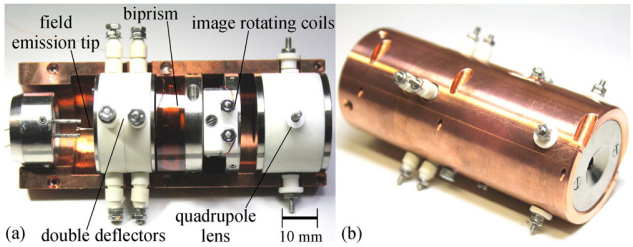

FIG. 2. (a) Image of the components in the beam path from the tip to the quadrupole with the upper copper shell removed. (b) Interferometer parts from the tip to the quadrupole mounted together within both half-shells.

tungsten tip is spot welded on a commercial holder and has a typical radius between 10 nm and 50 nm. The length of the tip profile and the radius can be controlled by the parameters in the etching process.[29] The tip is positioned 1 mm in front of an aperture of 2 mm diameter acting as a grounded counter electrode. Its distance to the biprism is $a = 19$ mm and to the entrance of the quadrupole lens $b = 28$ mm. The tip emits electrons with an acceleration voltage of $U_e = 2250$ V into a double deflector module, consisting of four pairs of flat deflection electrodes with a length of 5 mm and oriented around the beam with a distance of 5.5 mm between them. The positive and negative voltage applied between two opposing electrode pairs is equal to keep a zero potential on the beam axis. The biprism fiber consists of a glass fiber with a diameter of 400 nm that was manufactured by a special procedure described elsewhere.[4,30,31] It is coated with a gold-palladium alloy to ensure a smooth, conductive surface and is glued on a holder isolated by a non-conductive foil. The fiber is positioned between two grounded titanium electrodes that are 4 mm apart from each other. The rotating coil is winded around a 7 mm-diameter tube. The quadrupole lens is made out of four opposing cylindrical electrodes with a length of 10 mm, a diameter of 7.6 mm, and a distance normal to the beam path towards each other of 6.7 mm. As for the double deflectors, the electrodes are mounted within insulating holders made out of MACOR. It is important that the insulators are far away from the beam to avoid charging effects. An aperture with a diameter of 4 mm is positioned at the entrance and exit of the quadrupole lens to decrease the amount of secondary stray electrons on the detector. The interferometer is magnetically shielded by a mu-metal tube and in a vacuum chamber at $\sim 5 \times 10^{-10}$ mbar to ensure a long lifetime and stable emission of the tip.[32]

The aim of the design was to be as compact as possible along the beam axis. The necessary distance to provide a reasonable coherent illumination on the biprism can be calculated by the angular coherence relation and is determined by the effective source radius, with typical values for tungsten field emitters of $\sim$1 nm.[14,18] This consideration leads to a minimal tip-biprism distance a of $\sim$300 μm, in consistence with interference experiments with (smaller) nanotubes and tip-tube separations of several hundred nanometers.[14,17] In the current design, a had to be larger to allow the installation of the double deflectors and two 2 mm-apertures for a defined counter electrode and a reduction of stray electrons.

The distance b between the biprism and the superposition plane at the quadrupole entrance turns out to be more restrictive concerning the compactness of the device. It cannot be arbitrary small since it influences the superposition angle. A large angle will lead to a small pattern periodicity that needs to be sufficiently magnified. The biprism fiber with an applied voltage U_f deviates the beam paths by the angle $\gamma = \frac{\pi}{2\ln(R/r)}\frac{U_f}{U_e}$, with the radius r of the fiber and the distance R from the fiber to the grounded electrodes.[2,34] Geometrical considerations lead to $b = \frac{a(2\gamma-\theta)}{\theta}$, with the superposition angle θ, that depends on the de Broglie wavelength λ and the pattern periodicity s_0 : $\theta = \frac{\lambda_{dB}}{s_0}$.[34] The compact design is limited by electric insulation and arching,

since a large pattern magnification requires high voltages on the quadrupoles. Smaller dimensions such as in microelectromechanical system (MEMS) technology[39,40] could decrease the necessary voltages and allow for a more accurate alignment of the lenses and deflectors. This would require a new biprism micro-holder and a 3D-nanopositioning unit to adjust the tip.

With this device, it was possible to observe high contrast electron interference patterns such as shown in Fig. 3(a) for 5×10^5 detected particles. The temporal and spatial information of every detection event was recorded for a correlation analysis after data acquisition. The small bend in the middle of the pattern in Fig. 3(a) is due to a deviation of the beam from the optical axis in the quadrupole lens. It can be corrected by a fourth degree polynomial fit on the fringes and subsequent straightening. The resulting pattern in the marked red rectangle (7 mm × 32 mm) is exhibited in Fig. 3(b). Thus, nine fringes are visible in the image. The color bar indicates the intensity distribution of the incoming particles. In Fig. 3(c), the average intensity along the y-direction is plotted against the distance x on the screen. The distribution is enfolded by a *sinc*-function due to the similarity to the double slit experiment analysis.[33] Therefore, the data in Fig. 3(c) were fitted with the model function $I(x) = I_0 \cdot (1 + K_m \cdot \cos(\frac{2\pi x}{s_m} + \phi_0)) \cdot \mathrm{sinc}^2(\frac{2\pi x}{s_1} + \phi_1)$ revealing a contrast $K_m = (37.2 \pm 5)\%$ and the fringe distance $s_m = (0.85 \pm 0.02)$ mm. The phases ϕ_0, ϕ_1, the average intensity I_0, and the width of the interference pattern s_1 are additional fitting parameters. The magnification of the interferogram in Fig. 3(a) is 2517 ± 6. It is given by the determined fringe distance s_m on the detector after magnification divided by the theoretical fringe distance $s_0 = 338$ nm at the entrance of the quadrupole, which is calculated with the equations given above.[34]

We additionally performed beam path simulations with the program *Simion* (Version 8.1, Scient. Instr. Serv. Inc.). The superposition angle was extracted from the simulation by a method described in Ref. 26. It is known that contact potentials between the gold/palladium coating of the fiber and the titanium electrodes influence the effective potential interacting with the separated beams.[35,36] For that reason, we adapted the biprism voltage until nine interference stripes fit in the superposition area. This is achieved by adding 0.69 V in the simulation to the experimentally applied voltage of 0.559 V. This extra voltage is considered to be the contact potential and agrees well comparing the literature values for the work functions of the averaged 80:20% gold/palladium alloy and the one of titanium.[37] Their difference amounts to 0.71 eV. Our simulations revealed a superposition angle of 7×10^{-5} rad and a pattern periodicity of 369 nm before magnification. The quadrupole magnification was simulated to be 2886, which can be considered as an upper bound for perfect beam alignment on the optical axis. The reasonable small variations to the theoretical fringe distance s_0 and magnification are possibly due to the neglected beam adjustment voltages and small deviations between the simulated and experimental setup distances.

As recently demonstrated[20,21] and discussed above, contrast reducing dephasing effects, such as electromagnetic oscillations or mechanical vibrations, can be isolated and corrected by a second-order correlation analysis of the measured interference pattern. We applied this method, described in detail elsewhere,[20,21,38] to the interference data in Fig. 3(b). The analysis provides the second-order correlation function $g^{(2)}(u, \tau)$ with the correlation length u and correlation time τ between the detected particles. Consequentially, we can determine the fringe distance s_g and the contrast K_g of the unperturbed interference pattern at the temporal position $\tau = 0$, $g^{(2)}(u, 0)$, as shown in Fig. 4(a). The red curve is a fit function $g^{(2)}(u, 0) = 1 + \frac{K_g^2}{2} \cdot \cos(\frac{2\pi u}{s_g} + \phi_g) + O$ with the fit parameters contrast K_g, the fringe distance s_g, the phase ϕ_g

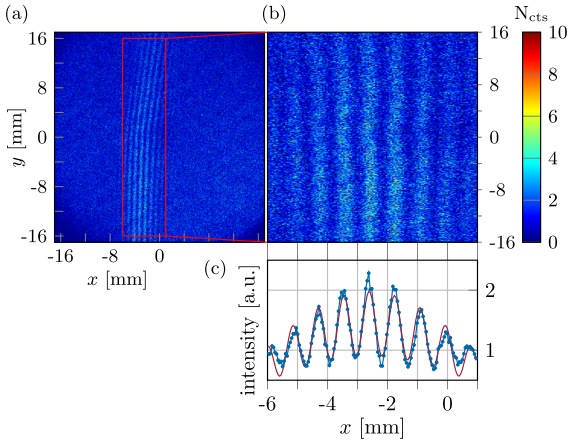

FIG. 3. (a) Image of the interference pattern on the detector screen with the set experimental values $U_e = 2250$ V, $U_f = (0.559 + 0.69)$ V and quadrupole voltages +2960 V between the electrodes normal to the fringes and −2910 V parallel to them. (b) Focus of the region within the red rectangle where the fringes were straightened by a fourth degree polynomial. (c) Blue curve: average intensity along the y-direction on the screen. Red curve: numerical fit of the intensity.

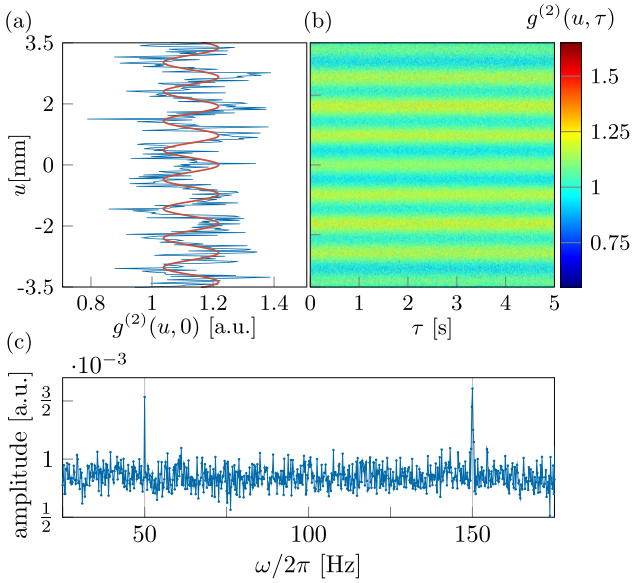

FIG. 4. (a) Blue line: the second-order correlation function $g^{(2)}(u, 0)$ at the correlation time $\tau = 0$. Red curve: fit function to reveal the contrast and the pattern periodicity. (b) The second-order correlation function $g^{(2)}(u, \tau)$ for τ ranging between 0 and 5 s. $g^{(2)}(u, \tau)$ is extracted from the data in Fig. 3(b). The periodic fringe pattern is clearly observable. (c) Plot of the amplitude spectrum calculated via a numerical Fourier transformation of $g^{(2)}(u = M_u \cdot s_g/2, \tau), M_u \in \mathrm{N}_0$ and subsequent averaging. Periodic perturbations of the interference fringes in time become visible and identify two characteristic frequencies at 50 Hz and 150 Hz.

and the offset O.[38] We obtain $s_g = (0.84 \pm 0.02)$ mm and $K_g = (42.5 \pm 7)\%$. The contrast K_g is higher than K_m suggesting that disturbing effects may wash-out the interference pattern. The significant high standard deviations for both values are due to a limited number of detected particles and therefore a large noise. In Fig. 4(b), $g^{(2)}(u, \tau)$ is shown for correlation times up to 5 s. Along the u-axis, the unperturbed fringe pattern with a distance s_g can be observed. The amplitude spectrum of the correlation function, $|\mathcal{F}(g^{(2)}(u,\tau))(u,\omega)|$, reveals the perturbation characteristics. It is determined using a numerical temporal Fourier transformation at the spatial positions $(u = M_u \cdot s_g/2, \tau, M_u \in \mathbb{N}_0)$, where the correlation function has its maximum signal.[21,38] In Fig. 4(c), the average over all amplitude spectra calculated at the spatial positions $u = M_u \cdot s_g/2$ is plotted. For optimal settings of the spatial and temporal discretization step size of the numerical correlation function,[38] two clear peaks at 50 Hz and 150 Hz evolve. These frequencies affect the electron waves and lead to unwanted contrast loss. Their spatial perturbation amplitude before the magnification can be determined according to the description in Ref. 21 to 14.3 nm at 50 Hz and 14.8 nm at 150 Hz. Thereby, it is assumed that the perturbation takes place before magnification, which is reasonable since the amplitudes are low. They probably originate from the utility frequency of the electrical power supplies. Their detection demonstrates the usability of our device as a sensor for external perturbation frequencies.

For further characterization of the compact interferometer, we present a series of measurements with variable voltages U_f at the biprism fiber, going from $(0.051 + 0.69)$ V to $(0.900 + 0.69)$ V in ~50 mV steps. With those sixteen data files, the same analysis is executed as described above. The data are shown in Fig. 5, whereas U_f is plotted against both the fringe distance and the contrast. The values for s_g and K_g refer to the unperturbed case originating from the second-order correlation analysis. As expected from theory,[34] the fringe distance decreases with increasing biprism voltage, since the superposition angle of the partial waves increases. This is observed for both s_m and s_g leading to nearly the same results. The contrast K_m increases up to ~38% at ~1 V biprism voltage. For lower voltages K_m decreases due to

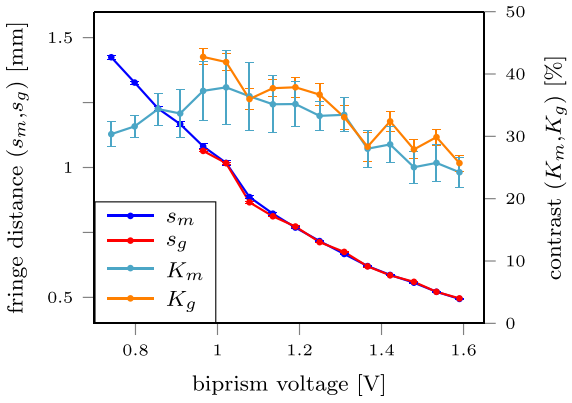

FIG. 5. Fringe distances s_m and s_g together with the interference contrasts K_m and K_g as a function of the biprism voltage. The data are evaluated by spatial integration and correlation analysis. The error bars for s_m and s_g are smaller than the dot size. K_m is in most cases lower than K_g due to the influence of the detected dephasing perturbations.

diffraction effects at the edge of the fiber. For higher voltages, a reduced contrast is expected due to coherence considerations with a beam source of finite extent.[28,34] K_g reveals a similar curve progression with a maximum of 42.7%. As expected, the contrast K_g is at most voltages higher than the contrast K_m disturbed by the two dephasing frequencies. The first four measurements of K_g cannot be evaluated with the $g^{(2)}$ analysis because of the influence of diffraction. It is not included in the theory of the $g^{(2)}$ analysis and significant for small biprism voltages.

We demonstrated a compact biprism matter wave interferometer for free electrons providing interference fringes with a contrast up to 42.7%. The dimension and the robustness of the setup are sufficient to be integrated in a mobile device. The interference data were recorded by a delay line detector with a high spatial and temporal single-particle resolution. This allowed a second-order correlation and Fourier analysis revealing the undisturbed contrast and the pattern periodicity of the interferogram. It was compared to the values obtained by pure spatial signal integration. Our device allowed the identification of dephasing frequencies at 50 Hz and 150 Hz and therefore demonstrated its applicability for the detection of external perturbations with the recently developed second-order correlation data analysis.[19–21,38] Identifying dephasing oscillations from the lab environment is a very helpful tool to improve experiments for sensitive phase measurements. The setup can also be applied to test the coherence of beam sources.[14,15] In particular, the simple design and the small dimensions make the interferometer easy to handle and usable in various environments. The sensitivity towards vibrational or electromagnetic dephasing and inertial forces such as rotation and acceleration could be increased significantly with a larger beam path separation. This would require an interferometer scheme with two or three biprism fibers in combination with a quadrupole or an einzel-lens.[5,25,26]

This work was supported by the Vector Stiftung and the Deutsche Forschungsgemeinschaft through the Emmy Noether Program No. STI 615/1-1, the Grant Nos. STI 615/3-1 and STI 615/5-1. A.S. acknowledges support from the Bridging Fund of the University of Tübingen and A.R. from the Evangelisches Studienwerk e.V. Villigst. We thank N. Kerker, R. Röpke, and G. Schütz for helpful discussions.

[1]F. Hasselbach, Rep. Prog. Phys. **73**, 016101 (2010).
[2]G. Möllenstedt and H. Düker, Z. Phys. A - Hadrons Nucl. **145**, 377 (1956).
[3]F. Hasselbach, Z. Phys. B **71**, 443 (1988).
[4]G. Schütz, A. Rembold, A. Pooch, S. Meier, P. Schneeweiss, A. Rauschenbeutel, A. Günther, W. T. Chang, I. S. Hwang, and A. Stibor, Ultramicroscopy **141**, 9 (2014).
[5]F. Hasselbach and M. Nicklaus, PRA **48**, 143 (1993).
[6]W. H. Zurek, Rev. Mod. Phys. **75**, 715 (2003).
[7]P. Sonnentag and F. Hasselbach, PRL **98**, 200402 (2007).
[8]Y. Aharonov and D. Bohm, Phys. Rev. **115**, 485 (1959).
[9]G. Möllenstedt and W. Bayh, Phys. Blätter **18**, 299 (1962).
[10]A. Tonomura, N. Osakabe, T. Matsuda, T. Kawasaki, J. Endo, S. Yano, and H. Yamada, PRL **56**, 792 (1986).
[11]R. G. Chambers, PRL **5**, 3 (1960).
[12]R. Bach, G. Gronniger, and H. Batelaan, Appl. Phys. Lett. **103**, 254102 (2013).
[13]H. S. Kuo, I. S. Hwang, T. Y. Fu, Y. C. Lin, C. C. Chang, and T. T. Tsong, Jpn. J. Appl. Phys. **45**, 8972 (2006).

[14]D. Ehberger, J. Hammer, M. Eisele, M. Krüger, J. Noe, A. Högele, and P. Hommelhoff, PRL **114**, 227601 (2015).
[15]P. Hommelhoff, Y. Sortais, A. Aghajani-Talesh, and M. A. Kasevich, PRL **96**, 077401 (2006).
[16]J. Hammer, J. Hoffrogge, S. Heinrich, and P. Hommelhoff, Phys. Rev. Appl. **2**, 044015 (2014).
[17]C. C. Chang, H. S. Kuo, I. S. Hwang, and T. T. Tsong, Nanotechnology **20**, 115401 (2009).
[18]B. Cho, T. Ichimura, R. Shimizu, and C. Oshima, PRL **92**, 246103 (2004).
[19]A. Rembold, G. Schütz, W. T. Chang, A. Stefanov, A. Pooch, I. S. Hwang, A. Günther, and A. Stibor, PRA **89**, 033635 (2014).
[20]A. Günther, A. Rembold, G. Schütz, and A. Stibor, PRA **92**, 053607 (2015).
[21]A. Rembold, G. Schütz, R. Röpke, W.-T. Chang, I.-S. Hwang, A. Günther, and A. Stibor, New J. Phys. **19**, 033009 (2017).
[22]O. Jagutzki, V. Mergel, K. Ullmann-Pfleger, L. Spielberger, U. Spillmann, R. Dörner, and H. Schmidt-Böcking, Nucl. Instrum. Methods Phys. Res. A **477**, 244–249 (2002).
[23]W. P. Putnam and M. F. Yanik, PRA **80**, 040902(R) (2009).
[24]P. Kruit, R. G. Hobbs, C.-S. Kim, Y. Yang, V. R. Manfrinato, J. Hammer, S. Thomas, P. Weber, B. Klopfer, C. Kohstall *et al*., Ultramicroscopy **164**, 31 (2016).
[25]J. F. Clauser, Physica B **151**, 262 (1988).
[26]G. Schütz, A. Rembold, A. Pooch, H. Prochel, and A. Stibor, Ultramicroscopy **158**, 65 (2015).
[27]F. Hasselbach and U. Maier, in *Proceedings of the Quantum Coherence and Decoherence - ISQM, Tokyo 98*, edited by Y. A. Ono and K. Fujikawa (Elsevier, Amsterdam, 1999), p. 299.
[28]U. Maier, Ph.D. thesis, University of Tübingen (1997)
[29]W. T. Chang, I. S. Hwang, M. T. Chang, C. Y. Lin, W. H. Hsu, and J. L. Hou, Rev. Sci. Inst. **83**, 083704 (2012).
[30]F. Warken, E. Vetsch, D. Meschede, M. Sokolowski, and A. Rauschenbeutel, Opt. Express **15**, 11952 (2007).
[31]F. Warken, A. Rauschenbeutel, and T. Bartholomäus, Photonics Spectra **42**(3), 73 (2008).
[32]K. S. Yeong and J. T. L. Thong, J. Appl. Phys. **99**, 104903 (2006).
[33]E. Hecht, *Optik*, 6th ed. (Walter De Gruyter Incorporated, Berlin, New York, 2014).
[34]F. Lenz and G. Wohland, Optik **67**, 315 (1984).
[35]E. Krimmel, C. Möllenstedt, and W. Rothemund, Appl. Phys. Lett. **5**, 209 (1964).
[36]W. Brünger, Z. Phys. **250**, 263 (1972).
[37]*CRC Handbook of Metal Etchants*, edited by P. Walker and W. H. Tarn (CRC Press, 1990)
[38]A. Rembold, R. Röpke, G. Schütz, J. Fortágh, A. Stibor, and A. Günther, preprint arXiv:1703.07819 (2017).
[39]R. Saini, Z. Jandric, K. Tsui, T. Udeshi, and D. Tuggle, Microelectron. Eng. **78**, 62 (2005).
[40]N. Maluf and K. Williams, *Introduction to Microelectromechanical Systems Engineering* (Artech House, London, 2004).